学位論文

Development of a High-Angular-Resolution Antenna for Low-Frequency Gravitational-Wave Observation

(低周波重力波観測のための高角度分解能望遠鏡の開発)

平成26年12月博士(理学)申請

東京大学大学院理学系研究科
物理学専攻

正田 亜八香

Contents

Abstract

We have developed a high-angular-resolution gravitational detector for the realization of the low-frequency gravitational wave (GW) astronomy, and searched for GWs from intermediate-mass black hole binaries.

The low-frequency GW is an important targets for the GW astronomy. For example, GWs from black hole binaries and a stochastic GW background are predicted to exist in low frequencies such as $10^{-4} - 1$ Hz. In order to observe the low-frequency GWs, we have proposed a ground-based detector Torsion-Bar Antenna (TOBA). TOBA has two test mass bars which rotate due to the tidal force from GWs. Its main feature is that it has sensitivity around 1 Hz even on the ground because the resonant frequencies in torsional mode is low enough for the bars to behave as free-falling masses. TOBA is expected to detect low-frequency GWs with a relatively low-cost and compact setup compared to the other low-frequency GW detectors such as space-borne detectors. Previously, the first prototype with a single test mass bar had been developed and set the first upper limit on a stochastic GW background at 0.2 Hz.

In this thesis, we developed the Phase-II TOBA for a test of technologies for the sensitivity improvements and for introducing a new observational method. The new observational method we proposed is called a multi-output system. While only the rotation of the test masses in the horizontal plane is monitored in the conventional configuration, we pointed out that the bars rotate also in the vertical plane. Consequently, the three independent signals are derived from a single detector by monitoring the vertical rotation and the horizontal rotation at the same time. This method improves the event rate of the detection, and the angular resolution of the GW sources. We successfully derived the three signals at the same time using Phase-II TOBA, and established the multi-output observation system.

Other than the multi-output system, we introduced the vibration isolation systems in order to reduce the seismic noise. One is passive vibration isolation with the suspension system for the noise reduction at higher frequencies, and the other is active vibration isolation using the six-legged table for the noise reduction at lower frequencies. As a result, the sensitivity in the horizontal rotation is improved at 1 - 10 Hz due to the vibration isolation.

Using the Phase-II TOBA, we performed an observational run for continuous 24 hours and searched for mergers of intermediate-mass black hole (IMBH) binaries with the mass of $200 M_\odot$ as a demonstration. This is the first search for the IMBH

binaries heavier than $100M_\odot$. As a result, no GW signals are detected and we have set an observational upper limit that there is no IMBH binaries within 1.2×10^{-4} pc of the Earth.

Though the sensitivity of the Phase-II TOBA is not enough for the GW detection, our technologies developed in this thesis are validated for the establishment of the low-frequency GW astronomy.

Glossary

Acronym	**Definition**
ADC	Analog to Digital Converter
AVIT	Active Vibration Isolation Table
BBN	Big Bang Nucleosynthesis
CBC	Compact Binary Coalescence
CMB	Cosmic Microwave Background
DAC	Digital to Analog Converter
DECIGO	DECi-hertz Interferometer Gravitational wave Observatory
FAR	False Alarm Rate
FDR	False Dismissal Rate
GW	Gravitational Wave
IMBH	Intermediate-Mass Black Hole
LIGO	Laser Interferometer Gravitational wave Observatory
LISA	Laser Interferometer Space Antenna
LS	Laser Sensor
OLTF	Open Loop Transfer Function
PS	Photo Sensor
RMS	Root Mean Square
SGWB	Stochastic Gravitational Wave Background
SMBH	Super Massive Black Hole
TOBA	TOrsion-Bar Antenna
TTgauge	Transverse-Traceless gauge
UGF	Unity Gain Frequency

Chapter 1

Introduction

Since Galileo Galilei had pointed a telescope at moon in 1609, we have observed the Universe using the electro-magnetic waves. Various laws of nature are revealed by the observation of the Universe. However, some phenomena cannot be observed with electro-magnetic waves, e.g., information inside the astronomical object, the characteristics of black holes, the Universe before the transparent to radiation, and so on. One of the possible method to observe such phenomena is the gravitational waves (GWs).

GWs are distortion of the space and time propagating with the speed of light. They are predicted by Albert Einstein in 1916 as the consequence of the general theory of relativity. They are considered to be emitted from astronomical objects with heavy mass moving at accelerated speed, such as neutron star binaries, black hole binaries, supernovae, and so on. The presence of GWs is proven from the decreasing orbital period of the pulsar. Hulse and Taylor had measured the orbital period of PSR B1913+16 for about 30 years to verify that the kinetic energy loss in the binary system matches the energy loss due to gravitational radiation [35, 51]. They won the Nobel prize in 1993 because of this observation. However, the distortion due to GWs are too small to be detected directly.

Nowadays – about 100 years later from the Einstein's first prediction, the GWs are about to be detected. The GW detectors have been widely studied since Weber claimed that GWs are detected with a pair of resonant bar detectors in 1970 [57]. Though the direct detection of GWs have not been verified by the further experiments, the GW detectors drastically improve their sensitivity due to keen study by many researchers all over the world. The current main stream of the GW detectors is ground-based interferometric GW detectors with the arm length of 3 - 4 km. In US, Large Interferometer Gravitational wave Observatory (LIGO) [53] is now under upgrading. Also in Europe, the large-scaled interferometer Virgo [10] is under upgrading. In addition, the cryogenic interferometer KAGRA is now under construction in Kamioka, Japan [49]. These detectors will have sensitivity high enough to have the expected event rate of $\sim 10/\text{yr}$ for the mergers of neutron star binaries.

The observation frequency band of the ground-based interferometers are around 100 Hz. Therefore the their main observational targets are the neutron star binary coalescence and supernovae. Observation of the neutron star binaries will reveal the state equation of the neutron stars, the mechanism of the gamma-ray burst, and so on. GWs from the supernovae are expected to contain information about their core which would help to unravel the mechanism of the explosion. While the large scientific impacts are expected from the observational results of the ground-based interferometers, it is necessary to observe GWs in various frequencies in order to evolve astronomy using GWs. For example, mergers of black holes are expected to be observed in low frequencies, such as mHz to 1 Hz. The space-borne interferometers, such as Laser Interferometer Space Antenna (LISA) [55] and DECI-herz Gravitational Observatory (DECIGO) [39], are planned to be launched for low-frequency GW observation.

However, since the space GW antennas are large project such that three space crafts construct large interferometers in space. They require many advanced technologies, but also they have difficulties in repairing, upgrading and so on. In order to get rid of these problems, Torsion-bar Antenna (TOBA) had been proposed [12]. The TOBA is a GW detector composed of two bar-shaped test masses which rotate differentially due to the tidal force from GWs. The main feature of TOBA is that it is sensitive to GWs at lower frequencies such as around 1 Hz even on the ground. Low resonant frequencies of the torsional mode realize the free-falling test masses around 1 Hz, i.e, the sensitive test masses to GWs. One of our observational targets is GW from a merger of the intermediate-mass black hole (IMBH) binary. IMBH is recently found in globular clusters and considered to be a seed of super-massive black holes (SMBHs). Observation of the IMBH coalescence is important for the theory of the SMBH evolution, and the galaxy evolution. Another target is a stochastic GW background. While the observation of a stochastic GW background with the cosmic micro-wave background (CMB) is discussed, it is also important to observe the background in various frequencies. The frequency dependence of the energy of the background has the information of the history of the Universe, such as the re-heating temperature.

For the low-frequency GW detection, the first prototype of the TOBA had been developed previously [38]. It has a single test mass bar suspended by the pinning effect of a superconductor. They performed the principle test and the first observation [38, 48]. In this thesis, we have developed the upgraded TOBA, which is called ‘Phase-II TOBA’ here. It is a new detector for the development of vibration isolation technologies, and for the principle test of the multi-output system. Here, we developed the passive and active vibration isolation system for the TOBA and successfully reduced the seismic noise. Also, we established the multi-output system, which derives three independent signals from a single detector. The multi-output system improves the event rate and the angular resolution of the detector. Also, we performed the observation for continuous 24 hours. Using these data, $200M_\odot$ IMBH binaries are searched for for the first time. Consequently, the GW signals are not detected and the have set an upper limit on the event rate of IMBH mergers.

In our thesis, the characteristics of GWs and the principle of the TOBA are explained at first (Chapter 2, and 3). Subsequently, the concept of the Phase-II TOBA, including the principle of the muti-output system and the detector design, is discussed in Chapter 4. The measured characteristics of the constructed detectors are shown in Chapter 5. In Chapter 6, we performed the observational run and searched for IMBH binaries as a part of an end-to-end test.

Chapter 2

Gravitational Waves

In this section, we briefly review the theory of GWs. We derive the GWs from by linearizing the Einstein equation. Subsequently, we explain how GWs are emitted from the astronomical sources, their characteristics, and how they affect on free masses.

2.1 Theory of the Gravitational Waves

2.1.1 Geodesic Equation and Metric Tensor

According to the General Theory of Relativity, the infinitesimal distance between two points in the space time x^μ and $x^\mu + dx^\mu$ is

$$ds^2 = g_{\mu\nu} dx^\mu dx^\nu, \tag{2.1}$$

where $g_{\mu\nu}$ is the metric tensor which represents the structure of the space time. The motion of the free masses which do not receive the external forces except gravity can be derived by the Geodesic Equation:

$$\frac{d^2 x^\lambda}{d\tau^2} = \Gamma^\lambda_{\mu\nu} \frac{dx^\mu}{d\tau} \frac{dx\nu}{d\tau}. \tag{2.2}$$

Here, τ is the proper time and $\Gamma^\lambda_{\mu\nu}$ is the Christoffel symbol:

$$\Gamma^\lambda_{\mu\nu} = \frac{1}{2} g^{\gamma\alpha} \left(\frac{\partial g_{\alpha\mu}}{\partial x^{nu}} + \frac{\partial g_{\alpha\nu}}{\partial x^\mu} - \frac{\partial g_{\mu\nu}}{\partial x^\alpha} \right). \tag{2.3}$$

Therefore, the motion of the free mass depends on $g_{\mu\nu}$.

2.1.2 Linearization of the Einstein Equation

$g_{\mu\nu}$ obeys the Einstein equation:

$$R_{\mu\nu} - \frac{1}{2} g_{\mu\nu} R = \frac{8\pi G}{c^4} T_{\mu\nu}, \tag{2.4}$$

where $R_{\mu\nu}, R$, and $T_{\mu\nu}$ are the Ricci tensor, the Ricci scalar, and the Energy momentum tensor tensor, respectively. c is the speed of the light and G is the gravity constant. $R_{\mu\nu}$ and R are derived from

$$\begin{aligned} R_{\mu\nu} &= R^{\alpha}_{\mu\alpha\nu} &(2.5)\\ R &= g^{\mu\nu}R_{\mu\nu}, &(2.6)\end{aligned}$$

where $R^{\gamma}_{\mu\rho\nu}$ is the Riemann curvature tensor

$$R^{\gamma}_{\mu\rho\nu} = \frac{\partial\Gamma^{\gamma}_{\mu\nu}}{\partial x^{\rho}} - \frac{\partial\Gamma^{\gamma}_{\mu\rho}}{\partial x^{\nu}} + \Gamma^{\gamma}_{\alpha\rho}\Gamma^{\alpha}_{\mu\nu} - \Gamma^{\gamma}_{\beta\nu}\Gamma^{\beta}_{\mu\rho}. \tag{2.7}$$

When the perturbation $h_{\mu\nu}$ is added to the flat space, i.e. the metric tensor is written by $g_{\mu\nu} = \eta_{\mu\nu} + h_{\mu\nu}$, where $\eta_{\mu\nu}$ is the metric tensor of the Minkowski space, Christoffel symbol, Riemann curvature tensor, Ricci curvature tensor, and Ricci scalar are

$$\begin{aligned}
\Gamma^{\lambda}_{\mu\nu} &\sim \frac{1}{2}\eta^{\gamma\alpha}\left(\frac{\partial h_{\alpha\mu}}{\partial x^{\nu}} + \frac{\partial h_{\alpha\nu}}{\partial x^{\mu}} - \frac{\partial h_{\mu\nu}}{\partial x^{\alpha}}\right) &(2.8)\\
R^{\gamma}_{\mu\rho\nu} &\sim \frac{1}{2}\eta^{\gamma\alpha}\left(\frac{\partial^2 h_{\alpha\nu}}{\partial x^{\rho}\partial x^{\mu}} - \frac{\partial^2 h_{\mu\nu}}{\partial x^{\alpha}\partial x^{\rho}} + \frac{\partial^2 h_{\mu\rho}}{\partial x^{\alpha}\partial x^{\nu}} - \frac{\partial^2 h_{\alpha\beta}}{\partial x^{\mu}\partial x^{\nu}}\right) &(2.9)\\
R_{\mu\nu} &\sim \frac{1}{2}\left(\frac{\partial^2 h^{\lambda}_{\nu}}{\partial x^{\lambda}\partial x^{\mu}} - \frac{\partial^2 h_{\mu\nu}}{\partial x_{\lambda}\partial x^{\lambda}} + \frac{\partial^2 h^{\lambda}_{\mu}}{\partial x^{\lambda}\partial x^{\nu}} - \frac{\partial^2 h}{\partial x^{\mu}\partial x^{\nu}}\right) &(2.10)\\
R &\sim \frac{\partial^2 h^{\mu\nu}}{\partial x^{\mu}\partial x^{\nu}} - \frac{\partial^2 h}{\partial x_{\alpha}\partial x^{\alpha}}. &(2.11)
\end{aligned}$$

Here, $h \equiv h^{\lambda}_{\lambda}$.

Taking Lorentz Gauge

$$\frac{\partial \overline{h}^{\mu}_{\nu}}{\partial x^{\mu}} = 0, \tag{2.12}$$

where the trace reverse tensor $\overline{h}_{\mu\nu}$ is defined as

$$\overline{h}_{\mu\nu} \equiv h_{\mu\nu} - \frac{1}{2}\eta_{\mu\nu}h, \tag{2.13}$$

we obtain the linearized Einstein equation

$$\frac{\partial^2 \overline{h}_{\mu\nu}}{\partial x^{\alpha}\partial x_{\alpha}} = \Box\overline{h}_{\mu\nu} = -\frac{16\pi G}{c^4}T_{\mu\nu}. \tag{2.14}$$

In the vacuum, i.e. $T_{\mu\nu} = 0$,

$$\Box\overline{h}_{\mu\nu} = 0, \tag{2.15}$$

, i.e., the wave equation is derived. $\overline{h}_{\mu\nu}$ propagating in the space time is the GWs.

2.1.3 Monochromatic Plain-Wave Solution

The monochromatic plain-wave solution of 2.15 is given as

$$\overline{h}_{\mu\nu} = A_{\mu\nu} e^{ik_\alpha x^\alpha}. \tag{2.16}$$

Substituting 2.16 to 2.12 and 2.15,

$$\begin{aligned} A_{\mu\nu} k^\mu &= 0 \qquad (2.17) \\ k_\mu k^\mu &= 0 \qquad (2.18) \end{aligned}$$

are derived.

Here, we take the transverse-traceless gauge (TT gauge),

$$\begin{aligned} A^\alpha_\alpha &= 0, \qquad (2.19) \\ A_{\mu\nu} U^\nu &= 0, \qquad (2.20) \end{aligned}$$

where U^ν is an arbitrary time vector.

Setting $U^\nu = \delta^\nu_0$, which is a unit vector of time in the Minkowski space,

$$A_{\mu\nu} \delta^\nu_0 = A_{\mu 0} = 0. \tag{2.21}$$

Also, Considering the GWs with the angular vibration ω propagating along the z-axis,

$$A_{\mu 3} = 0. \tag{2.22}$$

Then, $A_{\mu\nu}$ is derived as

$$A_{\mu\nu} = \begin{pmatrix} 0 & 0 & 0 & 0 \\ 0 & h_+ & h_\times & 0 \\ 0 & h_\times & -h_+ & 0 \\ 0 & 0 & 0 & 0 \end{pmatrix}. \tag{2.23}$$

Here, h_+ and $h_\times$ represent two polarizations of the GWs.

Consequently, we derive the generalized solution of GWs. Defining polarization tensors

$$\begin{aligned} e^+_{\mu\nu}(\hat{\boldsymbol{n}}) &\equiv \hat{\boldsymbol{u}}_\mu \hat{\boldsymbol{u}}_\nu - \hat{\boldsymbol{v}}_\mu \hat{\boldsymbol{v}}_\mu \qquad (2.24) \\ e^\times_{\mu\nu}(\hat{\boldsymbol{n}}) &\equiv \hat{\boldsymbol{u}}_\mu \hat{\boldsymbol{v}}_\nu + \hat{\boldsymbol{v}}_\mu \hat{\boldsymbol{u}}_\nu, \qquad (2.25) \end{aligned}$$

where $\hat{\boldsymbol{n}}$ is a unit vector parallel to the direction in which GWs propagate, and $\hat{\boldsymbol{u}}$ and $\hat{\boldsymbol{v}}$ are unit vectors orthogonal to $\hat{n}$ and each other, general solution of GWs is derived as

$$\overline{h}_{\mu\nu} = \sum_{A=+,\times} h_A(\hat{\boldsymbol{n}}) e^A_{\mu\nu}(\hat{\boldsymbol{n}}) e^{-i\omega(t-\hat{\boldsymbol{n}}\dot{\boldsymbol{x}}/c)}. \tag{2.26}$$

Here $\boldsymbol{x}$ is a position vector of an observation point. The GWs observed at $\boldsymbol{x}$ in t is the superposition of GWs coming from all directions with all frequencies:

$$\overline{h}_{ij}(t, \boldsymbol{x}) = \sum_{A=+,\times} \int_{-\infty}^{+\infty} d\omega \int d^2\hat{\boldsymbol{n}} h_A(f, \hat{\boldsymbol{n}}) e^A_{ij}(\boldsymbol{n}) e^{-i\omega(t-\hat{\boldsymbol{n}}\dot{\boldsymbol{x}}/c)}. \tag{2.27}$$

2.1.4 Effect on Free Masses

Here, we consider about the effect of the GWs on the free-falling masses in the small region around the coordinate x, which is the laboratory system called the proper detector frame.

The Geodetic Equation at $x+\xi$, a point apart from x by inifinitestimal distance ξ is

$$\frac{d^2(x^\mu + \xi^\mu)}{d\tau^2} = -\Gamma^\mu_{\nu\rho}(x+\xi) \frac{d(x^\nu + \xi^\nu)}{d\tau} \frac{d(x^\rho + \xi^\rho)}{d\tau}. \tag{2.28}$$

Taking only the first order of ξ,

$$\frac{d^2\xi^\mu}{d\tau^2} = -2\Gamma^\mu_{\nu\rho}(x) \frac{dx^\mu}{d\tau} \frac{d\xi^\rho}{d\tau} - \xi^\sigma \frac{\partial \Gamma^\mu_{\nu\rho}}{dx^\sigma}(x) \frac{dx^\mu}{d\tau} \frac{dx^\rho}{d\tau}. \tag{2.29}$$

Since the metric tensor can be approximated as $g_{\mu\nu} \sim \eta_{\mu\nu}$, and the velocity of the observer is $\frac{dx^i}{d\tau} \ll \frac{dx^0}{d\tau} = c$, the geodetic equation in the proper detector frame is derived from 2.7, 2.9, and 2.29 as follows:

$$\begin{aligned} \frac{d^2\xi^\mu}{d\tau^2} &= -c^2 \frac{\partial \Gamma^\mu_{00}}{\partial x^\sigma} \xi^\sigma \\ &= -c^2 R^\mu_{0\sigma 0} \xi^\sigma \\ &= \frac{1}{2} \frac{\partial^2 h^\mu_\sigma}{\partial t^2} \xi^\sigma. \end{aligned} \tag{2.30}$$

It means that the tidal force from GWs

$$F^\mu = \frac{m}{2} \ddot{h}^i_j \xi^j \tag{2.31}$$

is applied to the free mass with the mass of m.

Solving 2.30 with the condition that the answer does not get infinity at $t \to \infty$, we get

$$\delta\xi^i = \frac{1}{2} h^i_j \xi^j. \tag{2.32}$$

When GW with angular frequency of ω is incoming from x axis,

$$\begin{pmatrix} \delta\xi^x \\ \delta\xi^y \end{pmatrix} = \frac{1}{2}\begin{pmatrix} h_+ & h_\times \\ h_\times & -h_+ \end{pmatrix}\begin{pmatrix} \xi^x \\ \xi^y \end{pmatrix} e^{i\omega(t-z/c)} \tag{2.33}$$

$$= \frac{1}{2} h_+ \begin{pmatrix} \xi^x \\ -\xi^y \end{pmatrix} e^{i\omega(t-z/c)} + \frac{1}{2} h_\times \begin{pmatrix} \xi^y \\ \xi^x \end{pmatrix} e^{i\omega(t-z/c)} \tag{2.34}$$

is obtained. The first term and the second term represents the two polarization of GWs, + mode and × mode. The motion of the free masses caused by GWs with each polarization is pictured in Fig.2.1.

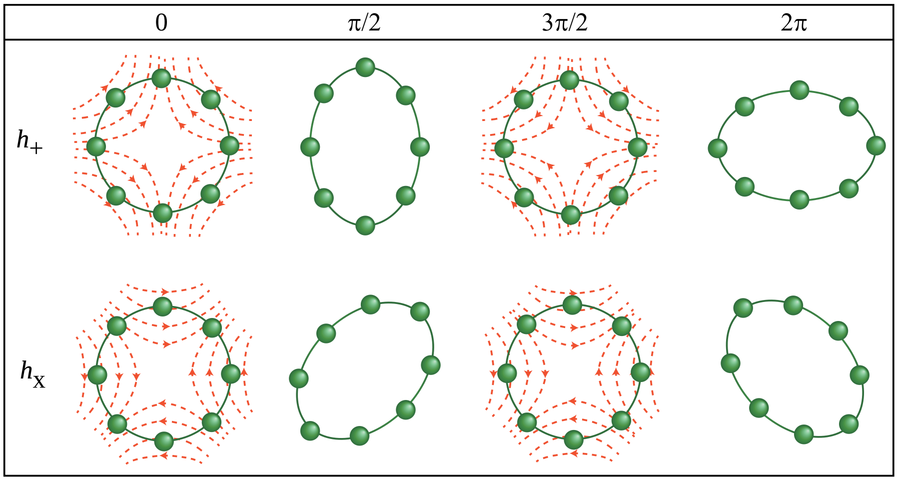

Figure 2.1: A picture of the two modes of GWs.

2.1.5 Generation of Gravitational Waves

Considering about the GWs coming from a small source at a distant place, the amplitude of GWs is derived as below:

$$\overline{h}_{ij}(t,x) = \frac{4G}{c^4}\int \frac{T_{ij}\left(t - \frac{|\overrightarrow{x}-\overrightarrow{x'}|}{c}, \overrightarrow{x'}\right)}{|\overrightarrow{x}-\overrightarrow{x'}|} d^3x'. \tag{2.35}$$

In case of the GW source (the region where $T_{ij} \neq 0$) is small enough compared with the wavelength of GWs, and the observer is far enough from the GW source, the equation above is approximated by

$$\overline{h}_{ij}(x) = \frac{2G}{c^4 r}\ddot{Q}_{ij}(t'), \tag{2.36}$$

where $r \equiv |\overrightarrow{x} - \overrightarrow{x'}|$, $t' \equiv t - r/c$, and Q_{ij} is a quadrupole moment defined by

$$Q_{ij}(t) = \int \rho(\overrightarrow{x'}, t') \left(x'_y x'_j - \frac{1}{3}\delta_{ij} x'^i x'^j \right) d^3x'. \tag{2.37}$$

Here, ρ is the density of the GW source.

2.2 Gravitational Wave Sources

GWs are considered to be emitted from various phenomena, e.g., binary coalescence, rotation of asymmetric stars, supernovae, and cosmic strings. In this section, we will briefly review the astronomical and cosmological sources of GWs and the recent observational results.

2.2.1 Compact Binary Coalescence

The binary systems made of compact stars, such as black holes and neutron stars, are promising sources of gravitational waves. PSR B1913+16, called Hulse-Taylor binary pulsar, is the neutron star binary system is the one of the strong evidence of the existence of GWs. Hulse and Taylor measured its parameters with high precision, such as the reduction of its orbital period, to prove their motion obeys the General Theory of Relativity very well [35, 51].

Define the mass of the binary stars as m_1 and m_2, the orbital radius as R, the amplitude of GW is derived as follows:

$$\begin{aligned} h_+(t) = \frac{4}{r}\left(\frac{GM_c}{c^2}\right)^{5/3}\left(\frac{\pi f_{\mathrm{gw}}(t)}{c}\right)^{2/3}\frac{1+\cos^2\theta}{2} \\ \cos(\int 2\pi f_{\mathrm{gw}}(t)dt \cdot t_{\mathrm{ret}} + \phi), \end{aligned} \tag{2.38}$$

$$h_\times(t) = \frac{4}{r}\left(\frac{GM_c}{c^2}\right)^{5/3}\left(\frac{\pi f_{\mathrm{gw}}(t)}{c}\right)^{2/3}\cos\theta\sin(\int 2\pi f_{\mathrm{gw}}(t)dt \cdot t_{\mathrm{ret}} + \phi), \tag{2.39}$$

where θ is the angle between the normal to the orbit and the line-of sight, and

$$M_c = \frac{(m_1 m_2)^{3/5}}{(m_1 + m_2)^{1/5}}, \tag{2.40}$$

$$f_{\rm gw}(t) = \frac{G(m_1 + m_2)}{\pi R(t)^3}. \tag{2.41}$$

Here, M_c is called the chirp mass.

Since the radiated energy due to GWs is the sum of the kinetic energy of the potential energy, $f_{\rm gw}(t)$ is derived as

$$f_{\rm gw}(t) = \frac{1}{\pi}\left(\frac{5}{256}\frac{1}{t_{\rm coal} - t}\right)^{3/8}\left(\frac{GM_c}{c^3}\right), \tag{2.42}$$

where $t_{\rm coal}$ is the time to coalesce. This waveform is called chirp, as shown in Fig.2.2.

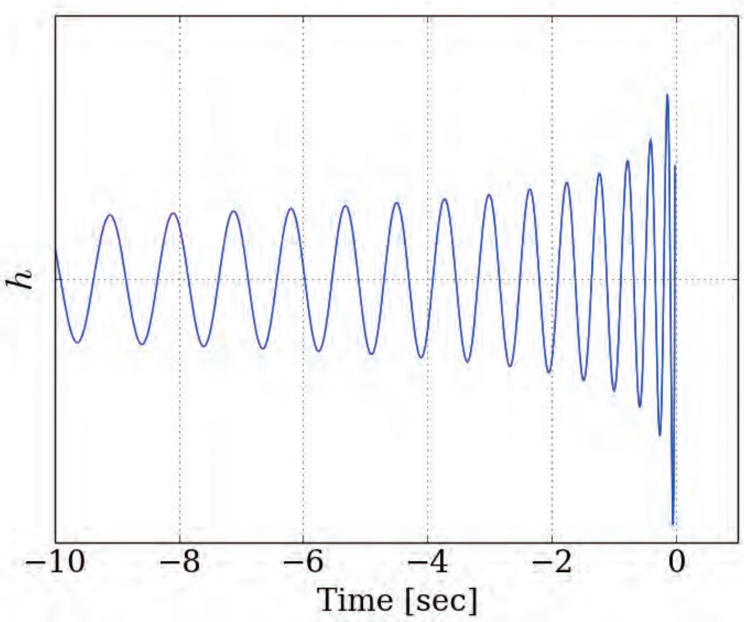

Figure 2.2: The chirp signal of GWs from 1000 - 1000 $M_\odot$ binary system. $t = 0$ is the time to coalesce.

However, the equations above are valid only when the background space-tune can be assumed to be flat. When the rotating stars are close and held together by gravitational force, i.e., the two stars are near to merge, the assumption that the velocity of stars and the space-time curvature are independent is not valid. In order to deal with such relativistic systems, a post-Newtonian (PN) formalism is introduced. Please refer [41] for the details of the formalism of PN waveforms.

GWs from binary systems, especially double neutron stars or neutron-star-black-hole binaries are searched by various GW detectors. For example, LIGO and Virgo have recently searched GWs associated with γ-ray bursts, which is believed to be emitted from mergers of compact astronomical objects, and have set a lower bounds on the distance for various GW emission models [5]. As a future perspectives, advanced LIGO and Virgo are predicted to detect GWs from such compact binary coalescences (CBCs) about 40 times per year [8]. Other than neutron star binaries, more massive objects, i.e., black hole binaries are searched by ground-based detectors, doppler tracking, and pulsar timing.

2.2.2 Rotating Stars

Single rotating compact stars such as neutron stars also emit GWs when the shape of the star is asymmetric. Considering a star rotating with the angular velocity $\omega_{\rm rot}$, a emitted GW is a monochromatic signal written as

$$\begin{aligned} h_+ &= \frac{4\pi^2 G}{c^4}\frac{I f_{\rm gw}^2 t}{r}\epsilon\frac{1+\cos^2\theta}{2}\cos(2\pi f_{\rm gw}t), && (2.43)\\ h_\times &= \frac{4\pi^2 G}{c^4}\frac{I f_{\rm gw}^2 t}{r}\epsilon\cos\theta\sin(2\pi f_{\rm gw}t), && (2.44)\\ & && (2.45)\end{aligned}$$

where r, I, and ϵ are the distance to the neutron star, moment of inertia around rotating axis, and ellipticity of the star respectively. Inserting numerical reference values, the equation gives [41]

$$h \sim 3.6\times 10^{-27}\left(\frac{\epsilon}{10^{-5}}\right)\left(\frac{I}{10^{38}\mathrm{kg\ m}^2}\right)\left(\frac{10\mathrm{kpc}}{r}\right)\left(\frac{f_{\rm gw}}{60\mathrm{Hz}}\right)^2. \tag{2.46}$$

The Crab pulsar is one of the promising objects which rotate with the frequency of 60.2 Hz. Such monochromatic GW signals have been searched for using the resonant GW detectors [66]. Later, the interferometric detectors searched for continuous GW signals from the Crab pulsar and set an upper limit about a factor of two below the spin-down limit, which is the amplitude of GWs calculated with the assumption that all the rotational kinetic energy loss by spin-down is converted to GWs [54].

2.2.3 Burst-like GWs

Here, we briefly introduce GW sources which emit burst-like GWs. One of the representative burst-like GW sources is supernova. Supernovae emit GWs when their core collapse. Though their waveforms are unknown yet, they are numerically simulated based on several models of explosion [43]. Other than supernovae, pulsar glitches[1], gamma-ray bursts, and soft gamma repeaters[2] are candidates of GW sources.

LIGO and Virgo have searched for burst-like signals without any assumptions on waveform and set an upper limit on the event rate as 1.3 event per year [6]. In the future, advanced LIGO is expected to be able to detect the GWs from supernovae occurred anywhere in our galaxy [59].

2.2.4 Stochastic Gravitational Wave Background

A stochastic GW background (SGWB) is a cosmologically interesting target which has the information about the history of the Universe. It is a superposition of the GWs originated in the cosmological phenomena such as the fluctuations of the space-time in the early Universe and the cosmic string, and the GWs from unresolved astronomical objects. The amplitude of a SGWB of a cosmological origin is larger at lower frequency when $\Omega_{\rm gw}(f)$, which is the energy per unit logarithmic interval of frequency, does not have frequency dependency, while the waveform of a SGWB is considered to be Gaussian, and unpredictable.

A SGWB has been searched using various detectors in various frequencies. Various telescopes, e.g., Planck, WMAP, and BICEP, are eagerly searching for a SGWB using the B-mode polarization of CMB. These telescopes can observe a SGWB at extremely low frequencies such as $10^{-18} - 10^{-16}$ Hz, whose wavelength is order of the size of the Universe. At very low frequencies, such as $10^{-10} - 10^{-8}$ Hz, Pulsar Timing Array have set upper limits on a SGWB [42]. Above those frequencies, an upper limit has been set using the Doppler Tracking measurement [14]. At higher frequencies, the interferometers, LIGO and Virgo, have set an upper limit around 100 Hz by the simultaneous observation [9]. Other than the large-scaled interferometers, 75-cm baseline synchronous recycling interferometers have set an upper limit at high frequency of 100 MHz [11]. Also the cryogenic resonant bar detectors, EXPLORE and NAUTILUS set upper limits by simultaneous observation [15]. Around 1 Hz, a single, and a pair of TOBA had set the upper limit around 0.2 Hz

---

[1] Pulsar glitch is a sudden increase in the rotational frequency of a pulsar.

[2] Soft gamma repeaters are astronomical objects which emit gamma-rays and X-rays irregularly. They are inferred to be magnetars or neutron stars

[38, 48]. Though other ground-based detectors do not have sensitivity around these frequencies, several upper limits have been placed recently, using Global Positioning System (GPS) [13], the seismic waves of the moon [24], that of the Earth [25], and the Earth as the resonant detector [26]. Note that the search methods using seismic sensors [24, 25, 26] are difficult to improve the sensitivity since the motion of their test masses, which are the Earth and moon, cannot be suppressed.

Chapter 3
TOBA

In this chapter, we will explain the merit and demerit of TOBA and its principle. Also, we will refer to the example configuration of the large-scaled TOBA and a road map to the ultimate detector.

3.1 Concept

The conventional GW detectors are sensitive to GWs only above about 10 Hz because of the seismic noise. In order to observe low-frequency GWs, space-borne GW detectors such as LISA and DECIGO are planned to be launched. However, the space detectors have difficulties in their cost, repair, and upgrade while they have potential for highly sensitive GW detectors because of its long baseline, escape from the seismic noise and the effect of the gravity, and so on.

The TOBA is now under development as a novel low-frequency GW detector. Its main feature is to have sensitivity to GWs at low frequencies such as 1 Hz even on the ground. The rotational motion of the test mass is monitored in the TOBA while the pendulum motion is observed in the interferometers. The test masses behave as free masses even at low frequencies, i.e., it is sensitive to GWs, since the resonant frequency of the rotational mode is as low as a few mHz. Also, the configuration of TOBA is relatively simple, compact and low-cost, while it is difficult to achieve as good sensitivity as interferometers since the length of the baseline is limited. Therefore, TOBA is expected to observe low-frequency GWs before space-borne GW detectors are launched and to accelerate the evolution of the GW astronomy by feeding back its scientific results to the design of space GW detectors.

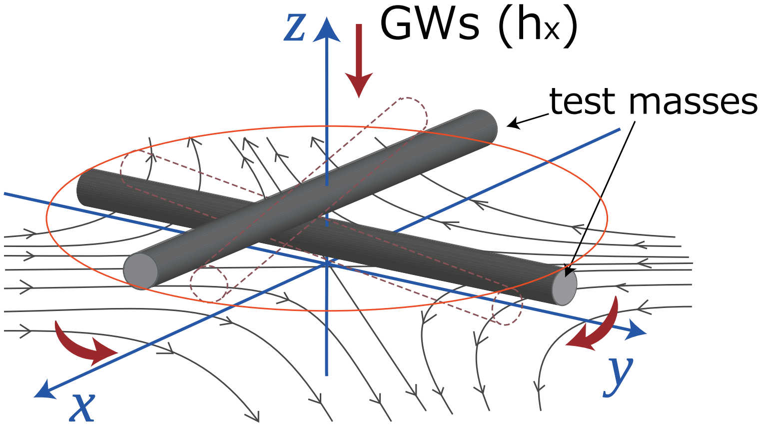

Figure 3.1: The conceptual picture of the TOBA.

3.2 Response to the Gravitational Waves

3.2.1 Equation of Motion

The Fig.3.1 is the schematic view of the TOBA. In this section, we will explain how the test masses of the TOBA react according to the GWs. We assume that the two bars are set along x axis and y axis respectively, and suspended at their center so that they rotate in $x-y$ plane.

The equation of the motion in the rotational mode is

$$I\ddot{\theta}(t)+\gamma\dot{\theta}(t)+\kappa\theta(t)=F_{\rm gw}, \tag{3.1}$$

where θ, I, γ, and κ are angular fluctuation around z axis, the moment of inertia around z axis, the damping constant and the spring constant respectively.

$F_{\rm gw}$ is derived by calculating the differential of energy stored in the test mass. The tidal force from GWs on the infinitesimal volume dV of the bar is

$$F^i dV=\frac{\rho}{2}\ddot{h}^i_j\xi^j dV \tag{3.2}$$

from 2.31, where ρ and ξ are the density of the test mass and the position of the infinitesimal volume dV. Since the test mass stores the energy

$$\begin{aligned} U &= -\int\int F^2 dV d\xi_i && (3.3)\\ &= \frac{\ddot{h}_{ij}}{4}\int \rho\xi^i\xi^j dV, && (3.4) \end{aligned}$$

the tidal force $F_{\rm gw}$ is derived as

$$F_{\rm gw} = -\frac{\partial U}{\partial \theta} = \frac{1}{4}\ddot{h}_{ij}q^{ij}. \tag{3.5}$$

Here, θ is the angular fluctuation around z axis and q^{ij} is the quadrupole moment of the test mass defined as

$$q^{ij} = \int \rho \left(\xi^i w^j + \xi^j w^i - \frac{2}{3}\delta^{ij}\xi^k w_k \right) dV. \tag{3.6}$$

w^i is the mode function, which in case of the rotation mode is written as

$$w^i = \begin{pmatrix} -y \\ x \\ 0 \end{pmatrix}. \tag{3.7}$$

Substituting 3.7 into 3.6, the quadrupole moments are derived as follows:

$$q_+ = q_{11} = -q_{12} = \int \rho 2xy dV, \tag{3.8}$$

$$q_\times = q_{12} = q_{21} = -\int \rho \left(x^2 - y^2\right) dV. \tag{3.9}$$

Assuming that a GW with the amplitude of

$$h(t) = \begin{pmatrix} h_+ & h_\times & 0 \\ h_\times & -h_+ & 0 \\ 0 & 0 & 0 \end{pmatrix} \tag{3.10}$$

is incoming into the torsion pendulum, the equation of motion in frequency domain is written as

$$-\omega^2 I\tilde{\theta}(\omega) + i\omega\gamma\tilde{\theta}(\omega) + \kappa(1+i\phi)\tilde{\theta}(\omega) = -\frac{1}{2}\omega^2(h_+q_+ + h_\times q_\times). \tag{3.11}$$

Therefore, the frequency response of the angular fluctuation to the GW is

$$\tilde{\theta}(\omega) = \sum_{A=+,\times} H_A(\omega)\tilde{h}_A, \tag{3.12}$$

$$H_A(\omega) = \frac{q_A}{2I}\frac{\omega^2}{\omega^2 - \omega_0^2(1+i\phi) + i\omega/I}, \tag{3.13}$$

where $\omega_0 = 2\pi f_0 = \sqrt{|\kappa|/I}$ is the resonant frequency of the torsional mode.

Considering uniform rectangular test mass,

$$
\begin{aligned}
q_+ &= 0 && (3.14)\\
q_\times &= \frac{1}{12}M(l^2 - r^2) \sim \frac{1}{6}Ml^2, && (3.15)\\
I &= \frac{1}{12}M(r^2 + l^2) \sim \frac{1}{12}Ml^2, && (3.16)
\end{aligned}
$$

where M, l, and r are the mass, the length of the longer side and the shorter side of the test mass, respectively. Substituting the equations above into 3.13, the transfer functions from GWs to the angular fluctuations are

$$
\begin{aligned}
H_+(\omega) &= 0 && (3.17)\\
H_\times(\omega) &= \frac{1}{2}\frac{\omega^2}{\omega^2 - \omega_0^2(1 + i\phi) + i\omega/I}, && (3.18)
\end{aligned}
$$

which indicates that the TOBA is sensitive only to the GWs with ×-mode.

The other orthogonal test mass also rotates similarly, but in the opposite direction. Therefore, the common mode noise between the two test masses can be rejected by taking the differential $\theta_1 - \theta_2$.

Also, the absolute value of $H_\times$ vs the frequency is plotted in Fig.3.2. It shows that $H_\times \sim 1/2$ is larger at higher frequencies than the resonant frequency while it gets small below the resonant frequency. Around the resonant frequencies, the sensitivity is better when the Q-value is better. The conventional resonance detectors searches GWs around their resonant frequencies while their resonant frequencies are as high as 300 Hz. In case of TOBA, the observation is performed at higher frequencies than f_0 as interferometric GW detectors so that broadband observation is enabled. The main feature of TOBA is that f_0 is lower than that of interferometers. Since the interferometers detect GWs using the pendulum motion of the test masses, whose resonant frequency is about 1 Hz, the observation band of interferometers is around 100 Hz. On the other hand, the observation band of the TOBA is around 1 Hz even on the ground since the resonant frequencies of torsional mode are as low as a few MHz.

3.2.2 Pattern function

The pattern function is the detector response function of the incident angle of GWs to the detector. Considering a GW $h_{ij}(t)$ propagating along $\boldsymbol{n} = (1, \Theta, \Phi)$ in the

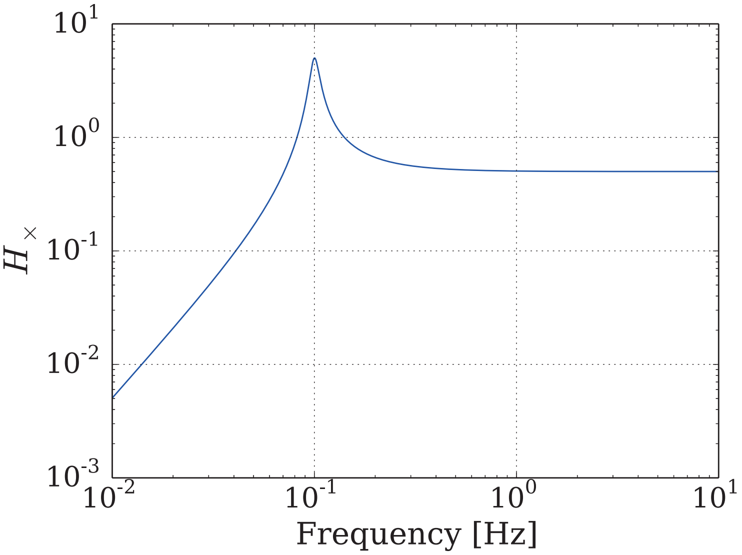

Figure 3.2: The transfer function from GWs to the angular fluctuation of the test mass. The resonant frequency f_0 and Q-value, which is defined by $Q = \omega_0 I/\gamma$, are set to be 0.1 Hz and 10, respectively. While the TOBA do not respond to GWs at lower frequencies than the resonant frequency, it has a flat response at higher frequencies than the resonant frequency.

polar coordinate, the amplitude of the GW $h(t)$ is

$$h(t) = \sum_{A=+,\times} F^A(\boldsymbol{n}) h_A(t), \tag{3.19}$$

with $F^A(\boldsymbol{n})$ is the pattern function defined as

$$F^A(\boldsymbol{n}) \equiv D^{ij} e^A_{ij}(\boldsymbol{n}). \tag{3.20}$$

Here, $e^A_{ij}(\boldsymbol{n})$ is the polarization tensors defined as shown in 2.24 D^{ij} is called the detector tensor which depends on the detector geometry. In case of the TOBA set as pictured in Fig.3.1, D^{ij} is

$$D^{ij} = \frac{1}{2}(\boldsymbol{n_x}^i \boldsymbol{n_y}^j + \boldsymbol{n_y}^i \boldsymbol{n_x}^j) = \boldsymbol{n_x}^i \boldsymbol{n_y}^j, \tag{3.21}$$

where $\boldsymbol{n_x}$ and $\boldsymbol{n_y}$ are the unit vectors pointing toward the x and y-direction. Substituting 2.24 and 3.21 into 3.20, the pattern function is obtained as below:

$$F^{+}(\Theta,\Phi,\Psi) = -\frac{1+\cos^2\Theta}{2}\sin 2\Phi\cos 2\Psi + \cos 2\Phi\cos\Theta\sin 2\Psi, \tag{3.22}$$

$$F^{\times}(\Theta,\Phi,\Psi) = \frac{1+\cos^2\Theta}{2}\sin 2\Phi\sin 2\Psi + \cos 2\Phi\cos\Theta, \tag{3.23}$$

where Ψ is the polarization angle, which is the rotation angle of GW polarization in the transverse plane. Please refer [42] for more details. This pattern function is as same as interferometric detectors.

3.3 Scientific Targets

Using the principle mentioned above, the TOBA is expected to detect low-frequency GWs, such as IMBHs and a stochastic GW background. In this section, we will explain about the example sensitivity required for the GW detection.

The example sensitivity for the GW detection is shown in Fig.3.3. It has two 10-m scaled test mass bars. Their angular fluctuations are read using Fabry-Perot cavity in order to reduce the shot noise of the sensor. Also, the suspension thermal noise should be reduced by cryogenic system.

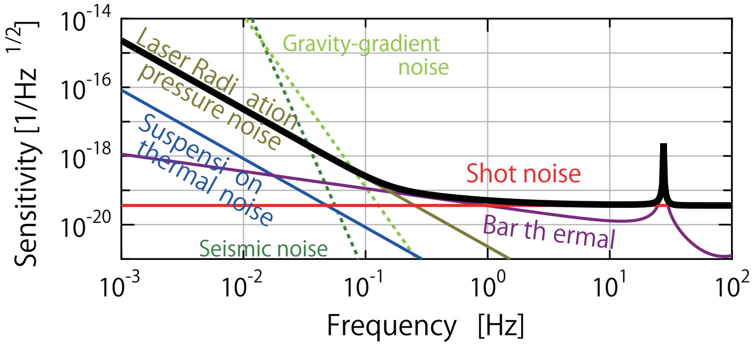

Figure 3.3: The example sensitivity of the ultimate TOBA. It has two bar-shaped test mass bars with a length of 10 m. The resonant frequency of the torsional mode is 1 mHz, and the test masses are suspended by the system with loss angle ϕ of 10^{-7}.

Fig.3.4 is the simulated observable distance for a merger of equal-mass binary system. It shows that the Ultimate TOBA will observe a merger of $10^5M.$ black holes at 10 Gpc with a signal to noise ratio (SNR) of 5. The observation of such intermediate-mass black holes will reveal how the super massive black holes evolved and how our galaxies evolved.

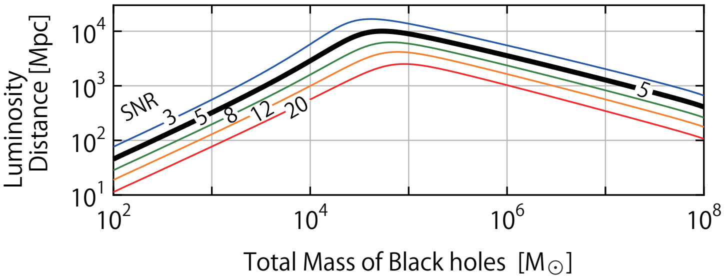

Figure 3.4: Simulated luminosity distance which ultimate TOBA will reach for a merger of equal-mass black holes with a each SNR.

Also, it will be possible to set an upper limit on a stochastic GW background. (See Fig.3.6.) Performing one-year simultaneous observation with the ultimate TOBAs, the upper limit will exceed the upper limit derived from the theory of the Big Bang Nucleosynthesis (BBN).

3.4 Previous Results

In order to reach the final sensitivity as shown in Fig.3.3, the detector should be developed step by step.

As a first step, the first prototype has been developed [38, 37]. It has a single test mass with the length of 20 cm. The main feature is that the test mass is magnetically levitated by the pinning effect of a superconductor, which realize the low-damping and low-loss suspension system.

The achieved sensitivity is shown in Fig.3.5. The sensitivity is limited by magnetic coupling effect caused by magnetic suspension system at low frequencies, and by seismic coupling noise at higher frequencies.

The principle test and the first observation are performed with this prototype. The first upper limit on a stochastic GW background at 0.2 Hz has been set with the single prototype TOBA [38]. Also, the upper limit is updated by a simultaneous observation with two prototypes set at Tokyo and Kyoto in Japan [48]. Figure 3.6 shows the upper limits obtained using the TOBAs and other detectors.

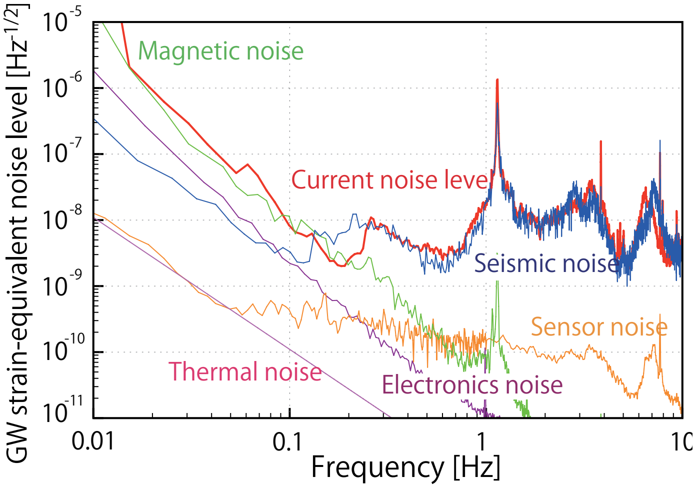

Figure 3.5: The sensitivity of the first prototype TOBA. The total sensitivity (red line) is limited by the seismic noise (the blue line) and the magnetic coupling noise (the green line).

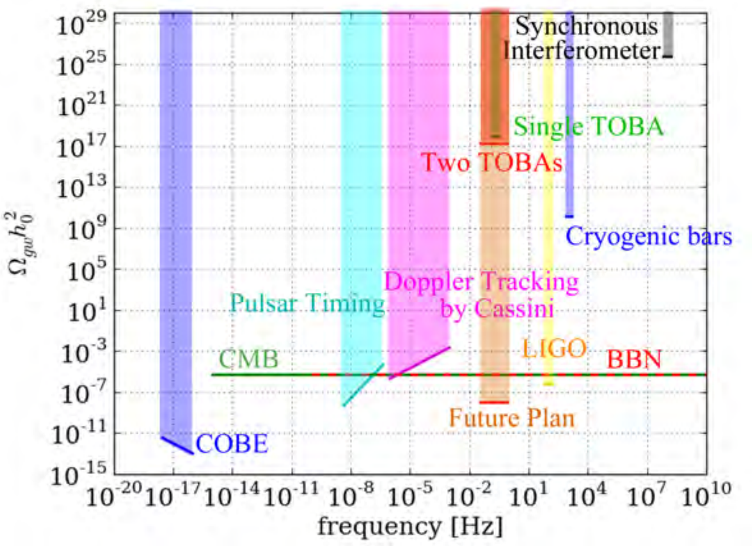

Figure 3.6: The upper limits on a stochastic GW background. TOBAs set an upper limit around 0.1 Hz, which had been unexplored region previously. The green line with the caption of 'Single TOBA' is obtained from the observation with the single detector. The red line with the caption of 'Two TOBAs' is obtained from the cross correlation analysis with the two TOBAs set at Tokyo and Kyoto in Japan, which enables to distinguish the noise and the stochastic GW signal. The line with caption 'future plane' is an estimated upper limit set by the 1-year simultaneous observation with the two ultimate TOBAs.

Chapter 4
Phase-II TOBA

We have developed *Phase-II TOBA* as a next step of the first prototype. As described in Sec.4.1, the main feature of Phase-II TOBA is the development of the new suspension system which realize a new observation system and seismic coupling noise reduction. In this chapter, we will explain about the method and the characteristics of the new observation system and the design of the Phase-II TOBA

4.1 Concept

The main purpose of the phase-II TOBA is to establish some of the technologies necessary for the detection of the low-frequency GWs using TOBA. In our setup, we established the new suspension system with four features:

- A multi-output system,
- A common mode noise rejection system,
- A passive vibration isolation system,
- An active vibration isolation system.

The multi-output system is the novel observation method which improves the angular resolution and the event rate by deriving three independent signals from a single detector. This system is realized by monitoring the vertical rotational mode of the test mass as well as the horizontal rotational mode. We introduce two test masses for the common mode noise reduction, and a suspended optical bench for the passive vibration isolation, and an active vibration isolation table (AVIT) for the seismic noise reduction at low frequencies. Though the rotational seismic vibration is too small to observe [50], the translational motion of the test masses couples to the rotational monitor as shown in Sec.3.4. Our suspension system have established the seismic isolation system for such seismic coupling noise.

See Fig.4.1 for the significance of the Phase-II TOBA in the road to the ultimate TOBA.

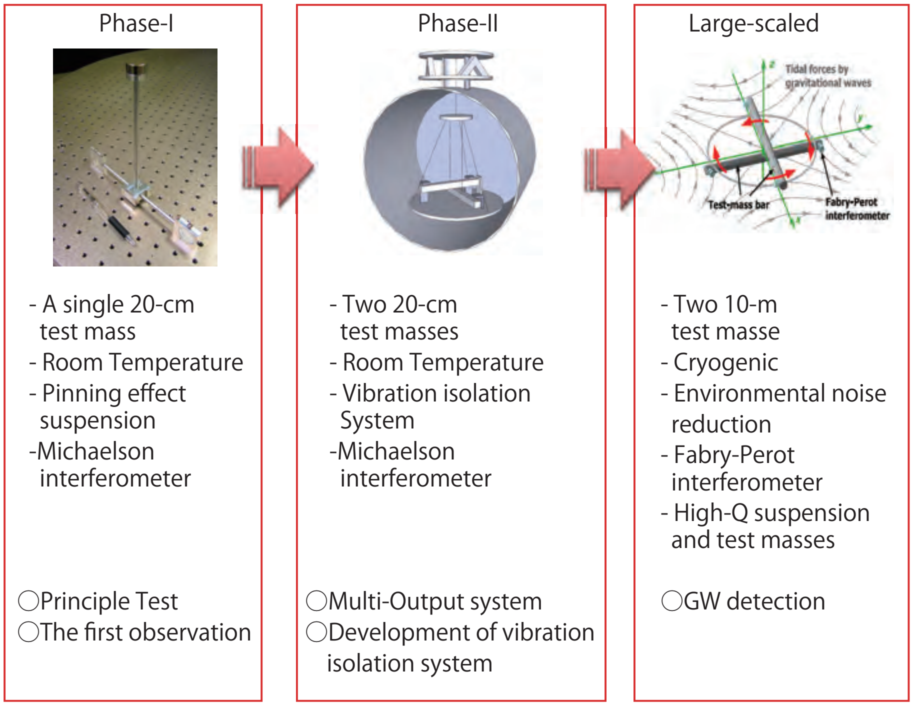

Figure 4.1: The road map of the TOBA project.

4.2 Multi-Output System

4.2.1 Method

In the Chapter 3, we explained about the principle to detect GWs using TOBA. There, we assume that the bars rotate only in the horizontal plane ($x-y$ plane). However, the test masses rotate in horizontal plane mainly by the GWs incoming along z axis. Considering the situation GWs coming from y axis, the test masses do not rotate in the horizontal plane but the test mass set along x axis rotates in $x-z$ plane (ϕ_1 in Fig.4.2). Therefore, we can obtain two independent signals from a single test mass bar by observing two rotational angular fluctuation θ_i and ϕ_i, where i is the index of the test masses.

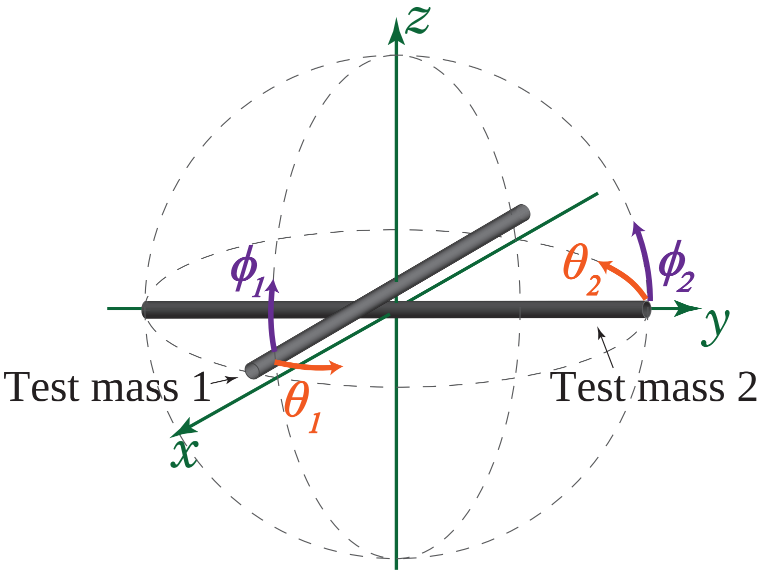

Figure 4.2: Schematic picture of multi-output TOBA in the proper antenna frame. The test masses rotate in the horizontal plane (θ_1 and θ_2) and in the vertical plane (ϕ_1 and ϕ_2).

The angular fluctuation ϕ_i obeys the equation of motion

$$I\ddot{\phi}_i(t) + \gamma_\phi \dot{\phi}_i(t) + \kappa_\phi \phi_i(t) = F_{\mathrm{gw}}, \tag{4.1}$$

which is basically the same as θ_i. In this case, κ_ϕ is derived as

$$\kappa_\phi = mgd, \tag{4.2}$$

where m, g, and d are the mass of the bar, the gravitational acceleration, and the distance between the center of mass of the bar and the suspension point. Therefore, the resonant frequency of ϕ_i, $f_{\phi_i 0} = \sqrt{mgd/I}/2\pi$, can be also as low as that of θ_i by adjusting the position of the center of mass.

Moreover, since we have two test masses, we can monitor 4 modes, $\theta_1, \phi_1, \theta_2$ and ϕ_2. Considering $\theta_1 = -\theta_2$ for the GW signals, TOBA can obtain three independent signals:

$$s_{\mathrm{I}} = (\theta_1 - \theta_2)/2, \tag{4.3}$$

$$s_{\mathrm{II}} = \phi_1, \tag{4.4}$$

$$s_{\mathrm{III}} = \phi_2, \tag{4.5}$$

without changing the setup drastically but only with additional sensors for ϕ_1 and ϕ_2.

4.2.2 Antenna Pattern Function

As well as 3.21, the detector tensors for each signal is written as

$$\begin{aligned} D_I^{ij} &= \boldsymbol{n_x}^i \boldsymbol{n_y}^j, && (4.6)\\ D_{II}^{ij} &= \frac{1}{2}\boldsymbol{n_x}^i \boldsymbol{n_z}^j, && (4.7)\\ D_{III}^{ij} &= \frac{1}{2}\boldsymbol{n_y}^i \boldsymbol{n_z}^j. && (4.8) \end{aligned}$$

Therefore, the antenna pattern functions for each signal are

$$\begin{aligned} F_{\mathrm{I}}^{+}(\Theta,\Phi,\Psi) &= \frac{1+\cos^2\Theta}{2}\sin 2\Phi\cos 2\Psi - \cos 2\Phi\cos\Theta\sin 2\Psi, && (4.9)\\ F_{\mathrm{I}}^{\times}(\Theta,\Phi,\Psi) &= \frac{1+\cos^2\Theta}{2}\sin 2\Phi\sin 2\Psi + \cos 2\Phi\cos\Theta, && (4.10)\\ F_{\mathrm{II}}^{+}(\Theta,\Phi,\Psi) &= \frac{1}{2}\sin 2\Theta\sin\Phi\cos 2\Psi - \sin\Theta\cos\Phi\sin 2\Psi, && (4.11)\\ F_{\mathrm{II}}^{\times}(\Theta,\Phi,\Psi) &= \frac{1}{2}\sin 2\Theta\sin\Phi\sin 2\Psi + \sin\Theta\cos\Phi\cos 2\Psi, && (4.12)\\ F_{\mathrm{III}}^{+}(\Theta,\Phi,\Psi) &= \frac{1}{2}\sin 2\Theta\cos\Phi\cos 2\Psi - \sin\Theta\sin\Phi\sin 2\Psi, && (4.13)\\ F_{\mathrm{III}}^{\times}(\Theta,\Phi,\Psi) &= \frac{1}{2}\sin 2\Theta\cos\Phi\sin 2\Psi + \sin\Theta\sin\Phi\cos 2\Psi. && (4.14)\\ & && (4.15) \end{aligned}$$

Figure 4.3 is the square root of the each antenna pattern functions:

$$F_i = \left(F_i^{+2} + F_i^{\times 2}\right)^{1/2}, \qquad (4.16)$$

and their total,

$$F_{\text{total}} = \left(\sum_{i=I,II,III} r_i F_i^2\right)^{1/2}. \qquad (4.17)$$

Here, r_i is the distance at which the source would be observed with the same SNR in a single output. The antenna patterns shown in Fig.4.3 is pictured under the assumption of $r_1 = 1, r_2 = r_3 = 0.5$ since the sensitivity of s_{I} is expected to be twice as good as s_{II} and s_{III} due to the common mode noise rejection. It shows the blind direction which the conventional single-output TOBA has is vanished for the multi-output TOBA.

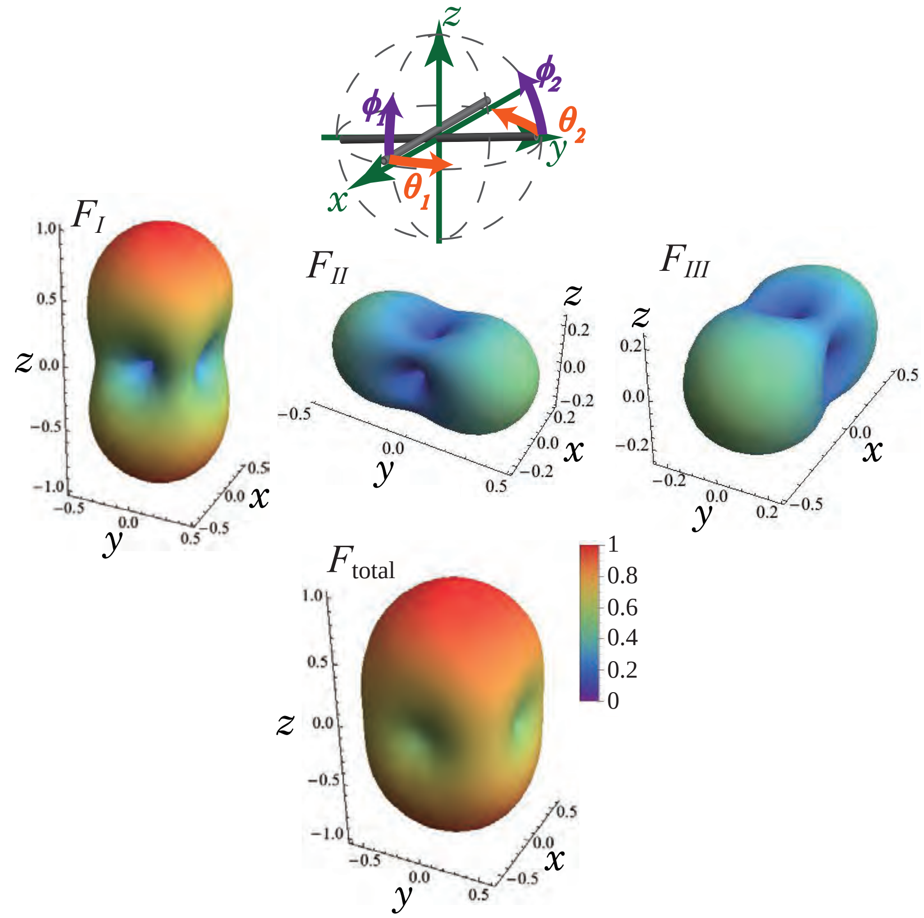

Figure 4.3: Square root of the antenna pattern functions of multi-output TOBA. The single-output TOBA has only the antenna response of F_{I}. By adding two signals s_{II} and s_{III} with the antenna pattern function of F_{II} and F_{III}, the blind direction is vanished and the region where TOBA can observe is enlarged (F_{total}). Note that we assume that the sensitivity of s_{I} is twice as good as s_{II} and s_{III} because of the common mode noise rejection, and that the sensitivity of s_{II} and s_{III} are the same.

4.2.3 Detection Volume

As shown in Fig.4.3, the volume enclosed by the sphere of the antenna pattern function is enlarged. It means that the area which the TOBA can observe is enlarged and the event rate is increased.

We will estimate the increased event rate with *the detection volume*, [47] defined as

$$V_N = \int d\Omega \int_0^{R_N(\alpha,\delta)} r^2 dr. \tag{4.18}$$

$R_N(\alpha, \delta)$ is its reach of the TOBA's observable area at each sky position α, δ:

$$R_N(\alpha, \gamma) = \frac{D}{\rho_{\text{min}}} \left[F_N(\alpha, \delta) \right]^{1/2}, \tag{4.19}$$

where D and rho_{min} are the distance to which the detector can detect GWs with a unit SNR, and the minimum value of SNR with which we can regard that GWs are detected. F_N is the square root of the pattern functions as is written in 4.16 and 4.17. In this case, we have $N = \text{I}, \text{II}, \text{III}$, and total.

For the convenience, we take $D = \rho_{\text{min}} = 1$ in order to compare the detection volume between the single-output and the multi-output TOBAs. Then, the detection volume is derived to be $V_I = 1.2$ for the single output, and $V_{\text{total}} = 2.0$ for the three outputs. Therefore, the detection volume, i.e., the event rate will be about 1.7 times larger than the conventional configuration when we have three independent signals.

4.2.4 Angular Resolution

The conventional GW detectors cannot identify the direction of the GW source because of their low directivity. It is known that at least three separate detectors are necessary for the identification. [47] Moreover, the time-of-flight method, which is used for ground-based interferometric detectors, is not effective to GWs whose wavelength is longer than the distance between detectors any more [1].

Since the multi-output method derives the three independent signals, it improves the accuracy of the identification. However, because of the geometrical symmetry of the detector, the single multi-output TOBA cannot identify the source as one point in all sky, but narrow down to one point in one quadrant, i.e., 8 points. In

---

[1] The wavelength of the GWs at 1 Hz is about 3×10^8 m, which is about the distance between the Earth and the moon. The second TOBA should be placed on the moon in order to get useful constrains from the time-of-flight method.

order to identify the source as one point, simultaneous observation with at least two multi-output TOBAs, or follow-up observation using the electro-magnetic waves is necessary.

Figure 4.4 is the angular resolution of the multi-output TOBA and the single-output TOBA. The angular resolution is estimated using Fisher analysis [31]. The GW source is assumed to be a monochromatic sources. It shows that the multi-output TOBA can narrow down the sky position of the GW sources of the 8 points with the error of 4×10^{-1} steradian, while single-output TOBA cannot determined the sky position at all if the observation time is shorter than 1 day. The single- and multi-output TOBA can determine the sky position of the GW sources if the observation time is longer than 1 day since the signal is modulated by the Earth's rotation. Also, the other parameters of GW source are proven to be determined with multi-output TOBA even though the observation time is shorter than 1 day [29].

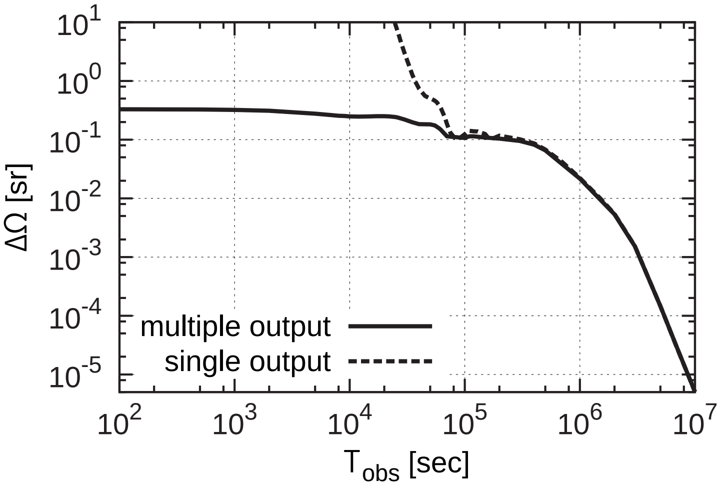

Figure 4.4: The angular resolution $\Delta\Omega$ vs the observation time T_{obs}. The frequency of the GW source is assumed to be 1 Hz, and the amplitude is normalized by SNR = 10.

Other than the monochromatic sources, we have investigated the angular resolution for the IMBH binaries. For example, the angular resolution for the $10^4 M.$ - $10^4 M.$ binaries are improved to be 6.74×10^{-2} steradian.

See [29] for more details of the Fisher analysis and the calculation. Please note that these Fisher analysis are calculated by Kazunari Eda.

4.3 Design Overview

As described in Sec.4.1, we developed the phase-II TOBA focusing on the suspension system.

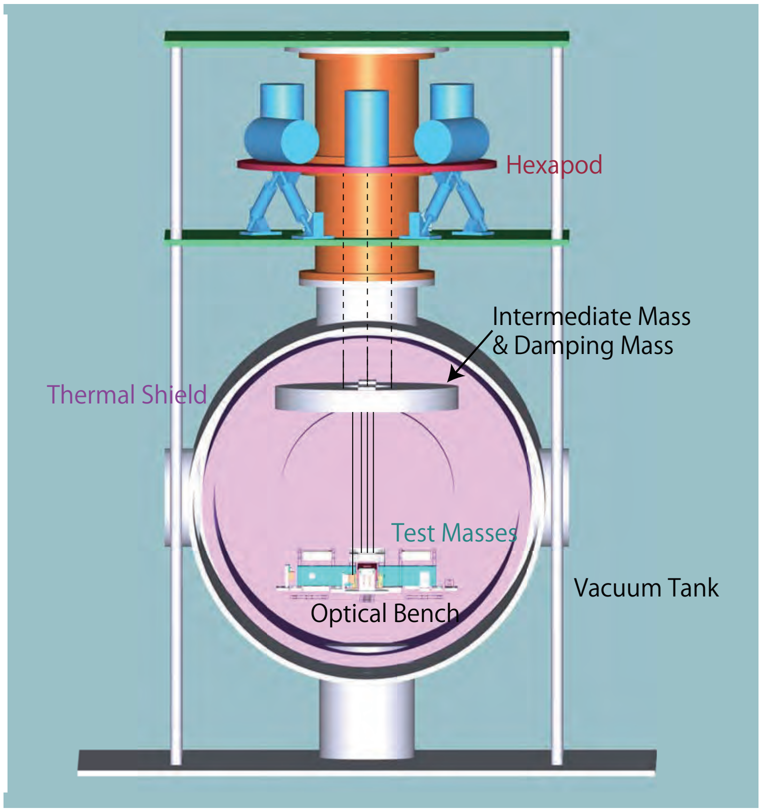

Figure 4.5: A picture of the hole setup.

The schematic view of the Phase-II TOBA is shown in Fig.4.5. The two test masses which sense the GWs are suspended from a Hexapod-type active vibration isolation table (AVIT) via an intermediate mass which is magnetically damped by a damping mass. The suspension system except the actuators and sensors of the AVIT is in a vacuum tank. The vacuum tank has the cryogenic system so that the suspension wires and test masses can be cooled down to 4 K in order to reduce the thermal noise, while the cryogenic system is not used for the Phase-II TOBA.

4.4 Suspension

4.4.1 Test Masses

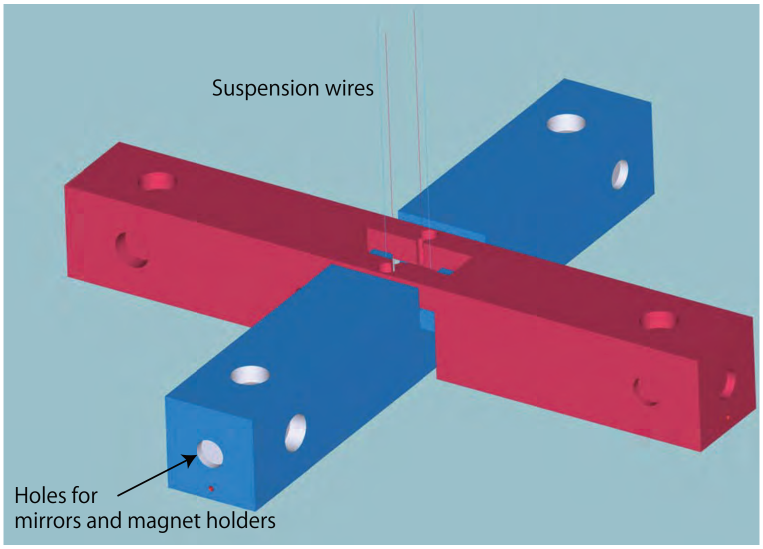

Figure 4.6: A picture of the two test masses.

The picture of the test masses is shown in Fig.4.6. The test masses are designed to realize the multi-output system and the common mode noise rejection. The length of the test mass is maximized to be 24 cm under the constraint of the size of the vacuum tank which is also used for the first prototype.

From 4.1 and 4.2, the resonant frequency in the vertical rotational mode is written as $f_0 = \sqrt{mgd/I}/2\pi$. Therefore, the suspension points of the test masses are set to be as close as possible to their center of mass so that the resonant frequency of the vertical rotation is minimized. In addition, the test masses have tapped holes for counter masses at the both ends of the bar in order to adjust the position of the center of mass to the suspension points. Note that the suspension points should be a little bit higher ($\sim$ 0.1mm) than the center of the mass for its stability.

The each test mass is suspended by two parallel wires so that the centers of mass of the two test masses are at the same point in order to maximize the common mode noise rejection rate. The expected common mode noises rejection rate is $\sqrt{2}$ in strain at the minimum where the noise sources of the two signals are independent. The maximum common mode noise rejection rate is expected to be more than 10 when the noises are correlated.

However, the resonant frequency in the horizontal rotational mode increases due to the suspension using the parallel two wires. When the test mass with the mass of m suspended by two wires rotates by the angle θ in the horizontal plane, the force applied at the suspension point is written as

$$F = \frac{mg\phi}{2}, \tag{4.20}$$

where $\phi = a\theta/l$ is the inclination angle of the suspension wire (See Fig.4.7). Here, a and l is the distance between the two suspension points divided by 2 and the length of the suspension wire, respectively. The equation of motion in the horizontal plane is

$$I\ddot{\theta} + \gamma\dot{\theta} = 2Fa = -mg\frac{a^2}{l}\theta, \tag{4.21}$$

where I is the moment of inertia. Therefore, the resonant frequency in the horizontal plane in our test mass is obtained as

$$f_{\theta 0} = \frac{1}{2\pi}\sqrt{\frac{mg}{I}\frac{a^2}{l}}. \tag{4.22}$$

It means that the resonant frequency is relative to the distance between the two suspension points. In our setup, a is set to be as small as possible in order to reduce the resonant frequency, which is limited by the size of screws under the constraint of the position of the two test masses.

The each test mass is composed of three parts: a set of wire clamps, and two bar-shaped parts. We set clamps and suspension wires at first, then the arms are attached to the clamp. Our configuration enables us to assemble the test mases at proper place without touching each other. Though the loss of the test mass is increased, i.e., the thermal noise of the test mass bar is increased, the thermal noise does not affect to the sensitivity in our setup. The material of the bar-shaped parts is aluminum since it does not magnetized and is easy to manufacture. The set of clamps are made of stainless steel, which is harder than the suspension wires, in order to clamp the suspension wires rigidly.

The material of the suspension wires is tungsten. Considering the weight limit, the constraint on the diameter of the wire d is

$$d > 2\sqrt{\frac{amg}{\pi T}}, \tag{4.23}$$

where a, m, g and T are the safety factor, the mass, the gravitational acceleration, and the ultimate tensile strength of the wire, respectively. Setting $a = 2$, the

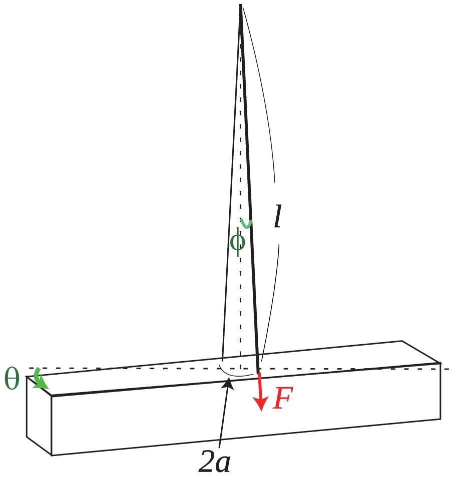

Figure 4.7: A schematic view of the rotating test mass in the horizontal plane.

diameter of the wire should be $d > 7.1 \times 10^{-5}$ m. Chosen from ready-made items, the diameter of the wires for the test mass is 0.1 mm.

See Table 4.1 for the details of the test mass properties.

4.4.2 Optical Bench

An optical bench is a table on which sensors and actuators are set. The optical bench is also suspended from the same intermediate mass. Since we measure the distance between the sensors and test masses, the seismic motion of the sensors couples to the signals effectively even though the test masses are well isolated from the seismic noise. Therefore, the seismic motion of the sensors and actuators should also be isolated from the vibration.

Here, we will explain how the seismic noise is reduced by the suspended optical bench. The equation of motion for the test mass with mass of m_{TM} suspended by wire with length of l_{TM} is

$$m\ddot{x}_{\mathrm{TM}}(t) + \gamma_{\mathrm{TM}}\dot{x}_{\mathrm{TM}}(t) + \frac{m_{\mathrm{TM}}g}{l_{\mathrm{TM}}}\left(x_{\mathrm{TM}}(t) - X(t)\right) = 0, \qquad (4.24)$$

where γ_{TM} and g are the damping constant and the gravity acceleration. $x_{\mathrm{TM}}(t)$ and $X(t)$ are the horizontal displacement of the test mass and the suspension point, respectively. Performing Fourier transformations, we have

$$\left(-\omega^2 m_{\mathrm{TM}} + i\gamma_{\mathrm{TM}}\omega + \frac{m_{\mathrm{TM}}g}{l_{\mathrm{TM}}}\right)\tilde{x}_{\mathrm{TM}}(t) = \frac{m_{\mathrm{TM}}g}{l_{\mathrm{TM}}}\tilde{X}(t) \tag{4.25}$$

$$\therefore \quad \tilde{x}_{\mathrm{TM}}(t) = \frac{\omega_{0\mathrm{TM}}^2}{-\omega^2 + i\frac{\omega_{0\mathrm{TM}}}{Q_{\mathrm{TM}}}\omega + \omega_{0\mathrm{TM}}^2}\tilde{X}(t), \tag{4.26}$$

where $\omega_{0\mathrm{TM}} = \sqrt{g/l_{\mathrm{TM}}}$ is the resonant frequency and $Q_{\mathrm{TM}} = \omega_{0\mathrm{TM}}/\gamma_{\mathrm{TM}}$ is the Q factor. Here, tilde denotes the Fourier transformations of the corresponding variables. The same equation is formed for the optical bench:

$$\tilde{x}_{\mathrm{OB}}(t) = \frac{\omega_{0\mathrm{OB}}^2}{-\omega^2 + i\frac{\omega_{0\mathrm{OB}}}{Q_{\mathrm{OB}}}\omega + \omega_{0\mathrm{OB}}^2}\tilde{X}(t). \tag{4.27}$$

Therefore, the relative motion between the test mass and the optical bench is

$$\tilde{x}_{\mathrm{TM}}(t) - \tilde{x}_{\mathrm{OB}}(t) = H(f)\tilde{X}(t), \tag{4.28}$$

where

$$H(f) = \frac{\omega_{0\mathrm{TM}}^2}{-\omega^2 + i\frac{\omega_{0\mathrm{TM}}}{Q_{\mathrm{TM}}}\omega + \omega_{0\mathrm{TM}}^2} - \frac{\omega_{0\mathrm{OB}}^2}{-\omega^2 + i\frac{\omega_{0\mathrm{OB}}}{Q_{\mathrm{OB}}}\omega + \omega_{0\mathrm{OB}}^2}. \tag{4.29}$$

$H(f)$ is the transfer function of the seismic motion from the suspension point to sensors. $1/H(f)$ is the passive seismic vibration isolation rate.

Figure 4.8 is the graph of the $H(f)$. At lower frequencies than the resonant frequencies, the test masses and the optical bench move commonly so that the seismic noise appeared in the sensor is rejected. On the other hand, the transfer function is small above the resonant frequencies since the motion of the test masses and the optical bench are both reduced. $H(f)$ gets smaller when the difference between $\omega_{0\mathrm{TM}}$ and $\omega_{0\mathrm{OB}}$ is smaller since the transfer functions of the test masses and the optical bench get closer. In order to reduce the seismic motion, it is effective to adjust the two resonant frequencies to be close.

The material of the optical bench should be metal since the bench should be rigid in order to avoid the resonance of the optical bench affect the sensitivity. Here, we use aluminum for the table and stainless steel for the clamps by the same reason as the test mass clamps.

Note that the extension caused by the tensile stress does not affect the operation. In our case, the extension of the test mass wires is 4.0×10^{-4} m while the extension of the optical bench wires is 6.7×10^{-4} mm, assuming that the wire lengths of the test mass and the optical bench are 0.36 m and 0.38 m, respectively [2].

---

[2] The Young's modulus of the tungsten is $E = 345$ GPa.

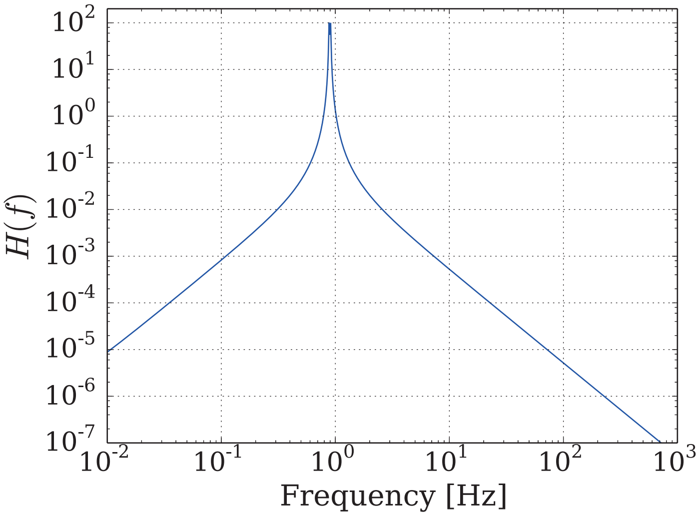

Figure 4.8: The transfer function of the horizontal motion from the suspension point to the sensors. We assume $l_{\mathrm{TM}} = 30$ cm, $l_{\mathrm{OB}} = 32$ cm, and $Q_{\mathrm{TM}} = Q_{\mathrm{OB}} = 100$. In this condition, the resonant frequency of the test mass and the optical bench are $f_{0\mathrm{TM}} = 0.91$ Hz and $f_{0\mathrm{OB}} = 0.88$ Hz, respectively.

4.4.3 Intermediate Mass and Damping Mass

We have the damping system so that the peaks of the pendulum modes do not effect on the sensitivity, the control system, and so on.

The intermediate mass, which is made of aluminum, is covered by the damping mass which has damping magnets inside. The magnets are attached by its magnetic force since the damping mass is made of ferromagnetic stainless. When the magnets are close enough to the intermediate mass, the movements of the intermediate mass is dumped because of the loss caused by eddy current in the aluminum. In this case, the magnets are arranged in a circle so that the loss in the horizontal rotation is reduced while the other modes are well damped.

The test masses and the optical bench are suspended from the intermediate mass. It lets the magnetic coupling noise caused by the damping magnets smaller than setting the damping system directly on the test masses and the optical bench.

Test Mass		
The length of the bar	240	mm
The mass	0.61	kg
The moment of inertia (in both yaw and roll)	3.34×10^{-3}	kg m^2
The quadrupole moment	3.20×10^{-3}	kg m^2
The distance between the suspension points (a)	17	mm
The length of the suspension wires	400	mm

Optical Bench		
The mass	4.4	kg
The moment of inertia (in yaw)	6.17×10^{-2}	kg m^2
The moment of inertia (in roll/pitch)	3.50×10^{-2}	kg m^2
The quadrupole moment (in roll/pitch)	3.08×10^{-2}	kg m^2
The distance between the suspension points	45	mm
The length of the suspension wires	400	mm

Table 4.1: The main property of the suspension system.

4.5 Control System

4.5.1 Control Loop

The test masses are controlled by sensors and actuators set on the optical bench. Servo system provides the linearity of the sensors and actuators. It enables us to calibrate the small signals properly.

Block diagram of the control system for the test masses is shown in Fig.4.9. We have two sensors: fiber laser interferometers for the main observation, and photo sensors for the alignment. The displacement signals measured by the sensors go to coil magnet actuators after filtered by the digital system. The digital system is a powerful tool for the control system with multi-degrees of freedom. The details of the digital system is described in Sec.4.8.

In this subsection, we will explain the principle of the control system. Assuming that the GW signals h is injected in the test mass, for example, the total force x applied on the test mass is written as

$$x = h - M S_i F_i A x, \tag{4.30}$$

where i =LS or PS is the indicator of the servo loop. M, S_i, F_i and A are the transfer function of the test mass from force to the displacement, that of sensors, that of

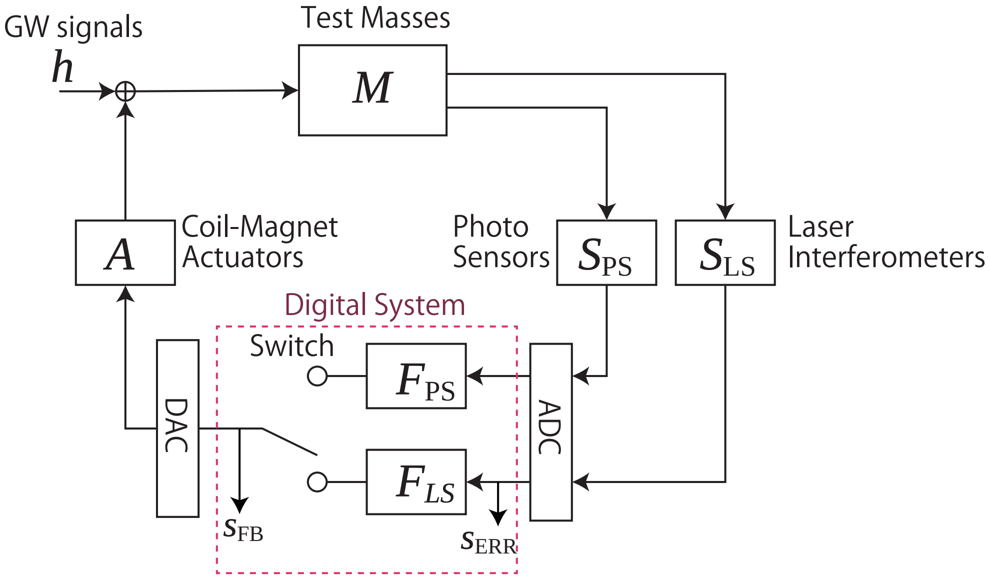

Figure 4.9: The control system of the test masses. We have two sensors: photo sensors (PS) and laser interferometers (LS). The GW signals are injected into the test masses and sensed by sensors via transfer function H, which is expressed in 3.17 and 3.18. The signals from the sensors go to the digital system via analog-to-digital converter (ADC). On and Off of the control loop is selected in the digital system. The selected feedback signals s_{FB} come out from the digital-to-analog converter (DAC) and go to the coil-magnet actuators.

filters, and that of actuators, respectively. Defining the open loop transfer function (OLTF) G_i as

$$G_i = MS_iF_iA, \tag{4.31}$$

x is derived as

$$x = \frac{1}{1+G_i}s. \tag{4.32}$$

Therefore, the displacement of the test mass is suppressed by $1+G_i$ times where G_i is bigger than one. We call the frequency where the absolute value of G_i is one as the unity gain frequency (UGF). UGF represents the minimum frequency that the object is controlled.

Meanwhile G_i should be large enough to maintain the linearity of the sensors and actuators, G_i is required to satisfy Nyquist stability criterion [62] in order to stabilize the control system. Plotting a Nyquist diagram of G_i, where the real part of G_i is plotted on the x axis and the imaginary part of G_i is plotted on the y axis when the frequency is swept from 0 to ∞, the control system is stable if the point $(-1, i0)$ is on the left hand side of G_i when the frequency is swept from 0 to ∞ (Fig.4.10). Here, phase margin is one of the indicators for the stability of the servo system. The phase margin is the angle of G_i from $-180°$ at the UGF. It represents how close G_i is from the point $(-1, i0)$. If there is little phase margin, the servo system is not stable and easily oscillate. The phase margin should be more than about 20° for the stable control.

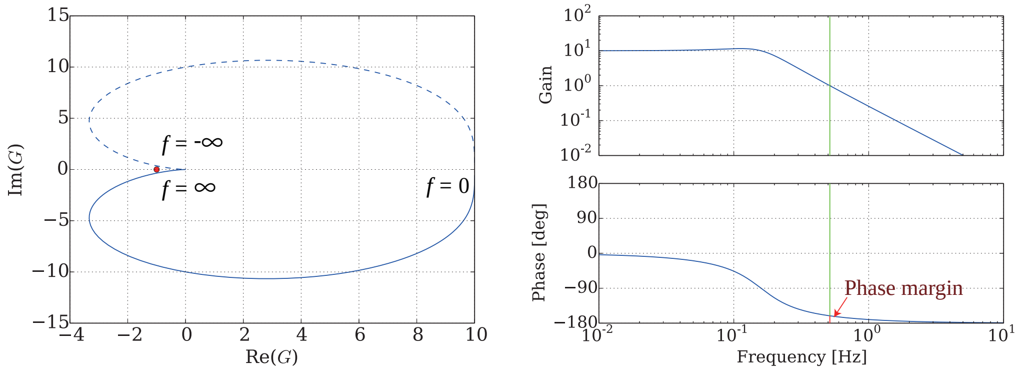

Figure 4.10: An example of a Nyquist plot (left) and a bode plot (right). In the both graph, a function $G = 10/(s^2+s+1)$ is plotted as an example, where $s = i2\pi f$. The green line shows the UGF. This system is stable since the point (-1, i0), which is plotted as a red circle, is left hand side of G and the phase margin is about 20°.

4.5.2 Photo Sensors

When the test mass is swinging freely and moves a lot in total root means square (RMS), it is difficult to keep the visibility stable enough for locking the interferometers since the interferometer does not have wide dynamic range and the laser beams of the interferometer do not aligned while it has good sensitivity. Therefore, we use location sensors called photo sensors (PSs) in order to fix the relative position between the test masses and the optical bench (the output ports of the laser beams).

The PSs are composed of one LED and two photo detectors as shown in Fig.4.11, and measure the distance to the object by sensing the amount of LED right reflected at the object. They have a larger dynamic range, but worse sensitivity than interferometers.

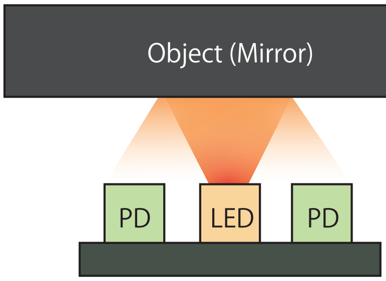

Figure 4.11: Schematic View of the photo sensors.

In our setup, we do not use mirrors for PSs since the LED light is reflected by the aluminum surface enough and the PSs are required to be stable only for the lock acquisition. The current noise level of the PSs are about $10^{-8}\mathrm{m}/\sqrt{\mathrm{Hz}}$, which is stable enough that the fluctuation of the fringe of the Michelson interferometer is within 5 %.

4.5.3 Laser Interferometers

The main sensors we used for the observation in Phase-II TOBA is the Michelson interferometric sensors. The sensor is switched from the photo sensors to interferometers after locking the test masses with photo sensors.

In order to decouple each mode and to reduce the coupling from the translational seismic noise as seen in the first prototype, we monitor two pendulum modes as well as two rotational modes, LONG, SIDE, YAW, and ROLL, using four interferometers, LS1 to LS4. (See Fig.4.12 for the definition of an each mode.) We do not monitor VERT (vertical) and PITCH mode since their motion is smaller than others due to their high resonant frequencies.

In the Phase-II TOBA, we used the fiber optics in order to compose the Michelson interferometers in order to save the space. The laser fibers are suitable for our setup in which many sensors are necessary though phase noise will be injected from fibers vibration. The laser beam is introduced by a single bare-fiber, and the beam is split in to 8 fibers by fiber beam splitters on the optical bench. The eight beams goes to the fiber laser interferometers shown in Fig.4.12. The one end of LS1, LS2, and LS3 are retroreflector patch fiber cables, which work as fixed reference mirrors, and the other is the mirror attached on the test mass. The roll motion (LS4) is monitored by measuring the difference of the distance from the output ports of laser beam to the mirrors at the top of the test mass between the two beam paths. The interfere of the returning beams are measured by the photo detectors. The photo detectors are on the optical bench, and the signals are derived via lead cables from the optical bench.

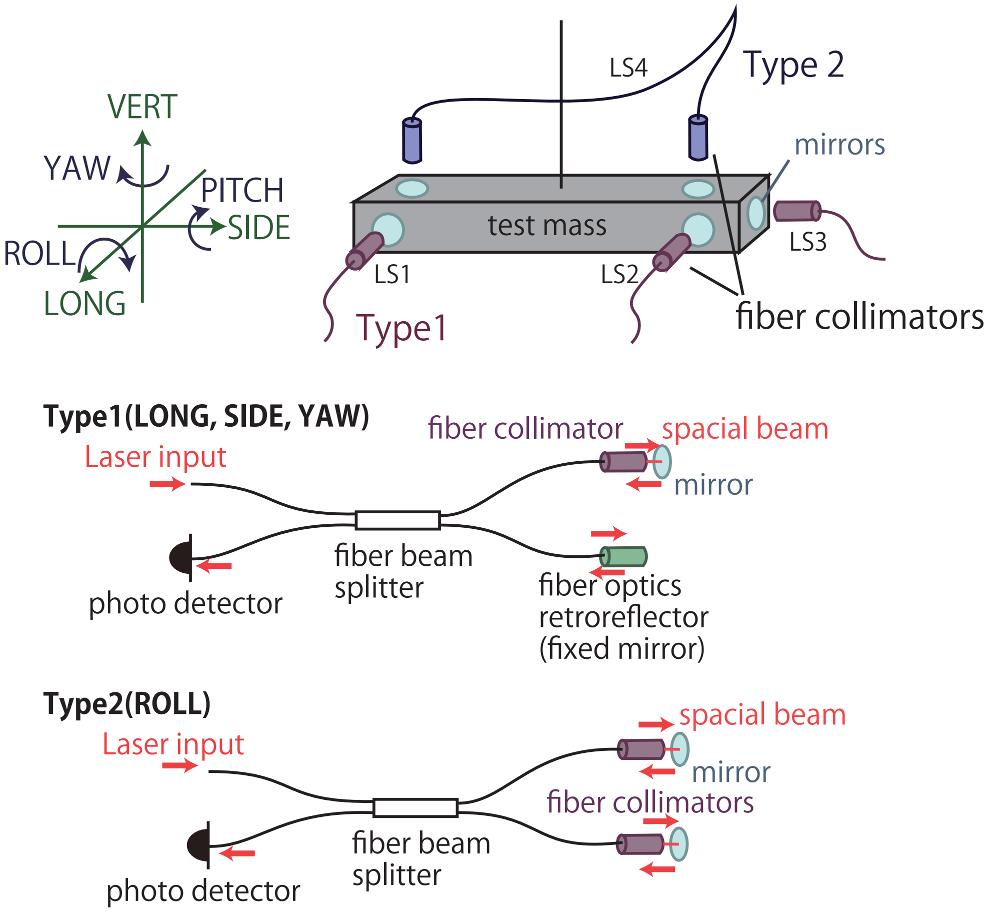

Figure 4.12: The configuration of the fiber laser interferometers.

In our setup, we use the interferometers at their mid-fringe. The electromagnetic field of the input beam is written as

$$E_{\text{in}} = E_0 e^{-i\Omega t}, \tag{4.33}$$

where E_0 and Ω is the amplitude and the angular frequency of the laser. The input beam goes to the fiber beam splitter (BS) and divided into two fibers. The beams are reflected by end mirrors attached on the test mass or fiber retroreflectors, and

Figure 4.13: The picture of the sensor module. The left one is the fiber collimator mounted on the half inch mirror mount, and the right one is the photo sensor.

recombined on the BS. Letting the optical pass lengths from the BS to the two ends as l_1 and l_2, the electromagnetic field of the recombined beam is

$$E_{\mathrm{PD}} = E_1 e^{-i(\Omega t - 2kl_1)} - E_2 e^{-i(\Omega t - 2kl_2)}, \tag{4.34}$$

where E_1 and E_2 are the amplitudes of the returning beams. k is the wave number of the beam. Therefore, the power of the light which the photo detector received is

$$\begin{aligned} P_{\mathrm{PD}} &= |E_{\mathrm{PD}}|^2 & (4.35)\\ &= \frac{P_{\max} + P_{\min}}{2} + \frac{P_{\max} - P_{\min}}{2} \cos(2k\delta l), & (4.36) \end{aligned}$$

where

$$\begin{aligned} P_{\max} &= (E_1 + E_2)^2, & (4.37)\\ P_{\min} &= (E_1 - E_2)^2, & (4.38)\\ \delta l &= l_2 - l_1. & (4.39) \end{aligned}$$

Since $\cos(2k\delta l) \sim 0$ around the mid-fringe, we obtain

$$P_{\mathrm{PD}} \sim \frac{P_{\max} + P_{\min}}{2} + \frac{P_{\max} - P_{\min}}{2} \frac{4\pi}{\lambda} \delta l \tag{4.40}$$

by taking the first order of δl in 4.36. Here, λ is the wavelength of the laser. Though $E_1 = E_2$ for the ideal case, E_1 and E_2 are not the same in the actual setup. Then, we define the visibility V_{LS} as

$$V_{\mathrm{LS}} = \frac{P_{\mathrm{max}} - P_{\mathrm{min}}}{P_{\mathrm{max}} + P_{\mathrm{min}}}. \tag{4.41}$$

When $V_{\mathrm{LS}} = 1$, $E_1 = E_2$ and there are no loss in the two beam paths. V_{LS} get smaller as the optical loss is larger.

In our setup, the wavelength of the laser is 1550 nm. The power of the laser is 500 mW in total. Since the laser is equally divided into 8 interferometers, the input power of the each interferometers is 62.5 mW.

Figure 4.13 is the picture of the fiber collimator (the output port of the laser beam) and the PS. The bases is original for the Phase-II TOBA instead of the ready-made pedestal bases in order to save the space.

4.5.4 Coil-Magnet Actuators

We use the coil-magnet actuators for the test mass control, which is one of the most typical actuators used in GW detectors. The coil-magnet actuator consists of a pin magnet attached on a test mass and a coil set on the optical bench. The magnetic field produced by the coil applies the force on the test mass via the magnet.

Compared to other actuators such as an electrostatic actuator [45], the coil-magnet actuators can produce relatively strong force as well as is easy to handle with. However, the environmental magnetic field also applies the force on the test mass and would reduce the sensitivity. In our setup, the coil-magnet actuators are adopted since the priority is given to the simplicity than the magnetic coupling noise reduction.

In our setup, the pin magnets are neodymium magnets with the length of 5 mm and the diameter of 1 mm. The coil has the self-inductance of 0.14 mH and the resistance of 11 Ω. The bobbin of the coil is made of Polyether ether ketone (PEEK) in order to avoid the eddy current flowing and suppress deterioration of a degree of vacuum.

4.6 Active Vibration Isolation Table

In the previous sections, we explain about the passive vibration isolation system using the pendulum. However, as shown in Fig.4.8, the seismic noise around the resonant frequencies of the pendulum mode is not reduced by the passive vibration isolation system. Therefore, we introduced the Hexapod-type active vibration isolation table (AVIT) in order to reduce the seismic noise around 1 Hz.

The AVIT is a table with six legs made of piezoelectric elements (PZT). The position of the table can be controlled by applying the voltage on the PZTs. The seismic motion of the table is suppressed by a feedback control using the seismometer set on the table as the sensors, and the PZTs as the actuators. The table is compact such as the diameter of 45 cm, but has a good vibration isolation rate around a few Hz, while a passive vibration isolation system needs a large setup, such as long suspension wires and GAS filters [19] and so on, in order to obtain a high vibration isolation rate at low frequencies. Also, the AVIT can suppress the vibration introduced from other than the ground, such as the vibration of a cryogenic anchor. Using the passive vibration isolation system, another intermediate mass with large mass to which the anchor is attached is necessary in order to reduce the introduced vibration of the cryogenic cooler as planned in bKAGRA [20].

A schematic view of the AVIT is shown in Fig.4.14. Hexapod-type AVIT has six legs with piezoelectric elements in them so that the length of the legs are changeable. Seismometers and the photo sensors are used for monitoring the vibration and the DC position of the table. These signals are fed back to the piezoelectric elements so that the seismic motion is canceled.

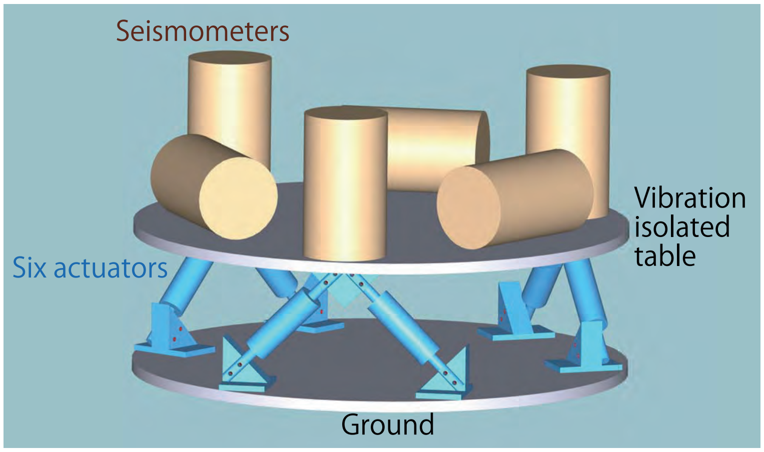

Figure 4.14: The schematic view of the Hexapod-type AVIT. It has six piezoelectric actuators as legs, which move the top table in any directions.

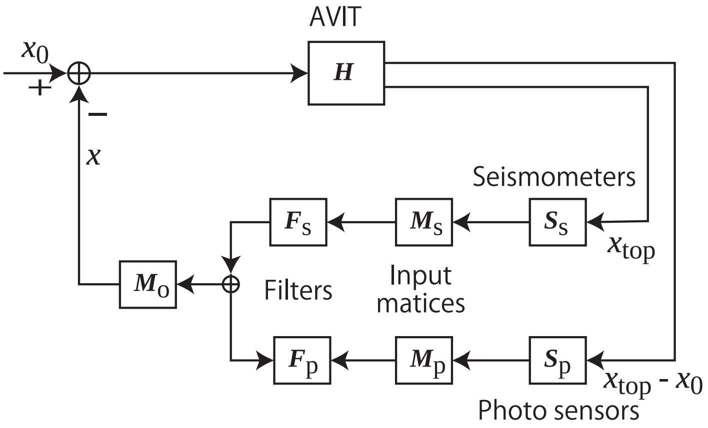

Figure 4.15: The control loop of the hexapod. Note that it describes the control loop only in one degree of freedom for the simplification.

4.6.1 Control System

Control Loop

The block diagram of the control loop is shown in Fig.4.15. In this control loop, two sensors, PSs and seismometers, are used at the same time. The seismometers are used for sensing the seismic motion of the table, while the PSs are used for sensing the absolute distance between the controlled table and the ground. The outputs of the sensors are gathered into the digital system and converted to the signals of each degree of freedom. Details of the method how the signals are converted are discussed in Appendix A. The output signals of the seismometer are the absolute vibration of the top table (x_{top}) while the PSs sense the relative movements between the top table and ground ($x_{\mathrm{top}} - x_0$). Each signal is filtered, then combined. The feedback signal are sent to the PZTs after being converted to actuation signals by an output matrix M_{o}.

In this control loop, the open loop transfer functions of each sensors are

$$G_s = S_s M_s F_s \tag{4.42}$$
$$G_p = S_p M_p F_p, \tag{4.43}$$

and overall open loop transfer function is

$$G = G_s + G_p. \tag{4.44}$$

The motion of the top table x_{top} can be written as

$$\begin{cases} x_{\text{top}} = x_0 - x & (4.45) \\ x = G_s x_{\text{top}} + G_p(x_{\text{top}} - x_0) & (4.46) \end{cases}$$

$$\therefore x_{\text{top}} = \frac{1+G_p}{1+(G_s+G_p)} x_0. \tag{4.47}$$

Therefore, the vibration reduction rate R is

$$R = \frac{1+(G_s+G_p)}{1+G_p}. \tag{4.48}$$

The gain of the control loop is adjusted so as to be $R > 10$ at 1 Hz in order to reduce the seismic motion by 10 times.

Seismometers

L4 seismometers produced by Sercel are used for the seismic sensors [3]. It is a passive seismic sensor made composed of a coil attached to the housing and a suspended magnet (Fig.4.16).

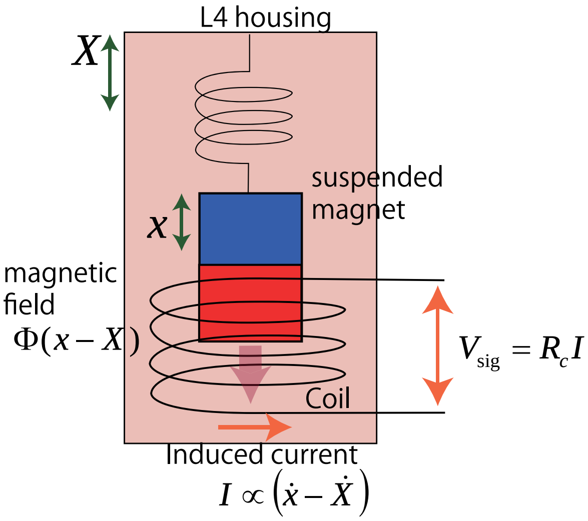

Figure 4.16: The system of the L4 seismometer.

---

[3] See the web page for the details of the product.

By analogy of 4.26, relative motion of the coil and the magnet is written as

$$x - X = \left(\frac{\omega_0^2}{-\omega^2 + i\frac{\omega_0}{Q}\omega + \omega_0^2} - 1 \right) X, \tag{4.49}$$

where X and x are the position of the ground and the magnet, respectively. ω_0 is the resonant frequency of the magnet, and Q is the Q value of the suspension. Since the magnetic field inside the coil is relative to $x - X$, the induced electromotive force relative to $\dot{x} - \dot{X}$ is applied on the coil. The calibration function from the L4 output to the seismic displacement is shown in Fig.4.17. Above the resonant frequency, which is 1 Hz in the case of L4, the output of the seismometer is relative to the velocity of the ground.

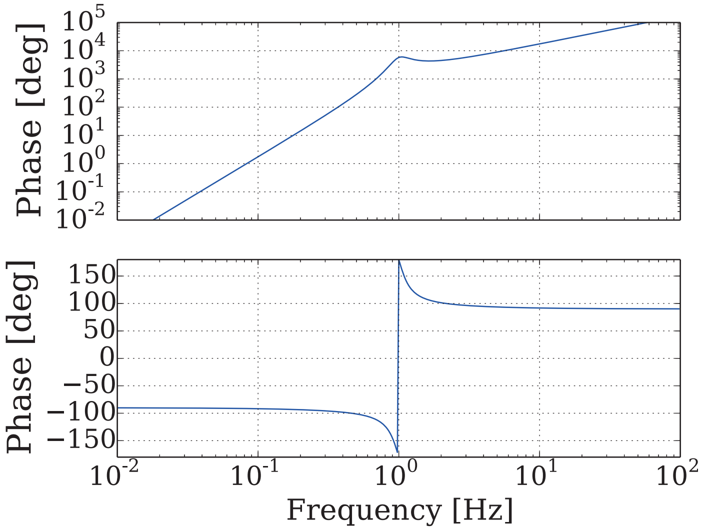

Figure 4.17: The calibration function of L4. Note that the calibration gain includes pre-amplifier

The noise level of L4 is shown in Fig.4.18. This noise is non-correlated signals between the three L4 seismometers set next to each other. Their sensitivity is limited by the amplifier circuit.

Photo Sensors

Since L4 sensors do not have sensitivities at low frequencies, the position of the table would drift if controlled only by L4 since the outputs of the seismometers are the

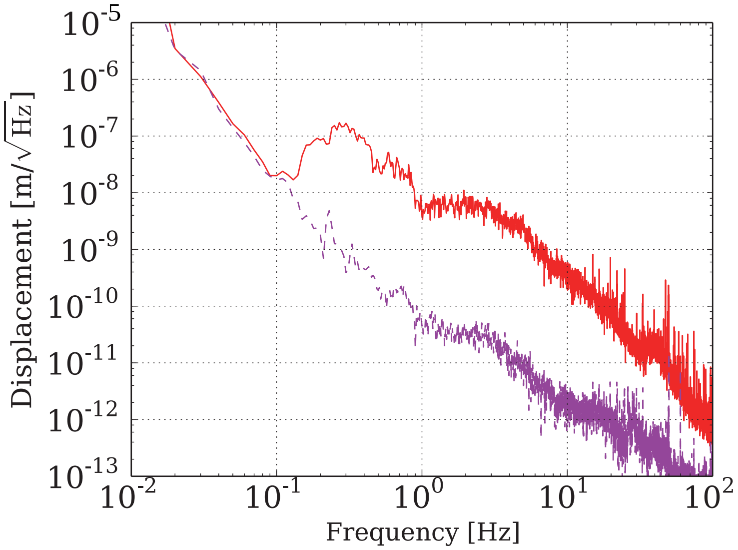

Figure 4.18: The seismic signal and the noise level of the seismometer. The red solid line is the seismic motion of the ground and the purple dashed line is the noise of the seismometer. The noise is calculated as an uncorrelated signal between the three seismometers set next to each other.

circuit noise below 0.1 Hz. Therefore, the table is controlled by the photo sensors at lower frequencies where the seismometers do not have good sensitivity.

The photo sensors used here are the same as described in Sec.4.5.2.

Piezoelectric Elements

We used six piezoelectric elements produced by PI (product number: P.844-30) [4]. The piezoelectric element is a device which convert the voltage to the force. It has a dynamic range of 45 μm with the input voltage of 0 to 100 V. The dynamic range is estimated from the order of the seismic motion. The seismic motion of the ground around 1 Hz is about 10^{-7} m/$\sqrt{\text{Hz}}$, PZTs are chosen so that the seismic motion is canceled out within the dynamic range of the PZTs.

The piezoelectric materials are set inclined by 45 degrees to the gravity force, though they are generally week if the burden perpendicular to the actuating direction is applied. In order to reduce the burden of the material, the piezoelectric elements

---

[4] See the web page for the details of the product.

and the moving parts are connected with a point, not with a surface. Additionally, we have hinges at the both ends of the devices in order to reduce the load on the PZTs caused by the distortion of the legs (See Fig.4.19). Their load limit is 15 kg per one piezoelectric element. Therefore, the total load limit of the AVIT is 90 kg.

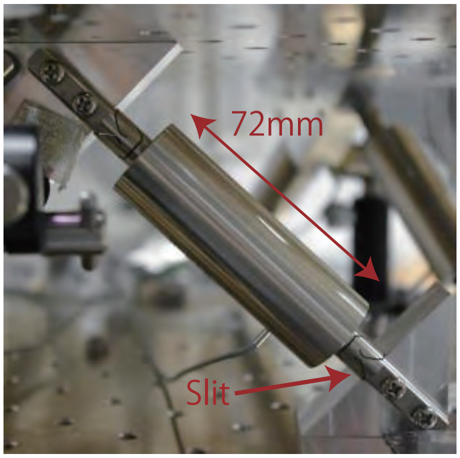

Figure 4.19: A picture of PZT. The length of the PZT is 72 mm, and it has slits at both end for the burden reduction.

4.7 Vacuum System

The setup described above, except the actuators and sensors of the AVIT is installed in a vacuum tank. It prevents the setup from the acoustic noise and loss caused by the residual gas. The chamber is evacuated using a scroll pump and a turbomolecular pump. The achieved degree of vacuum is about 10^{-3} Pa. In order to avoid the vibration of the pump induced, the pumps are connected to the vacuum tank through the damper and long flexible tube.

The vacuum tank is originally the same as the one used in the first prototype. The biggest difference is that the cryogenic system is installed in the chamber for the future application.

4.8 Digital System

All the processes of servo filters, matrices described, and data taking mentioned above are done in a digital system. The digital system is a powerful tool, especially for a system which needs many signals, multi-dimensional matrices, and fine tuning of filtering parameters.

The digital system we used is the same system as one used in LIGO, Virgo, and KAGRA. The systems [67], such as filters, matrices, and their connections, are constructed with *simLink*, the tool in Matlab. This system has tools for basic measurement: oscilloscope, spectrum measurement, open loop transfer function measurement, and so on.

The data is processed with the sampling rate of 4 kHz. The data for the long observation is stored with the sampling rate of 256 Hz.

Also, we have third order low pass filters with the cutoff frequency 10 kHz of Hz for the anti-aliasing/imaging filters before ADC and after DAC.

4.9 Principle Sensitivity

Figure 4.20 is the principle sensitivity in the Phase-II TOBA. We assume that the noise reduction rate by the AVIT as 10 and noise reduction rate with decoupling as 10. Thanks to the seismic isolation systems, the sensitivity above 1 Hz is expected to be improved more than 100 times than the first prototype.

Note that the magnetic coupling noise is not considered here since the test mass and the suspension system is different from the previous detector.

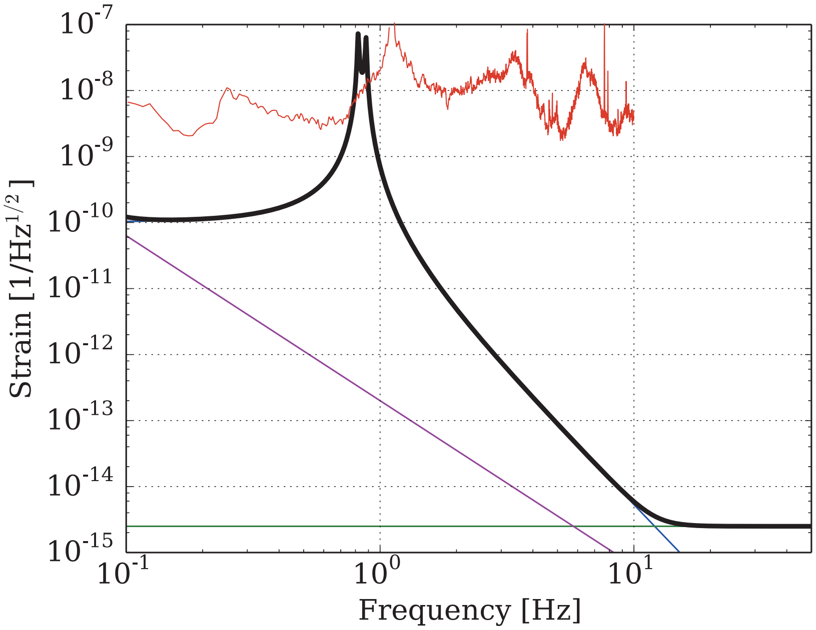

Figure 4.20: The principle sensitivity expected to be obtained with Phase-II TOBA. The bold black line is the total sensitivity. The blue, green, and magenta lines are the seismic noise, shot noise, and the suspension thermal noise. The red line is the sensitivity obtained with the first prototype.

Chapter 5
Experiments

In this chapter, we explain about the characteristics of the Phase-II TOBA. We constructed the Phase-II TOBA according to the design explained in the previous chapter. As a result, the three independent signal are successfully obtained, and the effect of the vibration isolation system is evaluated. We will explain about the calibration, its sensitivity, and its noise source.

5.1 Setup

The Phase-II TOBA is constructed in the room B207, Science Building 1, Department of Physics, University of Tokyo, which is at Hongo campus in Tokyo.

The picture of the vacuum tank with the suspension system installed is Fig.5.1. The two test masses which sense the GWs are suspended from a Hexapod-type active vibration isolation table via an intermediate mass which is magnetically damped by a damping mass. The suspension system except the Hexapod is in a vacuum tank. The vacuum tank has the cryogenic system so that the suspension wires and test masses can be cooled down to 4 K in order to reduce the thermal noise, though the cryogenic system is not use in this thesis.

Also, the test masses and the optical bench without the sensors and actuators are shown in Fig.5.2. Figure 5.3 is a picture of the AVIT integrated in the vacuum tank. The AVIT is set at the top of the vacuum tank in order to suspend the intermediate mass and the damping mass directly. The center of the vibration isolated table, including the suspension points of the masses, is in the vacuum while the sensors and actuators are in the air. The vibration isolation table is connected to the vacuum tank below and fixed table above with bellows. The table has air holes so that both the upper side and underside of the table are in the vacuum. Keeping the air pressure the same above and below the table prevents piezoelectric elements from being broken by the air pressure. Note that we used welded bellows for the connectors which have small spring constants in order to actuate the table without non-linearity.

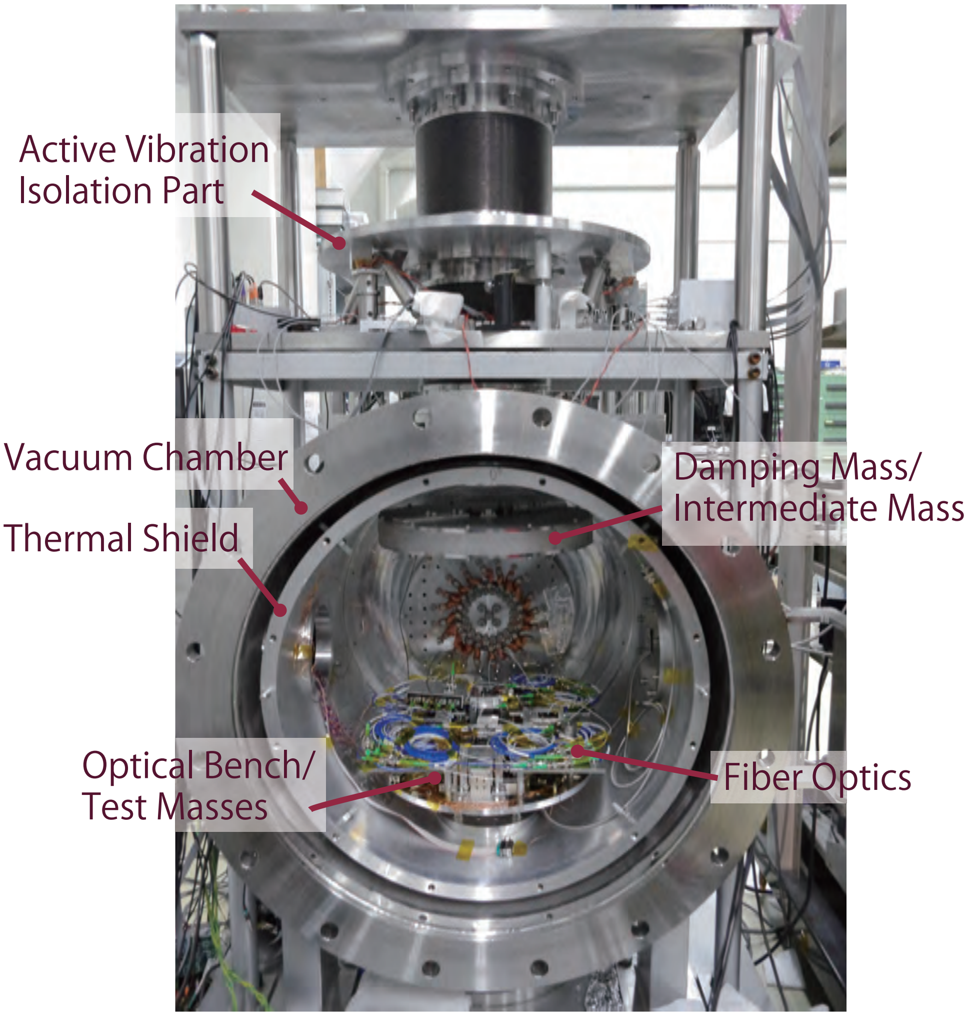

Figure 5.1: A picure of the detector.

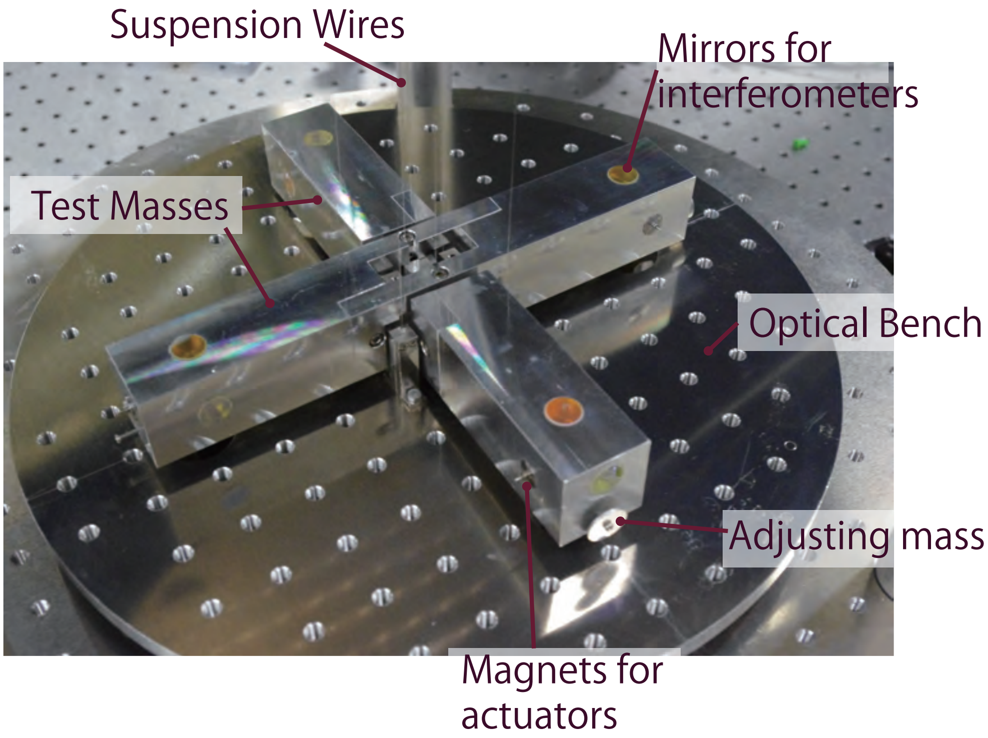

Figure 5.2: A picure of the detector.

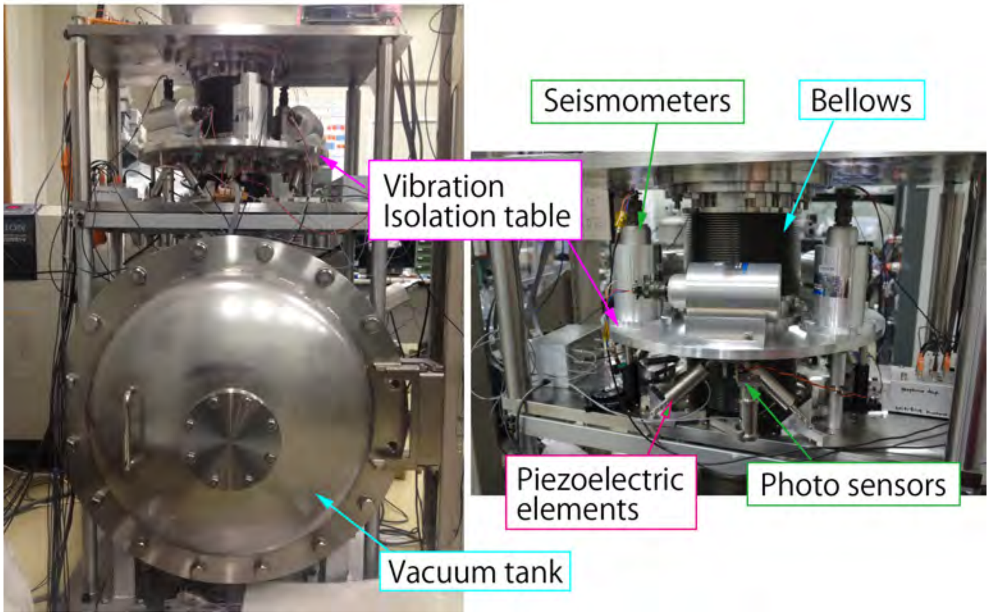

Figure 5.3: Pictures of the AVIT installed in the vacuum tank. The AVIT is set on the stainless table fixed above the vacuum tank. Also the other fixed stainless table is set above the AVIT. The tank and the AVIT table, and the AVIT table and the upper table are connected by bellows, respectively.

5.2 Calibration and Sensitivity

5.2.1 Calibration from the voltage to the angular fluctuation

We calibrate the output signal of the interferometer to the angular displacement using the fringe of the interferometer and the distance between the two mirrors. The calibration factor derived here corresponds to S, S_1, and S_2 in Fig.5.4 and Fig.5.7.

The calibration from the output voltage of the interferometer to the displacement is calculated according to 4.40. $P_{\rm max}$ and $P_{\rm min}$ are measured just before the test masses are locked by the control system using the interferometer. The residual displacement of the test masses is bigger than the wavelength of the laser when the test masses are controlled by PSs whose noise level is bigger than the wavelength of the laser.

The displacement signals are calibrated to the angular fluctuation $\delta\theta$ as

$$\delta\theta = \frac{\delta l_{\rm diff}}{d}, \tag{5.1}$$

where $\delta_{\rm diff}$ is the differential between the displacement of the two mirrors, and d is the distance between the centers of the two mirrors. Note that the calibration error is caused by the uncertainty of d since the beam spot of the laser is not exactly at the center of the mirror. Considering that the diameter of the mirror is 12.7 mm (a half inch) and $d = 190$ mm, the calibration error caused here is estimated as about 7 %.

5.2.2 Calibration from the feedback signal to the out-of-loop signal

The angular fluctuation of the test mass is derived from the error signal or the feedback signal in the servo system. In this subsection, we will explain how to calibrate the feedback signal to the angular fluctuation θ and ϕ.

ROLL Mode Calibration

The angular fluctuation in ROLL mode ϕ is controlled by the servo system shown in Fig.5.4.

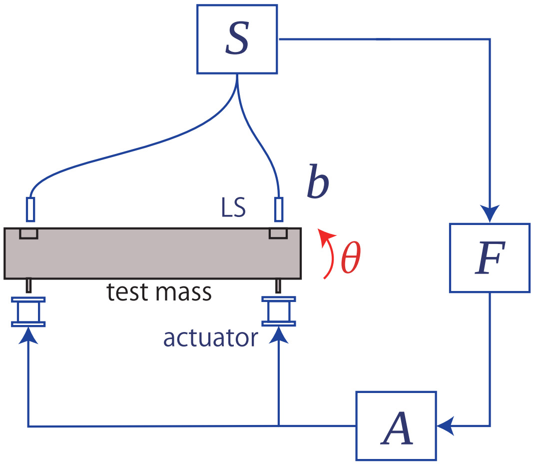

Figure 5.4: The block diagram of the servo system in the vertical plane. Here, we use the single laser interferometer in order to control the ROLL motion.

The displacement disturbance injected to the control loop was suppressed by $1 + G$ times as described in Sec.4.5.1. Therefore, the out-of-loop signal is calibrated as

$$s = (1 + G)s_{\mathrm{err}}. \tag{5.2}$$

The OLTF G is measured by injecting the excitation signal into the control loop. The measured OLTF of ROLL mode is shown in Fig.5.5. The UGF is around 30 Hz and the phase margin is about 30 degree.

The OLTF is not measured with good coherence since the injected excitation signal is largely suppressed at lower frequencies than 1.5 Hz. In order to guarantee the OLTF value $G = SFA$, the transfer functions S, F, and A are measured individually. The transfer function of the laser sensor S is obtained from the fringe of the interferometers as mentioned in the previous subsection. The transfer function of the filter F is obtained from the setup in the digital system. The transfer function of the actuator A is measured PSs. Figure 5.6 is the transfer function of the actuator, i.e., the transfer function from the input of the actuator to the output of the PSs. It is measured without controlling the test masses. The peak around 1 Hz is the coupling from the longitudinal degree of freedom.

The green line in Fig.5.5 is the OLTF calculated using the value of S, F, and A measured individually. It fits well to the data of the overall OLTF measurement. The phase delay of the OLTF at higher frequencies above 40 Hz is considered to be caused by the phase delay of the digital system.

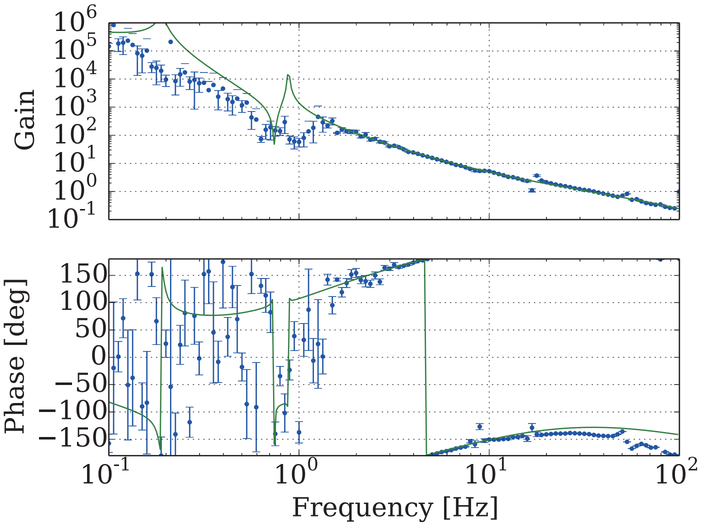

Figure 5.5: The OLTF of the ROLL mode. The blue dots are measured values and the green line is the OLTF calculated using the value of S, F, and A measured individually. The gain of the theoretical OLTF was fitted to the measured values.

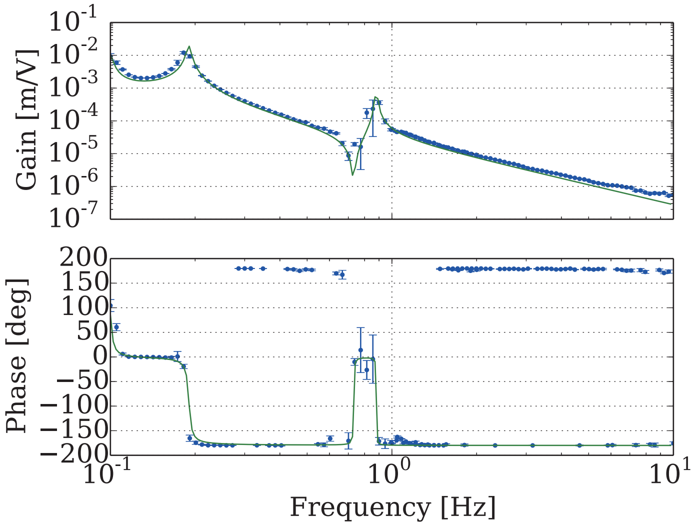

Figure 5.6: The transfer function of the coil-magnet actuator. The blue dots are the measured data and the green line is the fitted line.

YAW Mode Calibration

The angular fluctuation in YAW mode θ and the translational fluctuation in x axis is controlled by the servo system shown in Fig.5.7. Note that the control system is different from that of the ROLL mode since the translational mode and the rotational mode are controlled together by two servo systems. It is necessary to control both the translational mode and the yaw mode at the same time with this sensor configuration since the both interferometers should be locked at their mid fringes.

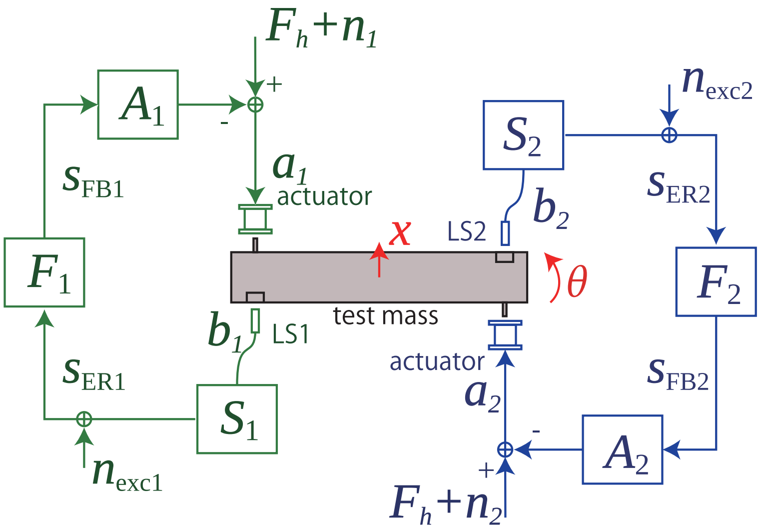

Figure 5.7: The block diagram of the servo system in the horizontal plane. The test mass in the figure is pictured from the top view. The two laser interferometers monitors the displacement b_1 and b_2 and each signal is fed back to the actuators set at the opposite of the each interferometers.

Defining the force applied at the two coil-magnet actuators as a_1 and a_2, respectively, the equations of motion in the translational mode and the rotational mode represented in the frequency domain are

$$m\left(\omega^2 + i\frac{\omega_{\mathrm{T0}}}{Q_{\mathrm{T}}}\omega + \omega_{\mathrm{T0}}^2\right)x = a_1 - a_2, \tag{5.3}$$

$$I\left(\omega^2 + i\frac{\omega_{\mathrm{R0}}}{Q_{\mathrm{R}}}\omega + \omega_{\mathrm{R0}}^2\right)\theta = (a_1 + a_2)\,l, \tag{5.4}$$

where m, I and l are the mass, the moment of inertia of the test mass, and the distance from the center of the test mass to the coil-magnet actuator. x is the translational displacement of the center of the mass, and θ is the angle of the bar around the center of the mass. ω_{T0} and ω_{R0} are the resonant angular frequencies of the test mass in the translational mode and the rotational mode, respectively. Q_{T} and Q_{R} are the Q-value in the translational mode and the rotational mode.

Here, b_1 and b_2 are the displacement of the mirrors set on the test mass written as

$$\begin{aligned} b_1 &= -x + l\theta, && (5.5) \\ b_2 &= x + l\theta. && (5.6) \end{aligned}$$

Substituting 5.3 and 5.4 into 5.5 and 5.6, we get

$$\begin{aligned} b_1 &= -T(a_1 - a_2) + R(a_1 + a_2) && (5.7) \\ &= (-T + R)a_1 + (T + R)a_2, && (5.8) \\ b_2 &= T(a_1 - a_2) + R(a_1 + a_2) && (5.9) \\ &= (T + R)a_1 + (-T + R)a_2, && (5.10) \end{aligned}$$

where

$$\begin{aligned} T &= \frac{1}{m\left(\omega^2 + i\frac{\omega_{\mathrm{T0}}}{Q_{\mathrm{T}}}\omega + \omega_{\mathrm{T0}}^2\right)}, && (5.11) \\ R &= \frac{l^2}{I\left(\omega^2 + i\frac{\omega_{\mathrm{R0}}}{Q_{\mathrm{R}}}\omega + \omega_{\mathrm{R0}}^2\right)}. && (5.12) \end{aligned}$$

Considering the control loop where the displacement disturbance from GWs h are injected, the relation between a_1, a_2, b_1, and b_2 are

$$\begin{aligned} \begin{pmatrix} b_1 \\ b_2 \end{pmatrix} &= -\begin{pmatrix} -T+R & T+R \\ T+R & -T+R \end{pmatrix} \begin{pmatrix} a_1 \\ a_2 \end{pmatrix} + \begin{pmatrix} h \\ h \end{pmatrix} && (5.13) \\ &= -\begin{pmatrix} -T+R & T+R \\ T+R & -T+R \end{pmatrix} \begin{pmatrix} B_1 & 0 \\ 0 & B_2 \end{pmatrix} \begin{pmatrix} b_1 \\ b_2 \end{pmatrix} + \begin{pmatrix} h \\ h \end{pmatrix}, && (5.14) \end{aligned}$$

where $B_i = S_i F_i A_i$ for $i = 1, 2$. Therefore, the force applied on the test mass including noise is written as

$$\begin{pmatrix} h \\ h \end{pmatrix} = \left[I + \begin{pmatrix} -T+R & T+R \\ T+R & -T+R \end{pmatrix} \begin{pmatrix} B_1 & 0 \\ 0 & B_2 \end{pmatrix} \right] \begin{pmatrix} b_1 \\ b_2 \end{pmatrix}, \tag{5.15}$$

where I is the identity matrix. The signal s'_1 is derived by adding the two signals:

$$s'_1 = 2h = (1 + 2RB_1)b_1 + (1 + 2RB_2)b_2. \tag{5.16}$$

The transfer function B_1 and B_2 are measured using the excitation signals n_{exc1} and n_{exc2}. The measured function is

$$\tilde{G}_i = \frac{S_i b_i}{S_i b_i + n_{\mathrm{exc}i}}, \tag{5.17}$$

where $i = 1, 2$. Here, we define the vectors and matrix as follows:

$$\vec{b} = \begin{pmatrix} b_1 \\ b_2 \end{pmatrix} \tag{5.18}$$

$$\vec{n}_{\mathrm{exc}} = \begin{pmatrix} n_{\mathrm{exc1}}/S_1 \\ n_{\mathrm{exc2}}/S_2 \end{pmatrix} \tag{5.19}$$

$$G = \begin{pmatrix} -T+R & T+R \\ T+R & -T+R \end{pmatrix} \begin{pmatrix} B_1 & 0 \\ 0 & B_2 \end{pmatrix}. \tag{5.20}$$

Assuming $h \ll n_{\mathrm{exc1}}, n_{\mathrm{exc2}}$, $\vec{b} + \vec{n}_{\mathrm{exc}}$ is derived as

$$\vec{b} = G\left(\vec{b} + \vec{n}_{\mathrm{exc}}\right) \tag{5.21}$$

$$\therefore \vec{b} = (I - G)^{-1} G \vec{n}_{\mathrm{exc}} \tag{5.22}$$

$$\therefore \vec{b} + \vec{n}_{\mathrm{exc}} = (I - G)^{-1} \vec{n}_{\mathrm{exc}}. \tag{5.23}$$

Substituting 5.20 to 5.22 and 5.23,

$$\vec{b} = X \begin{pmatrix} B_1(-T+R) + 4B_1B_2TR & B_2(T+R) \\ B_1(T+R) & B_2(-T+R) + 4B_2B_2TR \end{pmatrix} \vec{n}_{\mathrm{exc}}, \tag{5.24}$$

$$\vec{b} + \vec{n}_{\mathrm{exc}} = X \begin{pmatrix} 1 - B_2(-T+R) & B_2(T+R) \\ B_1(-T+R) & 1 - B_1(-T+R) \end{pmatrix} \vec{n}_{\mathrm{exc}}, \tag{5.25}$$

where

$$X = \frac{1}{1 - B_1(-T+R) - B_2(-T+R) - 4B_1B_2TR}. \tag{5.26}$$

Since excitation signal is injected one by one, $n_{\mathrm{exc2}} = 0$ when $n_{\mathrm{exc1}} \neq 0$ and $n_{\mathrm{exc1}} = 0$

when $n_{\text{exc2}} \neq 0$ Therefore, the measured OLTF $\tilde{G}_i$ is

$$\begin{aligned}
\tilde{G}_1 &= \frac{B_1(-T+R) + 4B_1B_2TR}{1 - B_2(-T+R)} && (5.27)\\
&= G_1 + \left(\frac{T-R}{T+R}\right)^2 \frac{G_2}{1-G_2} G_1, && (5.28)\\
\tilde{G}_2 &= \frac{B_2(-T+R) + 4B_1B_2TR}{1 - B_1(-T+R)} && (5.29)\\
&= G_2 + \left(\frac{T-R}{T+R}\right)^2 \frac{G_1}{1-G_1} G_2, && (5.30)
\end{aligned}$$

where $G_1 = B_1(-T+R)$ and $G_2 = B_2(-T+R)$.

The measured transfer function $\tilde{G}_1$ and $\tilde{G}_2$ are in Fig.5.8 and 5.9.

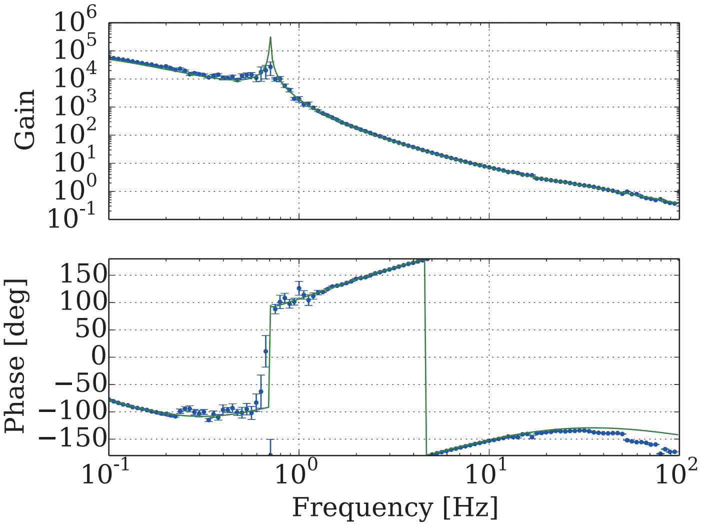

Figure 5.8: The transfer function $\tilde{G}_1$. The blue dots are the measured data and the green line is the fitted line.

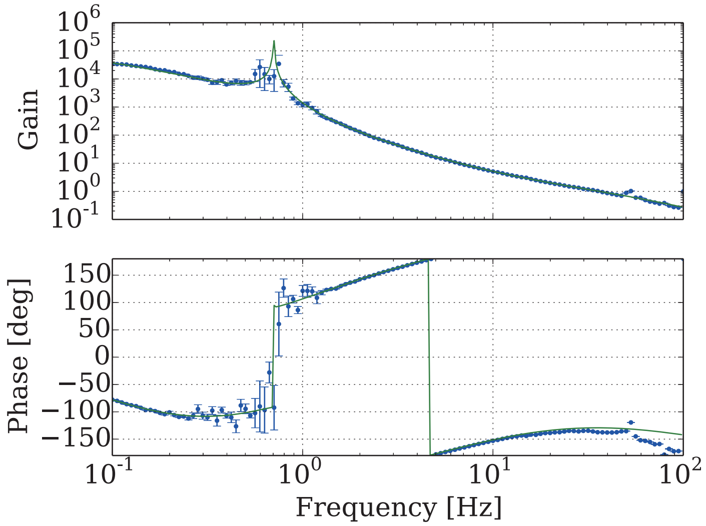

Figure 5.9: The transfer function $\tilde{G}_2$. The blue dots are the measured data and the green line is the fitted line.

5.2.3 Calibration to GW amplitude

According to 3.12 and 3.13, the three GW signals are derived from the out-of-loop angular fluctuations as

$$s_1 = \frac{1}{H_{\times 1}} \frac{1}{2}(\theta_1 - \theta_2) \tag{5.31}$$

$$s_2 = \frac{1}{H_{\times 2}} \phi_1 \tag{5.32}$$

$$s_3 = \frac{1}{H_{\times 3}} \phi_2 \tag{5.33}$$

(5.34)

where $H_{\times i}(i = 1, 2, 3)$ are defined as

$$H_{\times i} = H_{\times i}^{\mathrm{TM}} - H_{\times i}^{\mathrm{OB}}. \tag{5.35}$$

Here, $H_{\times i}^{\mathrm{TM}}$ and $H_{\times i}^{\mathrm{OB}}$ are the transfer functions from the GW signals to the angular fluctuations of the test masses and the optical bench, respectively. H_{+i} are considered to be zeros since $q_+ = 0$. Note the optical bench is also sensitive to GWs since it is suspended in our setup.

ROLL Mode Calibration

Assuming the test mass as a rectangular solid, the transfer function of the test mass $H^{\mathrm{TM}}_{\times 2,3}$ is derived as

$$H^{\mathrm{TM}}_{\times 1} \sim \frac{q^{\mathrm{TM}}_{\times 1}}{2I^{\mathrm{TM}}_{1}} \sim 0.48, \tag{5.36}$$

above the resonant frequencies of the test masses in our setup.

Note that the transfer functions of the optical bench $H^{\mathrm{OB}}_{\times 2,3}$ are not zero in our case since the optical bench has also the rectangular shape from the side view. Calculating $q^{\mathrm{OB}}_{\times i}$ and I^{TM}_{i} around the horizontal axis for $i = 1, 2$, we obtain

$$\frac{q^{\mathrm{OB}}_{\times i}}{2I^{\mathrm{OB}}_{i}} \sim 0.44. \tag{5.37}$$

This is calculated from the design value. The fiber optics and photo detector set on the optical bench are not included in this calculation. Therefore, H_i used to calibrate s_2 and s_3 is calculated as shown in Fig.5.10. The peak at 0.15 Hz is the resonant frequency of the test mass, and the peak at 1.1 Hz is the resonant frequency of the optical bench.

YAW Mode Calibration

The transfer function of the test mass is the same as that of ROLL mode $H^{\mathrm{TM}}_{\times 1,2}$. In the case of YAW, the transfer function of the optical bench is considered to be zero since the optical bench has the circular shape from the top or bottom view.

The transfer function $H_{\times 1}$ is shown in Fig.5.11. The peak at 0.1 Hz is the resonant frequency of the test mass. The absolute value of $H_{\times 1}$ is about 0.5 above the resonant frequency.

5.2.4 Sensitivity

The obtained typical sensitivity of this detector is shown in Fig.5.12. The sensitivity of s_1 is improved by about 100 times at the maximum compared to the first prototype at the higher frequencies where the seismic coupling noise limits the sensitivity in the first prototype. Al lower frequencies than 1 Hz, the sensitivity is not improved since the resonant frequencies of the test mass are higher than before. The sensitivity of s_2 and s_3 is worse by about 1,000 times than s_1, because of the seismic noise as described in Sec.5.3 and the calibration factor about 10 times different from that of s_1.

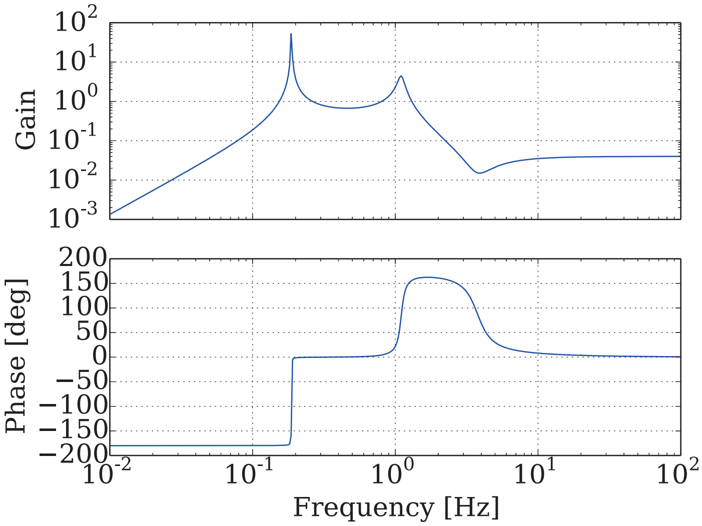

Figure 5.10: The calibration factor from the rotational angle to the amplitude of GWs in s_2. The resonant frequency of the test mass is set to be 0.15 Hz, and that of the optical bench is 1.1 Hz. The quality factor is assumed to be 10.

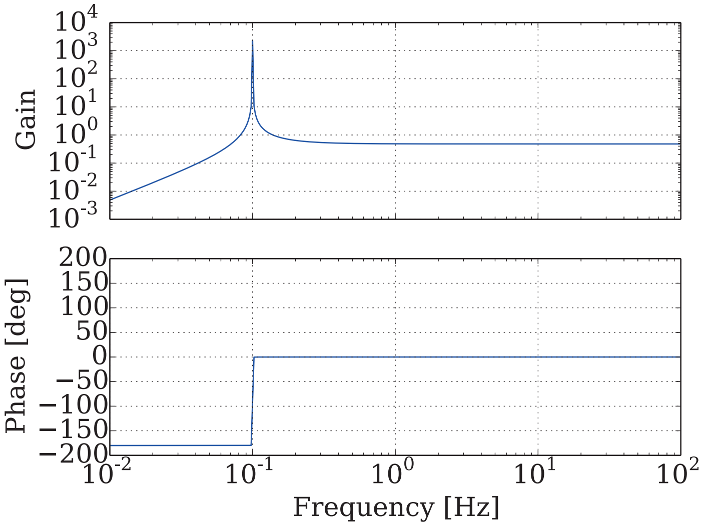

Figure 5.11: The calibration factor from the rotational angle to the amplitude of GWs in s_1.

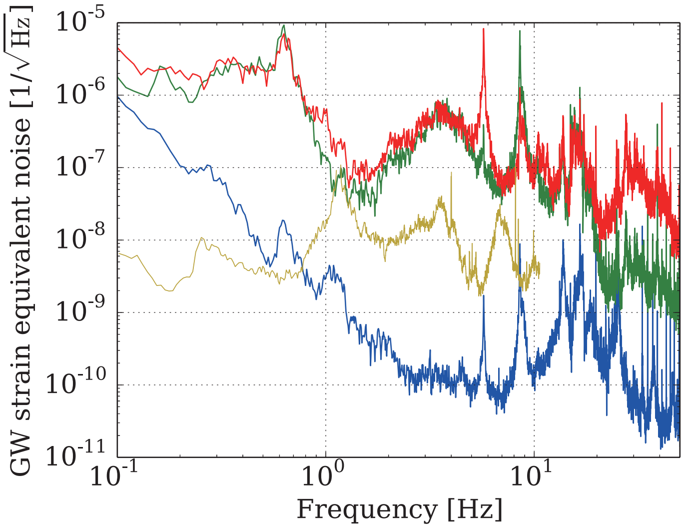

Figure 5.12: The GW strain equivalent noise spectra. The blue, green, and red lines are the sensitivity of s_1, s_2, and s_3, respectively. The yellow line is the sensitivity obtained from the first prototype of the TOBA.

In the following sections, their noise source and other characteristics will be evaluated.

5.3 Seismic Noise

5.3.1 Passive Vibration Isolation

Since the test masses and the optical bench are suspended, the seismic noise is reduced by the passive vibration isolation. The passive vibration isolation rate, i.e., the transfer function from the top table to the signals are measured by shaking the top table of the AVIT.

LONG to YAW coupling

Fig.5.13 is the transfer function from the displacement of the suspension point to the signals of the interferometers LS1 and LS2 when the suspension point is shaken to the LONG direction by the AVIT. The black line is the theory of the transfer function described in Sec 4.4.2. In this plot, we assume that the coupling rate of

0.1. It shows that the transfer functions to the LS1 and the LS2 signals are close to the theory, though the peak was largely damped. The cause is under investigation while it is considered to be because of the control loop.

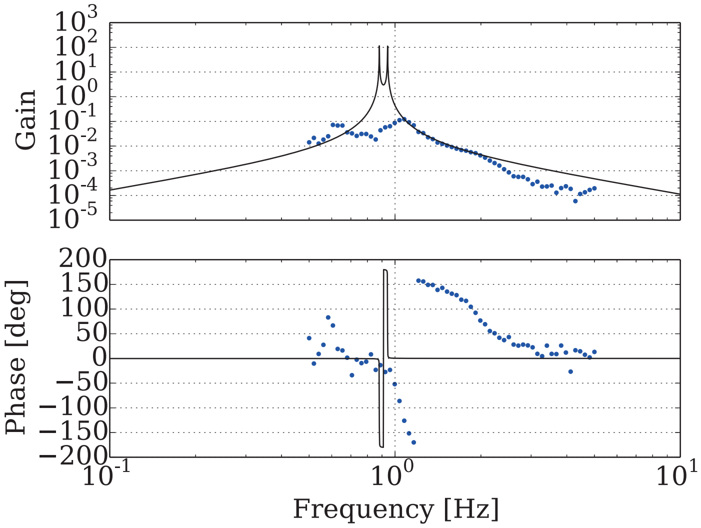

Figure 5.13: Transfer function from the displacement at the top table to longitudinal motion of the test mass. The blue dots represent the transfer function to the horizontal rotational signal. The black lines are the theoretical line with the assumption of the decoupling rate of 10.

YAW to YAW transfer function

Fig.5.14 is the transfer function from the horizontal rotation of the top table to the horizontal rotation of the test mass. The green line is the theory of the transfer function from rotational motion of the suspension point to the rotational motion of the test mass. The red line is the transfer function from the translational motion to the rotational motion. The cyan line is the sum of the two transfer functions.

The transfer function from the translational motion to the rotational motion should be considered since the motion of the AVIT is not perfectly decoupled. Even though the output matrix of the AVIT is adjusted, the translational motion would be excited when the rotational motion is excited because of the small asymmetry of the AVIT.

Other than the peaks, the gain of the transfer function at low frequencies also does not fit to the theory. Though it is under investigation, it shows that the sensitivity is not affected by the rotational motion of the suspension point.

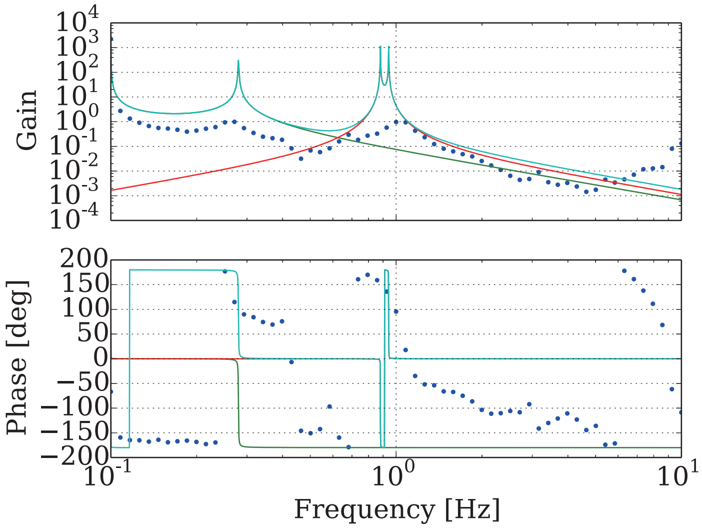

Figure 5.14: Transfer function from the rotation at the top table to the rotation of the test mass.

SIDE to ROLL transfer function

Assume that the coordinates of the suspension point and the test mass are $X(t)$ and $x(t)$, respectively (Fig.5.15), the equation of motion of the rotational angle $\theta(t)$ is

$$I\ddot{\theta}(t) + \gamma\dot{\theta}(t) = mgd(\phi + \theta), \tag{5.38}$$

where $\phi = (X(t) - x(t))/l$. I, m, g, d, and l are the moment of the inertia of the test mass, the mass of the test mass, the gravity acceleration, the distance between the suspension point and the center of the mass of the test mass, and length of the suspension wire, respectively. Performing Fourier transformation and substituting 4.26, we obtain

$$\tilde{\theta}(\omega) = \frac{\omega_{\theta 0}}{-\omega^2 + i\frac{\omega_{\theta 0}}{Q}\omega + \omega_{\theta 0^2}} \left(1 - \frac{\omega_{\mathrm{TM0}}}{-\omega^2 + i\frac{\omega_{\mathrm{TM0}}}{Q}\omega + \omega_{\mathrm{TM0}}^2}\right) \frac{\tilde{X}}{l}, \tag{5.39}$$

where $\omega_{\theta 0} = mgd/I$. The same equation is applied to the optical bench. The observed transfer function is the difference between the rotational angle of the test mass and that of the optical bench.

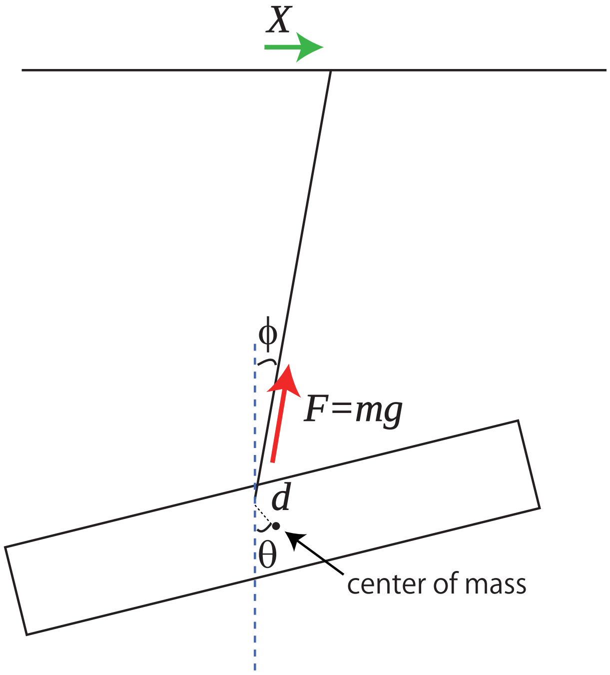

Figure 5.15: A schematic view of the test mass excited by translational displacement.

The black line in Fig.5.16 shows the transfer function calculated as above. We assume that the resonant frequency of the $\phi(s_2)$ of the test mass as 0.15 Hz, one of the ϕ of the optical bench as 1.1 Hz, which is calculated in case that the optical bench do not have any optics and the center of the mass is at the suspension points. The peak appeared at about 0.7 Hz is generated by the pendulum mode from the pendulum mode including the intermediate mass. The resonant frequency of the pendulum mode only below the intermediate mass is about 1 Hz. Note that Q values are assumed to be 30 for the optical bench.

5.3.2 Seismic noise level

From the measurement above, how largely the seismic noise contributes to the sensitivity is calculated. Figure 5.17, 5.17, and 5.17 show the sensitivity and the seismic

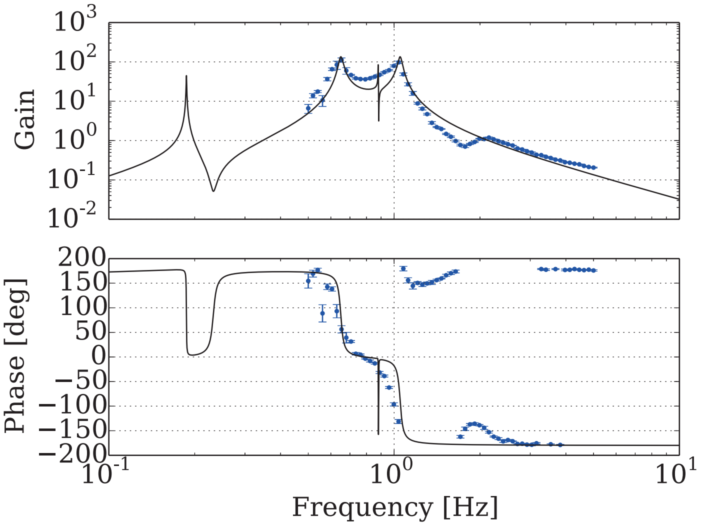

Figure 5.16: The transfer function from the translational displacement at the top table to the signals of the rotational mode. The blue points represent the transfer function to the two outputs of the interferometers, LS4, from which the ROLL signal is derived. (See Fig.4.12.)

noise contribution. They show that the seismic noise limits the sensitivities around 1 - 10 Hz.

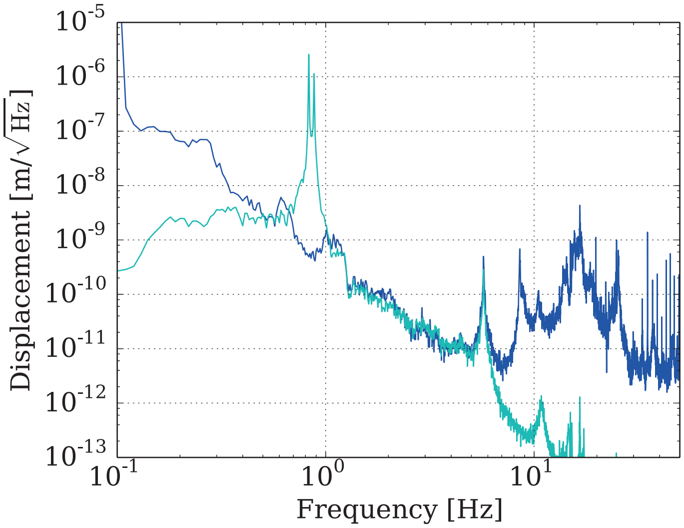

Figure 5.17: The affect of the seismic noise on the sensitivity. The blue line is the angular displacement of the YAW mode and the cyan line is the contribution of the seismic noise.

5.4 Decoupling

When the signals are calibrated from the signal to GW-equivalent noise spectrum, the signals of four interferometers are diagonalized to four degrees of freedom. Though the rotational angle $\theta = s_{\mathrm{LS1}} - s_{\mathrm{LS2}}$ in principle, the efficiency of the two sensors are slightly different. Here, s_{LS1} and s_{LS2} represent the signals from LS1 and LS2, which are converted to the rotational angle. The difference between the two efficiency is, for example, caused by the difference of the distance between the center of the mass and the point on which the laser beam hit. Therefore, we adjusted the coefficient of the decoupling according to the height of the peaks appeared because of the translational motion as shown in the previous section. Figure 5.20 shows the efficiency of the decoupling. The blue line is the GW strain equivalent noise to which the raw signal from LS1 is calibrated. The green line is the signal of $s_{\mathrm{LS1}} - s_{\mathrm{LS2}}$, i.e., the signal decoupled with non-adjusted coefficients. The GW signals are not

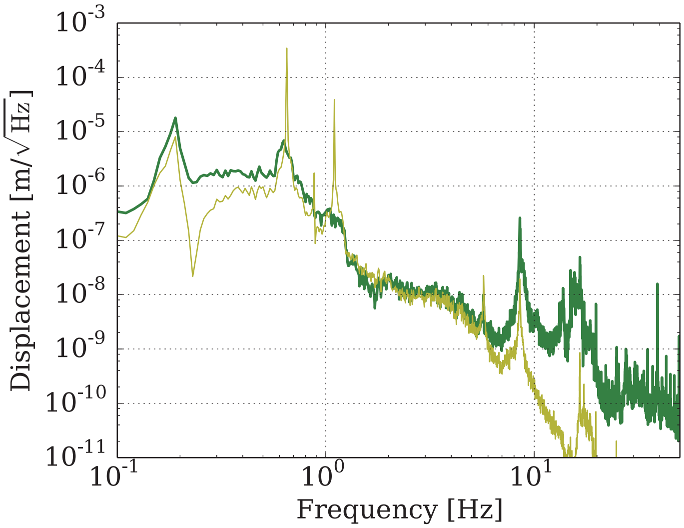

Figure 5.18: The affect of the seismic noise on the sensitivity. The green line is the angular displacement of the ROLL mode, which corresponds to s_2, and the yellow line is the contribution of the seismic noise.

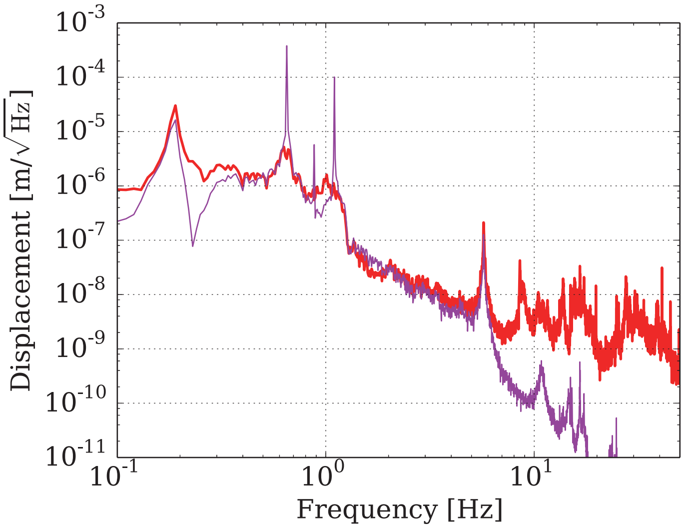

Figure 5.19: The affect of the seismic noise on the sensitivity. The red line is the angular displacement of the ROLL mode, which corresponds to s_3, and the magenta line is the contribution of the seismic noise.

cancelled by the decoupling since the signals used for the decoupling is confirmed to be the translational motion from the seismic noise measurement mentioned above. The red line is the signal of rotational motion decoupled with adjusted coefficients. They show the coefficient adjustment improves the sensitivity about 5 times at the maximum.

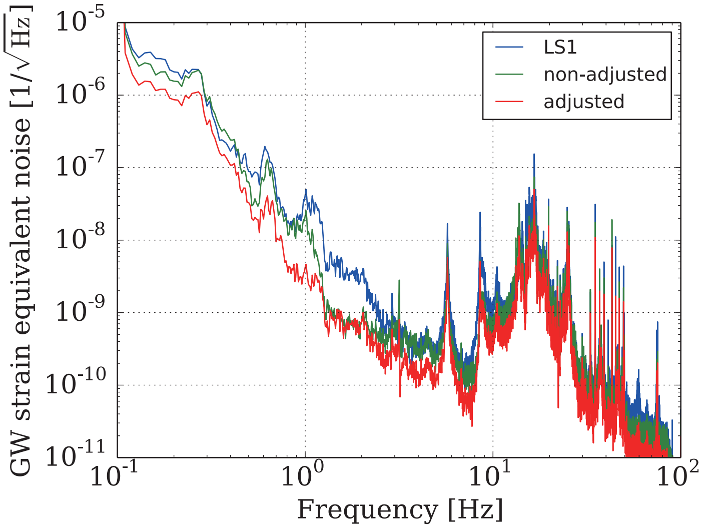

Figure 5.20: The GW equivalent noise spectra of s_{LS1}, $s_{\mathrm{LS1}} + s_{\mathrm{LS2}}$, and $cs_{\mathrm{LS1}} + c'\mathrm{LS2}$. c and c' are the adjusted coefficients. It shows he careful decoupling improves the sensitivity.

5.5 Common Mode Noise Reduction

In our setup, the motion of the two test masses are measured. The signal s_1 is derived from the differential rotation of the two test masses. It reject the rotational noise which affect on the test masses commonly. Figure 5.21 shows the effect of the common mode noise rejection. The blue line and the green line are the sensitivity derived from the rotational fluctuation of the single test mass. The red line is the differential rotation of the two test masses. It shows the noise at low frequencies, mainly below 1 Hz are reduced by about 5 times at maximum.

From these observations, it is shown that the sensitivities of s_2 and s_3 are limited by the seismic noise at almost all the frequencies. Also, the sensitivity of s_1 below

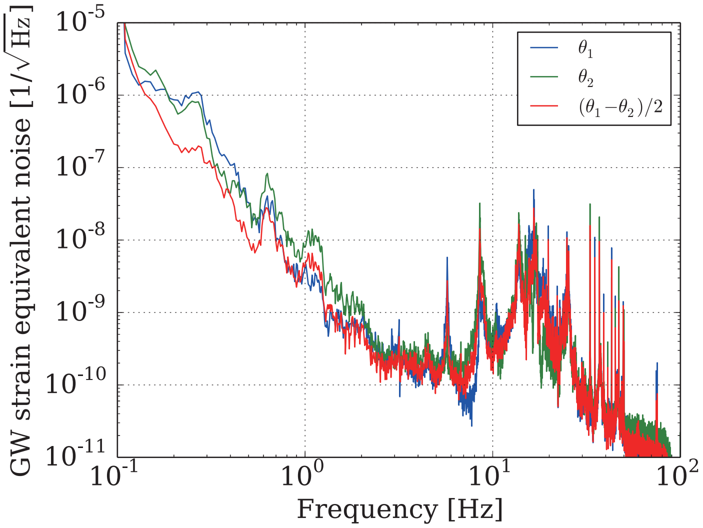

Figure 5.21: The GW equivalent noise spectra of θ_1, θ_2, and $(\theta_1-\theta_2)/2$. The common mode rejection between the two angles are effective at lower frequencies.

about 2 Hz is limited by the seismic noise even though its effect is reduced by the decoupling and common mode rejection.

5.6 ADC/DAC Noise

ADC and DAC has the quantization noise since the analog signals are converted to discrete signals and vise versa. The noise level of ADC and DAC is shown in Fig 5.22.

5.7 Sensor Noise

5.7.1 Shot Noise

The shot noise is one of the fundamental noise for laser interferometers which is caused by the Heisenberg's uncertainty principle. A photo detector counts the number of photons. Here, the quantum mechanics yields the fluctuation of the number of the photons. Since the number of photons has Poisson distribution, the current has uncertainty called the shot noise.

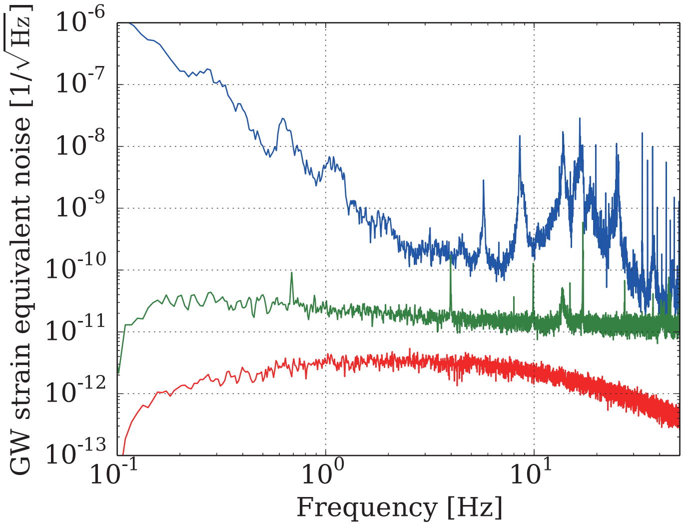

Figure 5.22: The noise spectrum of the ADC and the DAC. The blue line is the sensitivity of s_1. The green line is the contribution from the ADC, and the red line is from the DAC.

When an averaged current i_{DC} is emitted from the photo detector, the spectrum of the shot noise current is written as

$$i_{\mathrm{shot}} = \sqrt{2ei_{\mathrm{DC}}}, \tag{5.40}$$

where e is the elementary charge. The DC photo current produced by the laser with power of P is

$$i = \frac{e\eta}{\hbar\Omega}P, \tag{5.41}$$

where η and $\hbar$ are the quantum efficiency of the photo diode and the reduced Planck constant, respectively. The noise in the optical pass length caused by the shot noise is

$$\delta l_{\mathrm{shot}} = \frac{\lambda}{4\pi}\frac{2}{P_{\mathrm{max}} - P_{\mathrm{min}}}P_{\mathrm{shot}}. \tag{5.42}$$

Assuming $P_{\mathrm{min}} = 0$ for the convenience, equivalent optical pass noise is obtained as

$$\delta l_{\mathrm{shot}} = \sqrt{\frac{\hbar c\lambda}{4\pi P}}, \tag{5.43}$$

where $P = P_{\mathrm{max}}/2$.

5.7.2 Radiation Pressure Noise

Radiation pressure noise arises from the Heisenberg's uncertainty principle as well as the shot noise. When photons are reflected by a mirror, back reaction force is applied to the mirror. The back reaction force also fluctuates since the number of photons hitting on the mirror also fluctuates.

The applied force is written as

$$\delta F_{\rm rad} = \sqrt{\frac{2\pi\hbar P}{c\lambda}}. \tag{5.44}$$

Therefore, the angle fluctuation according to the quantum back action is

$$\delta\theta = \frac{1}{\omega^2 I}\sqrt{\frac{2\pi\hbar P}{c\lambda}}, \tag{5.45}$$

where I is the moment of inertia of the test mass bar.

The shot noise and radiation pressure noise in the GW strain equivalent noise is shown in 5.23.

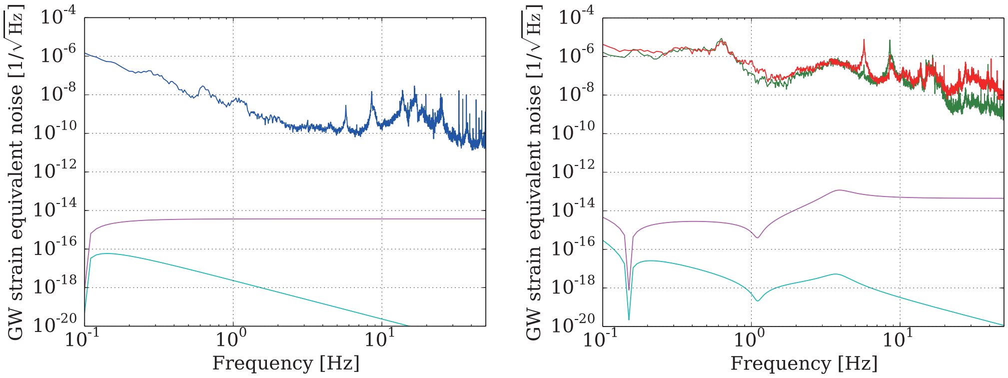

Figure 5.23: The shot noise and the radiation pressure noise. The blue, green, and red lines are the sensitivity of the signals s_1, s_2, and s_3, respectively. The magenta and the cyan lines are the shot noise and the radiation pressure noise. The shot noise and the radiation pressure noise in s_1 are different from those in s_2 and s_3 since the calibration factors are different. Note that the calibration factors of s_2 and s_3 are assumed to be the same, though they are slightly different because of the different resonant frequencies.

5.7.3 Intensity Noise

The amplitude of the laser is not perfectly stable. The intensity noise of our laser source is shown in Fig.5.24. It is measured with the laser beam just before injected to a beam splitter, just after the initial beam is split into 8 beams for the 8 interferometers on the optical bench.

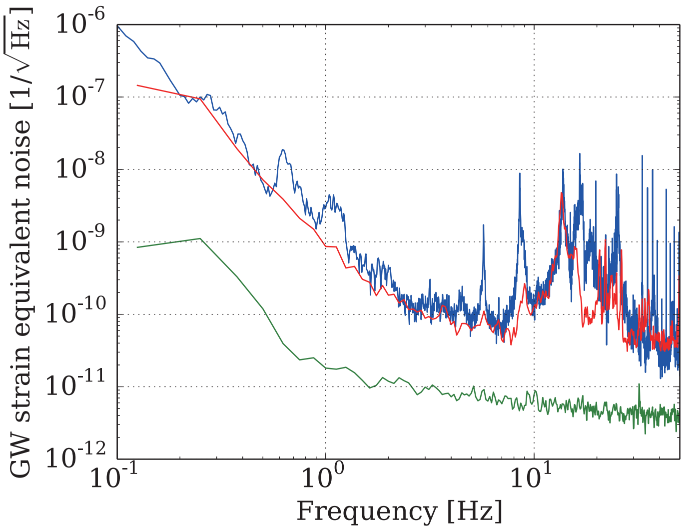

Figure 5.24: The noise caused by the intensity noise and the phase noise from the laser interferometers. The blue line is the sensitivity in s_1. The green, and the red lines are the noise from the intensity fluctuation of the laser, and the phase noise injected from the interferometers, respectively.

5.7.4 Phase Noise

The total noise caused by the fiber interferometer is also shown in Fig.5.24. You can see that the sensitivity is limited by the phase noise of the interferometers or close to the phase noise at all frequencies, while some peaks appeared in the spectrum of s_1 is caused by the seismic noise.

It is the spectrum of the output of the interferometers when the test masses are fixed. It includes the shot noise, the dark current noise, the intensity noise, and the phase noise induced from the fiber interferometers. Since the noise level is larger than the other noise described above, the sensitivity of the interferometers is limited by the phase noise caused by the fiber interferometer part.

Our noise level of the phase noise above 1 Hz is almost the same as the sensitivity of the interferometers with fixed mirrors not on the optical bench but on the optical table. [63, 64]. It means that the cause of the noise of our interferometers is not the structure of the optical bench, but the configuration of the fiber interferometers.

5.8 Performance of the AVIT

5.8.1 Open Loop Transfer Function

The open loop transfer function of the AVIT control in the translation direction is shown in Fig.5.25.

It shows out vibration isolation region is about 0.5 Hz to 7 Hz. The vibration isolation rate is limited by the dynamic range of the piezoelectric elements at low frequencies. The seismic displacements has a bump around 0.5 Hz called the micro seismic noise, which is mainly caused by ocean waves beating the shore. The micro seismic noise is too large to compensate the displacement with the piezoelectric devices we used. At higher frequencies, the vibration isolation rate is limited by the peaks at 7 and 9 Hz. These peaks are resonance of the structure of the poles supporting the AVIT which is set around the vacuum tank. Since these poles are originally made for the support of the superconductor in the first prototype, they are not thick enough.

The blue dots do not fit to the theoretical values at lower frequencies in x and y directions. It is because of the tilt coupling of the seismometers. Since the relative position of the coil and the suspended magnets in the seismometers also changes according to the tilt of the seismometers, the careful adjustment of the output matrix is necessary in order not to rotate the top table when the table is actuated in translational direction. Even though the careful adjustment, the tile couplings still remain.

5.8.2 Vibration Isolation Performance

The vibration isolated seismic displacement by the AVIT controlled by the open loop transfer function as shown above is Fig.5.26. The blue, red, and green lines are the seismic displacement in x, y, and z directions. The dashed lines represent the seismic displacement when the AVIT is not controlled, while the solid lines represents the

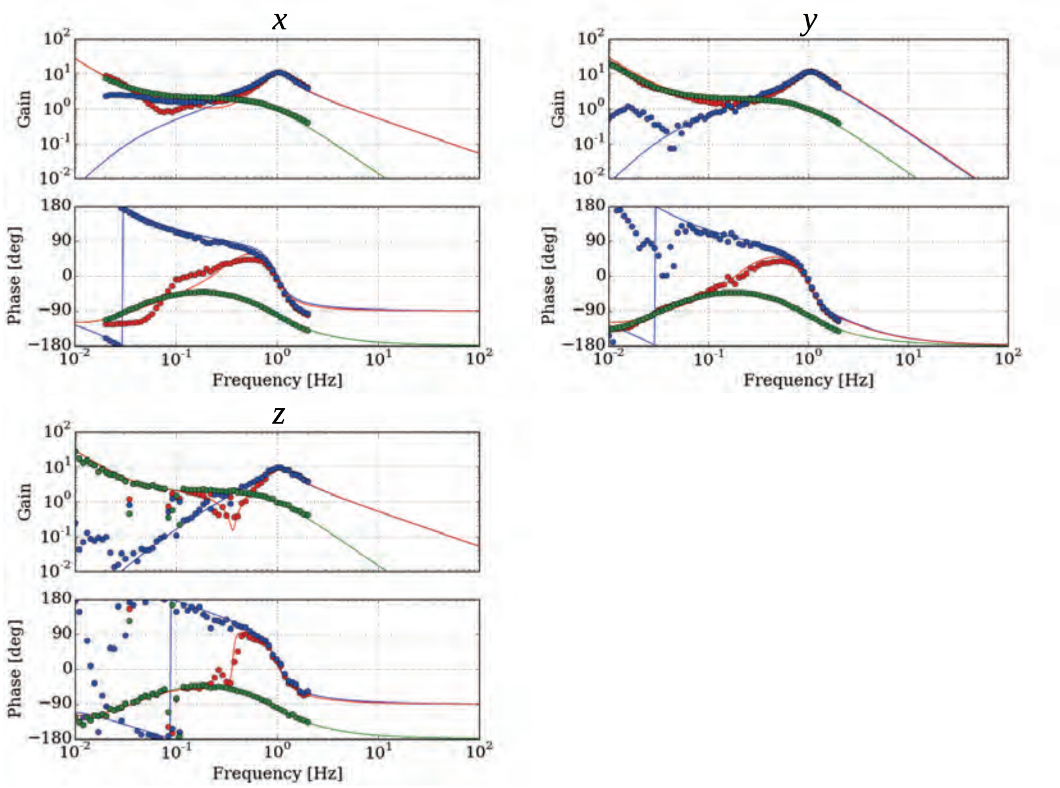

Figure 5.25: The open loop transfer functions of the AVIT in x, y, and z directions. The red line and dots are the total open loop transfer function of the control system (G in 4.42 and 4.43). The blue and the green lines and dots are the open loop transfer function of the seismometers (G_s) and the photo sensors (G_p), respectively. The dots are measured data, while the lines are theoretical values.

seismic displacement when the AVIT is active. It shows that the seismic vibration is isolated about 10 times at 1 Hz.

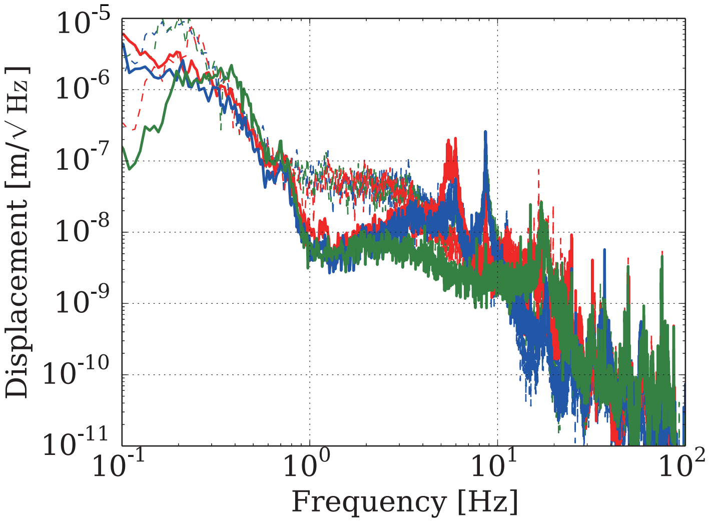

Figure 5.26: The seismic noise with the AVIT off and on. The dashed lines represent the seismic displacement with AVIT off, and the solid lines represent one with the AVIT on.

Also, the spectrogram of the seismic displacement during the AVIT on is shown in Fig.5.27. It shows that the AVIT is able to stably isolate the vibration in all the translational directions at the same time for more than two days. Note that it is measured without the suspension systems.

5.8.3 Sensitivity Improvement

In order to see the impact of the AVIT, we compared the sensitivity of Phase-II TOBA with the AVIT on and off. In Fig.5.28, the solid lines are the sensitivity with the AVIT on, while the dashed lines are the sensitivity with the AVIT off. The blue, green and red lines represent the sensitivity of s_1, s_2, and s_3 with AVIT on, respectively. The sky-blue, right green, and pink dashed lines are the sensitivity of s_1, s_2, and s_3 with AVIT off. The sensitivity around 1 Hz is improved in the every signals according to the vibration isolation rate obtained by the AVIT. However, the

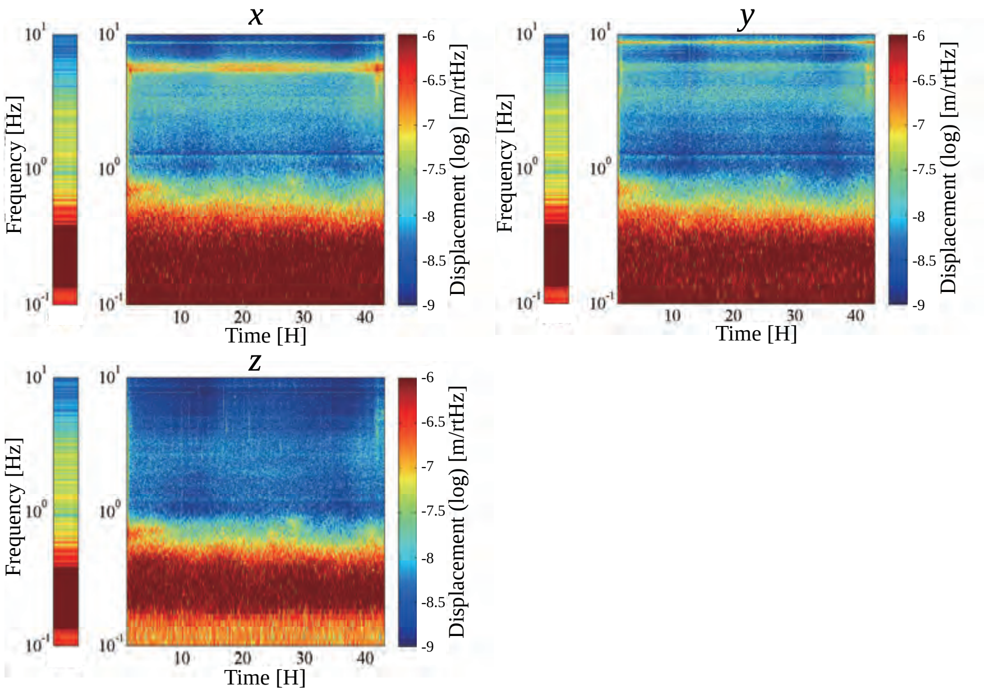

Figure 5.27: The spectrogram of the seismic displacement during the AVIT is on, which is plotted in the logarithm of 10. The top left, the top right, and the bottom left are the spectrogram of x, y, and z, respectively. The left color-bar on the left of the each spectrogram shows the seismic displacement with the AVIT off.

noise around 7 Hz is raised when the AVIT is on. It is because of the deterioration of the seismic noise at high frequencies. Since the phase margin around the peaks in 7 Hz and 9 Hz due to the resonance of the supporting table for the AVIT is not enough, the seismic noise gets worse around 7 Hz when the AVIT is controlled.

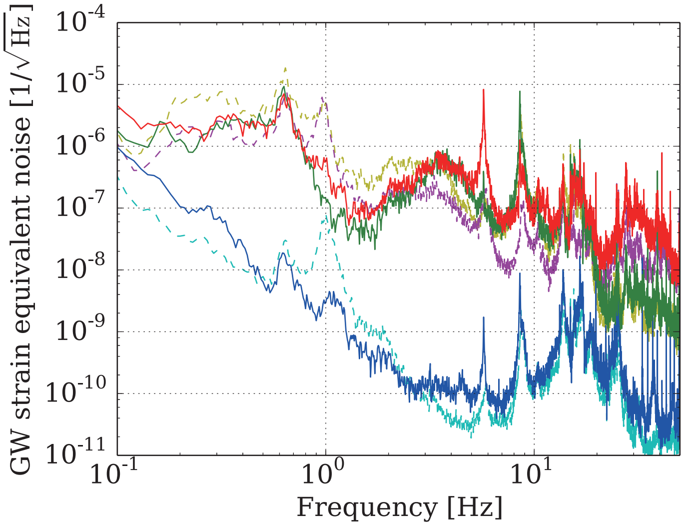

Figure 5.28: The sensitivity of signals with the AVIT on and off.The blue, green and red lines represent the sensitivity of s_1, s_2, and s_3 with AVIT on, respectively. The sky-blue, yellow, and pink dashed lines are the sensitivity of s_1, s_2, and s_3 with AVIT off.

Chapter 6

Observation and Analysis

Using the Phase-II TOBA we developed, the observational run had been performed as a part of the end-to-end test. As a demonstration, we have searched for compact binary coalescences around 1 to 10 Hz using matched filtering analysis. The target source is the intermediate mass black hole binaries with the mass of 200 $M_\odot$, which had never been searched for previously. In this chapter, we will explain about the source and how to analyze the data obtained from the Phase-II TOBA.

6.1 Intermediate-Mass Black Hole Binaries

The compact binary coalescences (CBCs) are the most promising source for the GW detectors. The frequencies of GWs emitted from the binary system depend on their mass. At lower frequencies where TOBA has good sensitivity, such as around 1 Hz, GWs from the intermediate-mass black holes (IMBHs), having masses of $10^2 M_\odot \lesssim m \lesssim 10^3 M_\odot$ are the main observation target.

Recently, hyper-luminous X-ray source 1, HLX-1, in the galaxy M82 was proven to be the IMBH from the observation with Chandra and Swift [44]. The IMBHs are considered to be mainly in globular clusters and formed by the core collapse of large star clusters [60]. These IMBHs formed in the cluster would fall into their host galaxy. When they interact with other IMBHs on the way to the center of their host galaxy, they would form a binary system, which emit energy in the form of the GW. Since they lose their energy because of the gravitational radiation, they would merge and form a single super-massive black hole at the center of the galaxy. This is one of the hypotheses of the formation of the super massive black holes.

Besides the observations with electro-magnetic waves, the GW detectors are expected to observe such IMBH coalescence directly and estimate how often the IMBHs merge and form a super massive black hole. The direct observation of IMBHs with GWs will reveal how the super massive black holes are evolving, and how the galaxies are evolved.

6.2 Matched Filtering

6.2.1 Waveform

As explained previously, GW signal $h(t)$ is usually smaller than detector noise $n(t)$. However, it is possible to detect $h(t)$ smaller than the noise floor of the detector if we know the form of the signal $h(t)$, by taking the correlation with the detector output $s(t) = h(t) + n(t)$ and the known signal $h(t)$.

CBCs are composed of three dynamical phases: inspiral, merger, and ringdown. In the inspiral phase, the chirp signal is obtained as described in Sec.2.2.1. The waveforms of the inspiral are described accurately by the post-Newtonian approximation to the Einstein equation [18]. The signal in the merger phase is modeled only with numerical simulations since there is a nonlinear effect [33]. The ringdown is the phase that the merged objects are resting. In our analysis, we searched for only the chirp signals. In the following, we will explain about the chirp waveform in details.

The GW signal as observed by the detector is written as

$$h(t) = F_+ h_+(t) + F_\times h_\times(t), \tag{6.1}$$

as explained in 3.19. Here, the pattern functions are assumed to be constant since the effect of the Earth spin is negligible for the GW signals with the frequencies of 1 - 10 Hz. The chirp waveform can be written as

$$\begin{aligned} h_+(t) &= -\frac{GM_\odot}{c^2 r}(1+\cos^2\iota)h_c(t), & (6.2)\\ h_\times(t) &= -\frac{2GM_\odot}{c^2 r}\cos\iota h_s(t), & (6.3) \end{aligned}$$

with

$$\begin{aligned} h_c(\tau) &= \frac{2}{c^2}\left(\frac{\mu}{M_\odot}\right)(\pi G M f(t))^{2/3}\cos\Phi(t), & (6.4)\\ h_s(\tau) &= \frac{2}{c^2}\left(\frac{\mu}{M_\odot}\right)(\pi G M f(t))^{2/3}\sin\Phi(t). & (6.5) \end{aligned}$$

Here, $G, M_\odot, c, r$ and ι are the gravitational constant, the solar mass, the speed of light, luminosity distance from the Earth to the source, and the inclination angle. μ is called the reduced mass of the binary defined as

$$\mu = \frac{m_1 m_2}{m_1 + m_2}, \tag{6.6}$$

where m_1 and m_2 are the mass of the binary objects. M is the total mass of the binary defined as $M = m_1 + m_2$. The GW frequency $f(t)$ is function of time since the period of the binary system varies. $f(t)$ and $\Phi(t)$ is calculated through the post-Newtonian formalism [18]. At leading order,

$$f(t) = \frac{c^3}{8\pi GM}\left(\frac{5GM}{c^3\eta(t_c - t)}\right)^{3/8}, \tag{6.7}$$

where η is the symmetric mass ratio $\eta = m_1 m_2/M^2$ and t_c is the coalescence time. The orbital phase $\Phi(t)$ is derived as

$$\Phi(t) = \int f(t)dt - \phi_0, \tag{6.8}$$

where ϕ_0 is an initial orbital phase.

As described later, the analysis is performed in the frequency domain. Using the stationary phase approximation, the chirp signals in the frequency domain is derived [58, 27] as

$$\tilde{h}_c(f) = \frac{2GM_\odot}{c^2 r}\left(\frac{5\mu}{96M_\odot}\right)^{1/2}\left(\frac{M}{\pi^2 M_\odot}\right)^{1/3} f^{-7/6}\left(\frac{G}{M_\odot}\right)^{-1/6} e^{i\Psi(f;M,\eta)}, \tag{6.9}$$

with

$$\begin{aligned}\Psi(f; M, \eta) = 2\pi f t_c - 2\phi_0 - \frac{\pi}{4} + \frac{3}{128\eta}\Bigg[&x^{-5} + \left(\frac{3715}{756} + \frac{55}{9}\eta\right)x^{-3} - 16\pi x^{-2} \\ &+ \left(\frac{15293365}{508032} + \frac{27145}{504}\eta + \frac{3085}{72}\eta^2\right)x^{-1}\Bigg],\end{aligned} \tag{6.10}$$

where $x = (\pi M f G/c^3)^{1/3}$. Since $h_s(t)$ and $h_c(t)$ are orthogonal to each other, $\tilde{h}_s(f)$ is obtained as

$$\tilde{h}_s(f) = i\tilde{h}_c(f). \tag{6.11}$$

These equations are used for the matched filtering explained in the next sub-section.

6.2.2 Matched Filtering Algorithm

In order to detect the small signal $\tilde{h}(f)$ in the detector output $\tilde{s}(f) = \tilde{h}(f) + \tilde{n}(f)$, where $\tilde{n}(f)$ is the detector noise, we take the correlation between $\tilde{h}(f)$ and $\tilde{s}(f)$ as the signal of the analysis:

$$z(t) = (s|h), \tag{6.12}$$

where $(a|b)$ is the inner product defined by

$$(a|b) = 4\mathrm{Re}\int \frac{\tilde{a}(f)^{*}\tilde{b}(f)}{S_n(f)} e^{2\pi i f t} df. \tag{6.13}$$

Here, the data are weighted by the noise power spectral density of the detector output $S_n(f)$. * denote a complex conjugate. Since h consists of two orthogonal signals $h_c(t)$ and $h_s(t)$, the signal z is computed by

$$z = \sqrt{(s|h_c)^2 + (s|h_s)^2}. \tag{6.14}$$

The variance of $(s|h)$ in the presence of a signal is

$$\begin{aligned}\sigma^2 &= \left\langle [(s|h) - (h|h)]^2 \right\rangle = \left\langle [(n|h)]^2 \right\rangle \\ &= (h|h).\end{aligned} \tag{6.15}$$

Therefore, the squared SNR ρ^2 is written as

$$\rho^2 = \frac{|z|^2}{\sigma^2}, \tag{6.16}$$

which is analytically maximized over the amplitude and the phase of the GW waveform. Note that ρ^2 has χ^2 distribution with 2 degrees of freedom when the detector noise is Gaussian.

6.3 Analysis Pipeline

The flowchart of the signal processing is shown in Fig.6.1. In our analysis, the most sensitive signal s_1 is mainly used for the analysis, though we have the other signals s_2 and s_3. s_2 and s_3 are used only for the coincidence check when s_1 has the significant signal. In other words, we perform the analysis using only s_1 and the other signals s_2 and s_3 are used only for the consistency check.

6.3.1 Segmentation and Calibration

At first, we divide the raw signal into the several segments with the length of T_{seg}. Each segment is analyzed independently after transformed into the frequency domain and calibrated according to the description in Sec.4.5.1. In the Fourier transformation, we use the Hanning window as a window function. Therefore, we take the

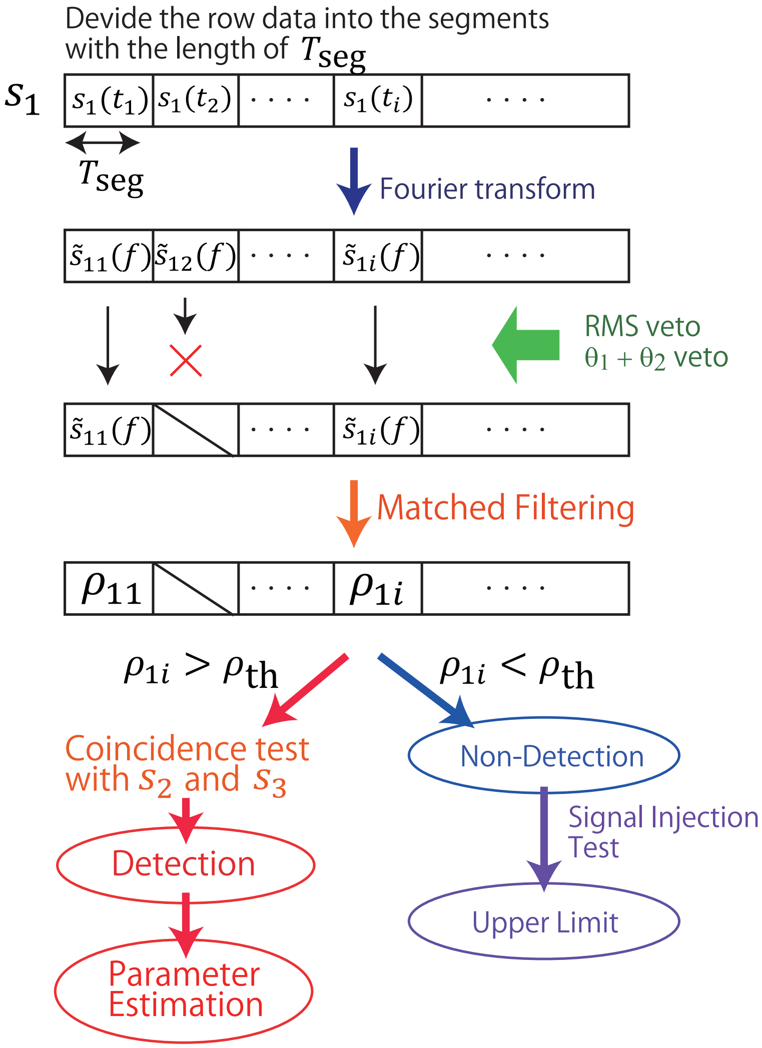

Figure 6.1: The flowchart of the signal processing.

overlap of 50 % between the two segments next to each other so that information is not lost because of the window function.

After the Fourier transformation is performed, the data are calibrated into the GW strain equivalent amplitude as described in Sec.4.5.1. Using calibrated data, the data selection is performed as a next step.

6.3.2 Data Selection

The noise level over the observation time is not stable. Sudden noise, such as spike-like noise is temporarily observed. Such noise will affect the analysis badly. Sometimes they are detected as signals in error, or make the upper limit worse.

Therefore, we select the data to be analyzed and condition the data quality. It is important not to remove the GW signals intentionally. In our analysis, we applied two vetoes in order to remove the noisy segment.

RMS Veto

When the noise level gets worse, the root mean square (RMS) gets larger. Therefore, we remove the segments where the RMS value is large. At first, the data is whitened as

$$\tilde{s}_{ij\mathrm{wt}} = \frac{\tilde{s}_{ij}(f)}{\overline{|\tilde{s}_i(f)|}}, \tag{6.17}$$

where i is the indexes of the output signals and j is the indexes of the segments. $|\tilde{}_i\bar{(f)}s|$ is the averaged spectrum over the whole segments. This procedure enables us to evaluate the level of the noise floor by reducing the effect at the peaks appear at the specific frequencies.

The RMS is calculated only the outside of the frequency range where the matched filtering is performed. It prevents GW signals from being removed intentionally. In our analysis, two frequency band is used to calculate the RMS. One is below 0 - 1 Hz, the other is 10 - 100 Hz. In other words,

$$X = \sqrt{\sum_{f=0}^{0.1} |s_{ij\mathrm{wt}}(f)|^2 + \frac{1}{90}\sum_{f=10}^{100} |s_{ij}(f)|}, \tag{6.18}$$

where the coefficient 90 is the normalizing factor, so that the weight of the RMS at two frequency band is equal.

$\theta_1 + \theta_2$ Veto

The data is also selected using the actual data which do not have sensitivity to GWs, i.e., $\theta_1 + \theta_2$. The signal $s_1 = \theta_1 - \theta_2$, which has the information about the noise and GWs, is used in order to derive the SNR ρ in the main analysis. Here, the SNR ρ_{veto} calculated by the matched filter analysis using the veto signal $s_{\mathrm{veto}} = \theta_1 - \theta_2$ is used for a veto indicator. The segments with large ρ_{veto} are removed by this veto procedure.

While the GW signals are rejected in s_{veto}, s_{veto} has the information about the noise level. Therefore, this is the effective veto system which exploits the information about the noise at the analyzed frequencies while the GW signals are not intentionally removed.

6.3.3 Matched Filtering and Signal Detection

The matched filtering analysis is performed using the survived data segments. The SNR is derived as described in Sec.6.2. The presence of the GW signal is determined according to the values of the square SNR ρ_{1j}^2.

According to the Neyman-Pearson criterion, the decision rule is given as

- if $\rho_{1j} \leq \rho_{\mathrm{th}}$, the signal is present in the j-th segment,
- if $\rho_{1j} < \rho_{\mathrm{th}}$, the signal is absent in the j-th segment.

ρ_{th} is called 'detection threshold,' which is determined from the probability distribution of ρ_{1j} and the false alarm rate. The false alarm rate is the probability that we decide the signal is present, though the signal is absent in reality. Defining the probability distribution of ρ_{1j} when the signal is absent as $p(\rho|0)$, the false alarm rate α is written as

$$\alpha = \int_{\rho_{\mathrm{th}}}^{+\infty} p(\rho|0) d\rho. \tag{6.19}$$

In the case of the matched filtering, $p(\rho|0)$ is χ^2 distribution with two degrees of freedom.

If the signal is detected, the consistency with s_2, s_3, or the environmental signal is checked in order to ascertain the detected signal is not noise but GWs. Here, the GW parameters such as their amplitude, i.e., the distance to the source, is estimated from the value of ρ. When the signal is undetected, the injection test is processed in order to set the upper limit.

6.3.4 Upper Limit

We performed the signal injection test in order to set an upper limit. This analysis derives the distance to the GW sources from which the GW signals are detectable with our detector. The procedure is as follows:

- Make the simulated signal in the frequency domain from the GWs source apart from the Earth by the distance r. The sky position of the source of the mock signal, polarization angle, and the inclination angle are randomly decided.
- Inject the signal into a randomly chosen segment and calculate the SNR of the injected segment.
- Repeat the first and the second procedure.
- Calculate a false dismissal rate (FDR), which is the probability that we miss the GW signals, from the obtained distribution of the SNR.
- Change the distance r and repeat the procedure above. Then the FDR function of r is derived.

The distance r where the FDR is β is the upper limit with the confidence level of β.

6.4 Observation

We performed the observation from 8:50 UTC, December 10, 2014 to 8:50 UTC, December 11, 2014. The control system stably continued for more than 24 hours. The latitude and the longitude of the cite are (35.42, 139.45). The two test mass bars lie almost north and south, and east and west. One is oblique in the northwest to the southeast direction by about 10 degrees from the north-south line, and the other.

The spectrogram of the signals during the observational run is shown in Fig.6.2. The control systems continued stably, and are disturbed mainly by the earthquakes.

6.5 Parameters

In our analysis, we searched for the GWs from the binary of equal-mass IMBHs with the mass of $200M_{\odot}$. Though the waveform template bank is necessary in order

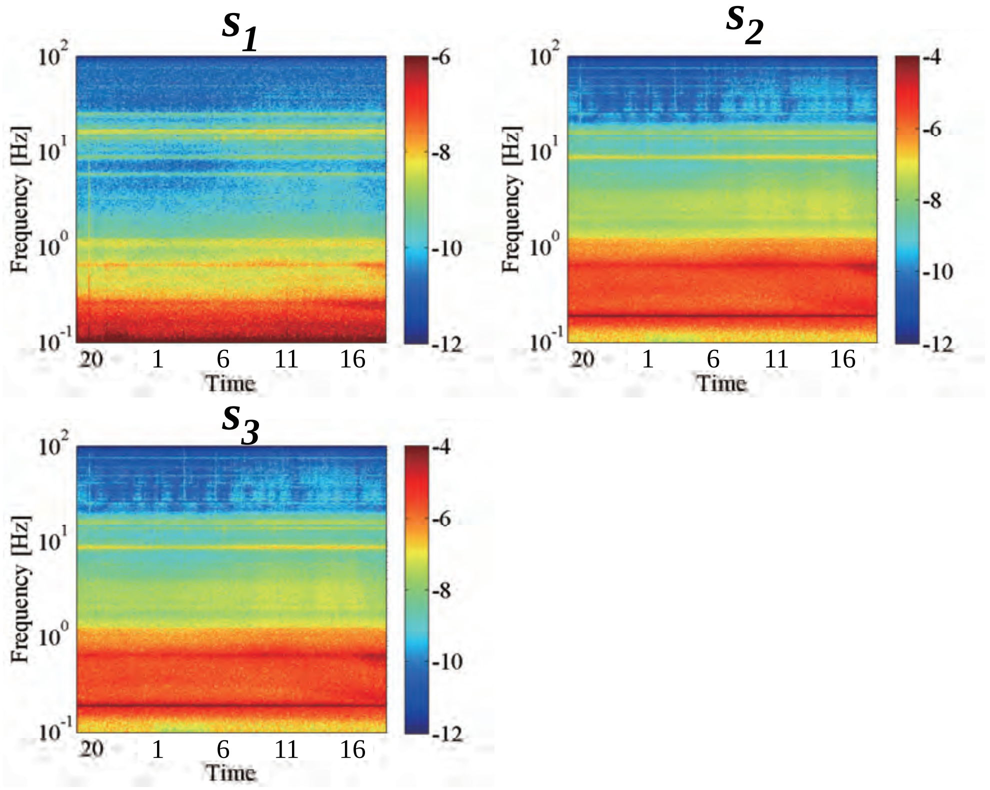

Figure 6.2: The spectrogram of the three signals during the observation.

to search for binaries with various parameters, we performed the matched filtering only with the fixed parameters for the simplification.

The obtained data were divided into the segments with the length of 200 seconds, and we take the overlap between the segments as 50 %. In the data selection pipeline, we removed the 10 % of the data in the RMS veto and the $\theta_1 + \theta_2$ veto respectively.

We have set the False Alarm Rate (FAR) as 10^{-5} events/year, which means $\alpha = 3.17 \times 10^{-11}$. Considering that the distribution of ρ^2 obeys χ^2 distribution, the detection threshold is determined as $\rho^2_{\mathrm{th}} = 48.3$.

6.6 Results

6.6.1 Data Selection

The values of RMS and ρ_{veto} is shown in Fig.6.3 and Fig.6.4. The lines are the values of the RMS and ρ_{veto}, and the circles represents the removed segments according to the each veto. The dots indicate the segments removed by the other veto. It shows the value of RMS increased as the observation continues, while ρ_{beto} is relatively stable over the observation.

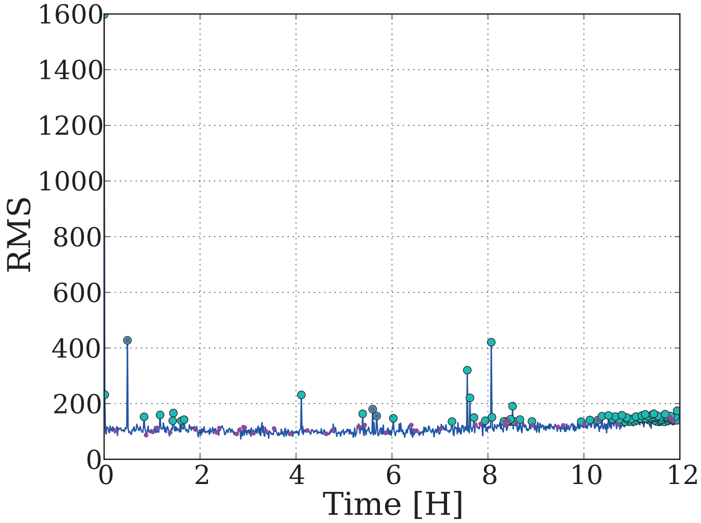

Figure 6.3: The value of RMS and the removed segments. The cyan circles are the removed segments by the RMS veto. The magenta dots are the segments removed by the $\theta_1 + \theta_2$ veto.

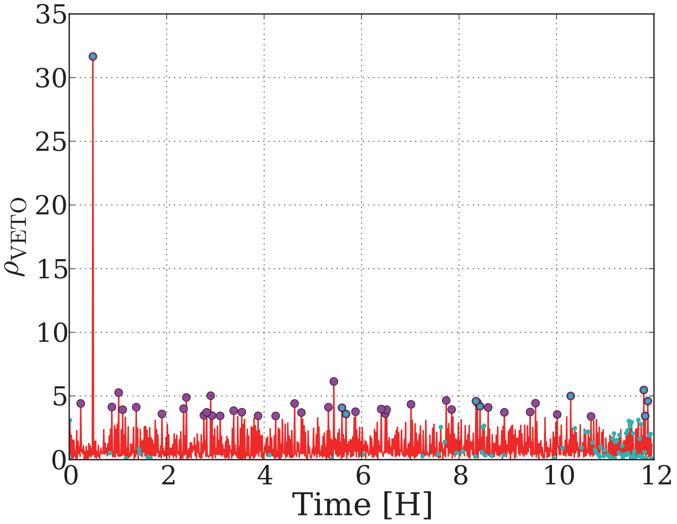

Figure 6.4: The value of ρ_{veto} and the removed segments. The magenta circles are the removed segments by the $\theta_1 + \theta_2$ veto. The cyan dots are the segments removed by the RMS veto.

6.6.2 Signal to Noise Ratio

The histogram of the ρ^2 obtained from the matched filter analysis is shown in Fig.6.5. The red line is the theoretical value of the χ^2 distribution. Though the values of SNR have tails, which exceed the χ^2 distribution, no signal which exceed ρ_{th} was found. Therefore, we concluded that no GW signal are detected.

6.7 Observational Boundary

Since we detected no GW signal, we have set an upper limit on the distance where IMBH does not exist. Figure 6.6 is the FDR derived from the signal injection. The distance where the FDR is 10 % is derived by collinear approximation using the data close to 10 %, which is independent from the assumption of the IMBH distribution. The fitted linear line is shown in the red line. Consequently, we have an 90 % confidence upper limit that no IMBH binaries exist where $r < (2.1 - 0.7) \times 10^{-4}$ pc from the fitted parameters with the fitting error.

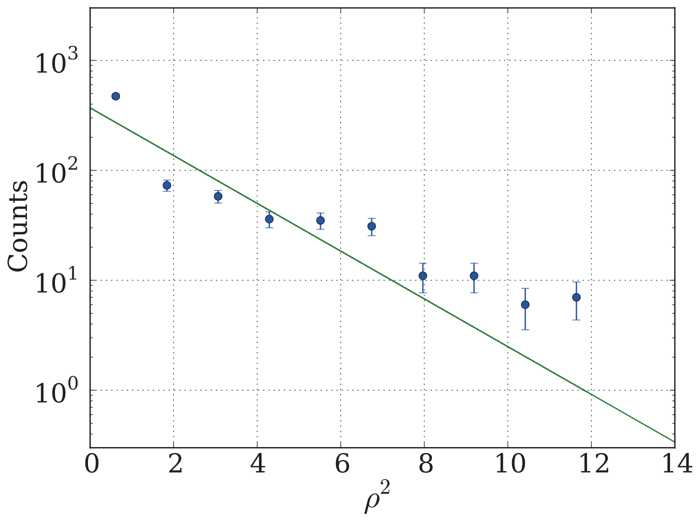

Figure 6.5: The blue dots are histogram of ρ. The green line is the theoretical line of χ^2 distribution.

The systematic error arises mainly from the uncertainty in calibration: the amplitude of the fringe of the interferometers, the beam spot position and fluctuation of the efficiency of coil-magnet actuators. We estimate these systematic error as 10 %. Therefore, our upper limit with 90 % confidence including the error is $r < (2.1 - 0.7 - 0.2) \times 10^{-4}$ pc.

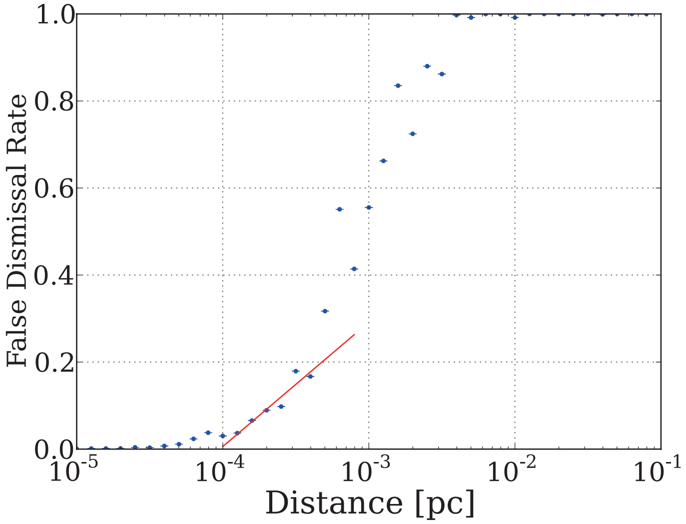

Figure 6.6: The false dismissal rate derived from the signal injection. The blue dots are derived FDR from the simulation. The red line is fitted linear line using 5 points around FDR = 10 %.

Chapter 7

Summary

7.1 Summary and Conclusion

We developed the detector called ‘Phase-II TOBA.’ The TOBA is GW detector which has two bar-shaped test masses. The two bars rotate due to the tidal force of GWs. Its main feature is that TOBA has a sensitivity at lower frequencies such as around 1 Hz even on the ground thanks to the low resonant frequencies of the rotational mode. Our scientific targets are GWs from IMBH binaries or a stochastic GW background. These observations will provide us the information about the Universe, which is not able to be obtained with the electro-magnetic waves. In order to detect GWs from mergers of IMBH binaries about 10 Gpc apart from the Earth, it is necessary to assemble many advanced technologies, such as high-Q suspension for 10-m scaled large test mass bars, cryogenic system, Fabry-Perot interferometric sensors on the torsion pendulum.

Previously, the first prototype TOBA had been developed. The principle test and the first GW observation around 0.2 Hz were performed as the first detector. In this thesis, we have developed the Phase-II TOBA, which is the new detector for the technical verification and the sensitivity improvement. We have focused on the vibration isolation technologies and the common mode noise reduction technologies, which are realized by a suspension system and an active vibration isolation table (AVIT). The Phase-II TOBA is an important step towards the detector with enough sensitivity for the GW astronomy.

Besides, we introduced the multi-output system in the Phase-II TOBA for the first time. The multi-output mode provides three independent signals from a single detector without the drastic change of the setup configuration. The only modules we add are the sensors for the vertical rotation monitoring. In our research, we pointed out that the test masses rotate in the vertical plane as well as the horizontal plane. Using the three signals, not only the event rate, but also the angular resolution would be improved since the three outputs have different response function to the GWs. Assuming the three signals have the same sensitivities, the event rate would be improved by about 1.7 times. Also, the sky positions of the GW sources could be determined with only a pair of detectors set apart, and also narrowed down to the 8 points even with a single detector, while three conventional detectors are necessary in order to determine the sky positions of the GW sources. It means that TOBA could evolve the GW astronomy with fewer detectors. The multi-output system enhances the value of TOBA as a simple and inexpensive ground-based detector for low-frequency GWs.

In our setup, the sensitivity in the horizontal rotation is achieved to be about $10^{-10}[1/\sqrt{\mathrm{Hz}}]$ in the GW strain at 7 Hz. The sensitivity was improved especially around 1 - 10 Hz by about 100 times than the previous detectors because of the passive vibration isolation using the suspension system and common mode noise rejection. As a result, the current sensitivity is limited by the residual seismic noise and sensor noise which is induced from fiber laser interferometers. Our result shows the efficiency of the vibration isolation system. The seismic noise has been reduced to be close to the sensor noise already. Especially, the AVIT is the powerful tool for the low-frequency vibration isolation system not only for TOBA but also other experiments which needs precise measurement.

Also, we successfully obtained the three signals at the same time and established the multi-output system. However, the sensitivity in the vertical rotation is worse by about 10^3 times than that in horizontal. The optical bench where the sensors and the actuators are set is also sensitive to GWs incoming from the horizontal direction. It reduces the sensitivity of the vertical monitor by about 10 times. The sensitivity is limited by the seismic noise over almost all the frequencies since the translational seismic displacement excites the rotational motion.

Using our setup, we have performed the observational run for 24 hours and searched for the chirp GW signal from mergers of IMBHs with the mass of $200M_{\odot}$. This is the first search for the IMBH black hole binaries with the mass larger than $100M_{\odot}$. Our system was stable enough to continue the observation for more than one day without losing its control. Using these data, the matched filtering analysis for the IMBH binary system with the mass of $200M_{\odot}$. As a result, no GW signals are detected and we exclude the presence of IMBH merger at $r < (2.1-0.7-0.2)\times 10^{-4}$ pc with 90 % confidence. Here the analysis pipeline for the IMBH search was successfully established in our detector.

7.2 Discussion and Future Perspective

7.2.1 Sensitivity

In order to improve the sensitivity more, the noise to get rid of at first is the seismic noise and laser sensor noise. As for the sensor noise, it is necessary to reveal the mechanism from which the sensor noise come. Though it is relatively easy to assemble many monitors with the fiber optics, more study is required in order to reduce the phase noise in the fiber optics enough. For the next upgrade, the sensors are necessary to be upgraded to the Fabry-Perot interferometers in terms of the advanced technology. Fabry-Perot interferometric sensors are expected to improve the sensitivity due to an optical spring effect [56]

In order to reduce the seismic coupling noise further, the much larger suspension system is required. However, since the resonant frequency of the pendulum mode is around 1 Hz, the peaks of the pendulum resonance would decrease the sensitivity. Still, it is fundamentally possible to reduce the seismic noise more by adjusting the position of the center of the mass of the optical bench and so on.

The vibration isolation rate of the AVIT could also be improved by replacing the piezoelectric elements to those with a larger dynamic range. In order to improve the performance at higher frequencies, the support table for the AVIT should be buttressed since the resonance of the supporting table limit the open loop transfer function of the control system.

In order to improve the sensitivity in lower frequencies, it is necessary to decrease the resonant frequency of the rotational mode. Since the resonant frequencies in our setup are relatively high, such as 0.1 Hz, due to the two suspension wires per one test mass, the test masses do not have a good response around 0.1 - 1 Hz. In order to reduce the resonant frequency, it is necessary to suspend the test masses with a single wire even though it is difficult to set the two centers of the mass at the same point.

Although the thermal noise is not observed in our experiment, research on the low-loss suspension system and on the cryogenic system are required at a following step. As for the cryogenic system, we already have the pulse-tube cooler. The cooling test and vibration reduction test of the heat anchor is the possible test for the next plan.

Also, the gravity gradient noise, called Newtonian noise [46], would limit the sensitivity in the future. It is caused by the gravity gradient caused by the seismic displacement of the ground, or the motion of the objects around the detectors. It is one of the fundamental noise for the TOBA since it affects the detectors largely at low frequencies. Since the Newtonian noise effects on the test masses through gravity, it cannot be shielded out. Therefore, the Newtonian noise has to be canceled out by the data processing using environmental sensors or multiple detectors [28, 17].

7.2.2 Multi-Output System

In our setup, we succeeded in controlling the test mass in 4 degrees of freedom at the same time and derive the 3 independent signals. However, it is revealed that the new signals largely couples to the translational seismic motion. Since the transfer function from the translational seismic displacement to the angular fluctuation is relative to f^{-2} above the resonant frequency of the rotational motion, the seismic coupling noise could be reduced when the resonant frequency of the optical bench is reduced to the same order of that of the test masses, as an analogy of the seismic noise in the horizontal rotation.

Also, it is necessary to re-design the shape of the optical bench so that the optical bench do not rotate according to the GWs, i.e., the quadrupole moment of the optical bench should be negligible.

7.2.3 Applications

Other than the gravitational astronomy, torsion pendulum has many applications to explore physics. One is the precise force measurement since a torsion pendulum behave as a free-falling mass at low frequencies even on the ground. Many precise measurement experiments have been performed with torsion pendulums, such as the test of inverse square low of the gravity, measurement of gravity constant, measurement of the Casimir force, test of the equivalent principle and so on. Our setup could be also applied to such measurement with the optimization of the parameters of the pendulum.

Other than that, the TOBA is expected to be applied to the prompt earthquake detection [65]. As mentioned in the last of Sec.7.2.1, the test mass of the TOBA is sensitive to the gravity gradient. When the large earthquake occurs, the gravitational potential changes [30]. The change of the gravity potential propagates with the speed of light, faster than the seismic waves: p-waves and s-waves. Therefore, if the change in the gravitational potential is detected with the TOBA, the earthquake is expected to be alerted earlier by about 5 seconds. In order to detect the gravitational potential fluctuation due to the large earthquake, the sensitivity of the order of $10^{-15}[1/\sqrt{\mathrm{Hz}}]$ is required, which is less sensitive than the 10-m scaled TOBA as shown in Sec.3.3. Since the TOBA is relatively low-cost compared to other GW detectors, it is feasible to set several TOBAs at various points. Then the center of the earthquake can be also detectable.

Chapter A

Decoupling matrices for Active Vibration Isolation System

The default matrices which converts signals to and from the each degrees of freedom, M_{in} and M_{out} are written as.

$$M_{\mathrm{in}} = \begin{pmatrix} 0 & -1/4 & 1/2 & 0 & 0 & 1/3 \\ 1/3 & 0 & 0 & 1/2 & 0 & \\ 0 & 1/2 & 0 & 0 & 0 & 1/3 \\ 1/3 & 0 & 0 & -1/4 & 1/2 & 0 \\ 0 & -1/4 & -1/2 & 0 & 0 & 1/3 \\ 1/3 & 0 & 0 & -1/4 & -1/2 & 0 \end{pmatrix} \tag{A.1}$$

$$M_{\mathrm{out}} = \begin{pmatrix} 1 & 0 & 1 & 0 & 1 & 1 \\ -1 & 0 & 1 & 0 & 1 & -1 \\ -0.5 & 1 & 1 & 1 & -0.5 & 1 \\ 0.5 & -1 & 1 & 1 & -0.5 & -1 \\ -0.5 & -1 & 1 & -1 & -0.5 & 1 \\ 0.5 & 1 & 1 & -1 & -0.5 & -1 \end{pmatrix} \tag{A.2}$$

where the matrices are defined as

$$\begin{pmatrix} S_{\mathrm{H}_1} \\ S_{\mathrm{V}_1} \\ S_{\mathrm{H}_2} \\ S_{\mathrm{V}_2} \\ S_{\mathrm{H}_3} \\ S_{\mathrm{V}_3} \end{pmatrix} M_{\mathrm{in}} = \begin{pmatrix} S_x \\ S_y \\ S_z \\ S_{\mathrm{pitch}} \\ S_{\mathrm{roll}} \\ S_{\mathrm{yaw}} \end{pmatrix} \tag{A.3}$$

$$\begin{pmatrix} S_x & S_y & S_z & S_{\mathrm{pitch}} & S_{\mathrm{roll}} & S_{\mathrm{yaw}} \end{pmatrix} M_{\mathrm{out}} = \begin{pmatrix} S_{\mathrm{P1}} & S_{\mathrm{P2}} & S_{\mathrm{P3}} & S_{\mathrm{P4}} & S_{\mathrm{P5}} & S_{\mathrm{P6}} \end{pmatrix} \tag{A.4}$$

See Fig.C.4 for the definition of the label of sensors and actuators, and directions. Those matrices are adjusted so that the signals in the other degrees of freedom do not couple to the main signal. Especially, the tilt movement largely couples to the horizontal seismometers' signals at low frequencies. Therefore, M_{out} should be carefully adjusted so that the transfer functions from the actuator input to the horizontal seismometers outputs fit well to the theory even at low frequencies around 0.1 Hz.

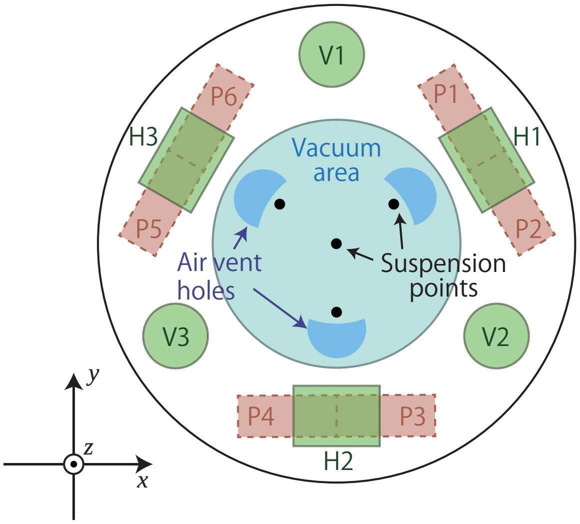

Figure A.1: The setup of the AVIT. P1, P2, . . . , and P6 are the piezoelectric elements below the table. V1, V2, and V3 are the seismometers which sens the vertical seismic motion, and H1, H2, and H3 are the ones which sens the horizontal seismic motion. Photo Sensors are set below the seismometers so that each of them measures the DC position of the table in the same direction as the seismometer above it. In the Vacuum area, the table has air vent holes in order to protect the piezoelectric elements from the pressure of the air.

Chapter B

Q measurement

Q values of the test mass pendulum is measured from the damped oscillation. Figure B.1 are the graph of the damped oscillation of longitudinal mode measured by the PSs. Note that the data was filtered by the resonant filter in order to get rid of the effect of the other noise. They are measured without the control system. The obtained Q values of the LONG, ROLL, and YAW modes are in Table B.1. The errors on the Q values are the fitting errors.

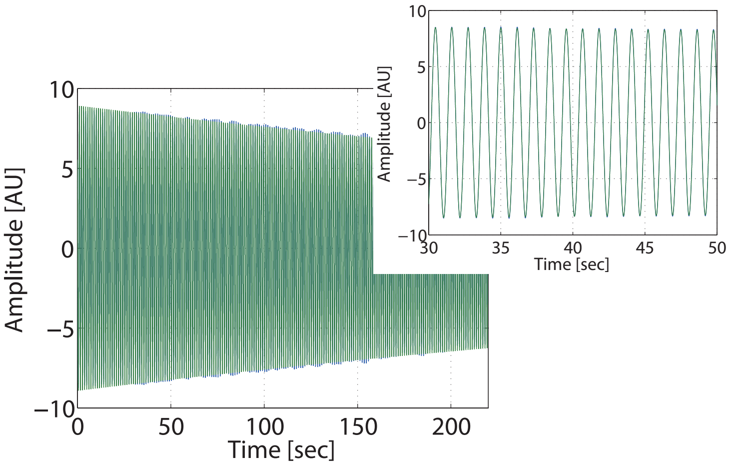

Figure B.1: The dumped oscillation of the longitudinal mode of the test mass. The blue line is the measured line, and the green line is the fitted line.

Pendulum mode	Resonant frequency [Hz]	Q value
LONG	0.88	1709 ± 3
YAW	0.10	4800 ± 10
ROLL (s_2)	0.19	311.1 ± 0.4
ROLL (s_3)	0.14	376.1 ± 4.6

Table B.1: The resonant frequencies and Q values of the test mass 1, which is along north-south direction.

Chapter C

Circuits

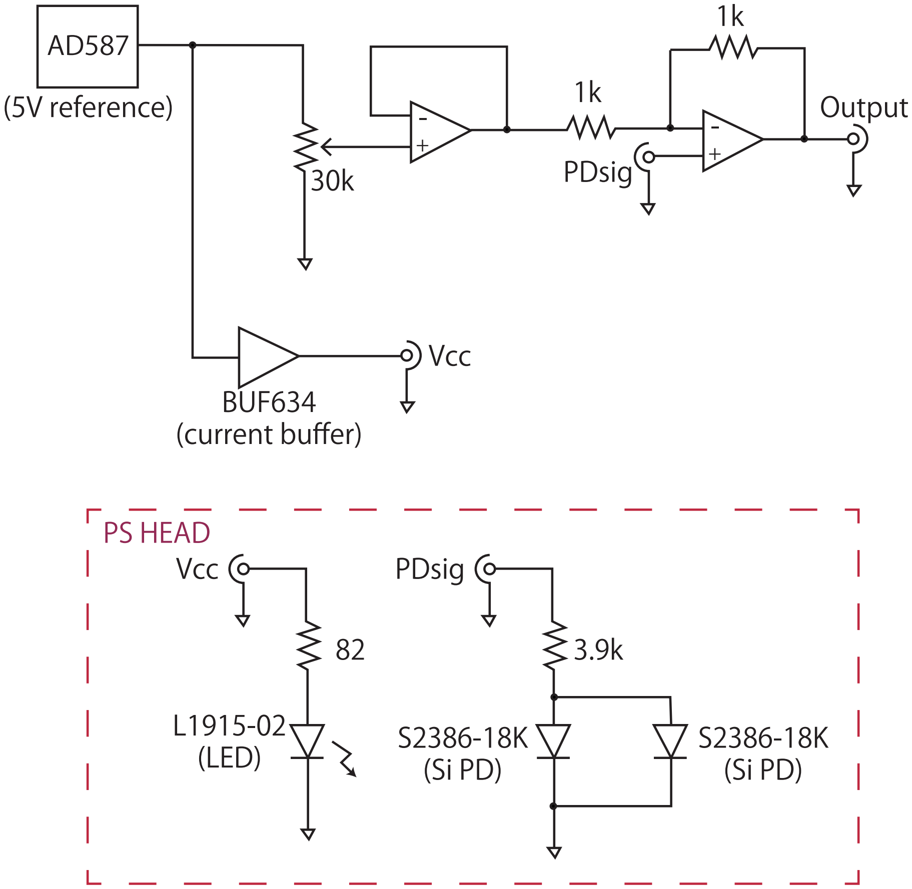

Figure C.1: A circuit for the photo sensor. It drives the LED and convert the photo detector current to the voltage.

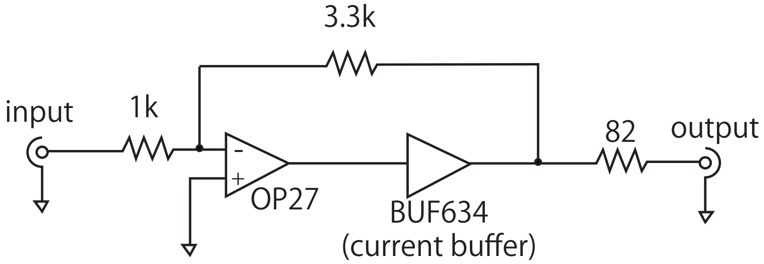

Figure C.2: A circuit for coil-drivers. It emit current enough for the coil-magnet actuators. BUF634 emit 200 mA at maximum.

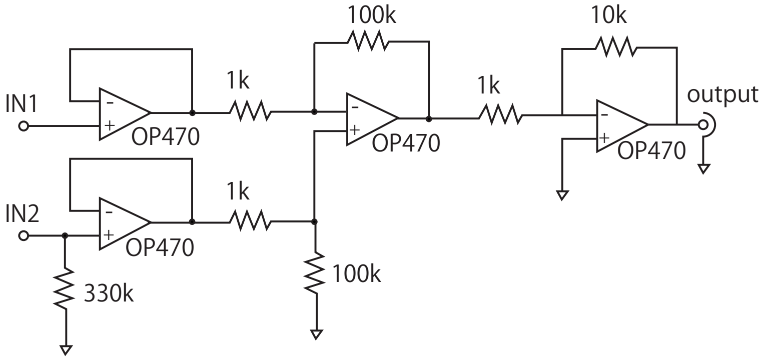

Figure C.3: A circuit for the seismometer amplifier. It has differential input ports and the amplifier gain of 1000.

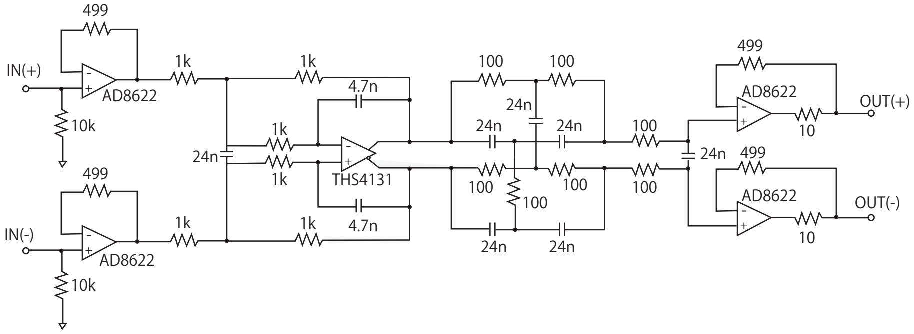

Figure C.4: A circuit for the anti-aliasing and anti-imaging filter. It is third order 10 kHz cut-off low-pass filters with notch at 65536 Hz, which is the frequency of the timing signal. They are placed before the ADC input and after the DAC output.

Acknowledgement

This work could not be accomplished without lots of supports and advices from many people.

I am deeply grateful to Prof. Masaki Ando for the constant support. When we were designing our detector, he patiently advised me in spite of my poor understandings. He has also watched over and supported me in the construction phase. Also, advices from Prof. Kimio Tsubono is indispensable for my thesis. I have a great honor to have him as my former supervisor. It was a great time to talk with him about the physic and the future plans. The former assistant professor in our lab, Prof. Yoichi Aso, also give me a lot of advice especially about the development of the AVIT. The AVIT developed in this thesis is originally the active vibration isolation system for a cryogenic optical cavity for the frequency-stabilized laser source which Prof. Aso proposed.

I was greatly helped by co-researchers. I am obliged to Mr. Kazunari Eda and Prof. Yosuke Ito for their calculation of the multi-output system. Their work reveal the significance of my proposal. Mr. Yuya Kuwahara have been working on the experiment with me and complemented our thesis. He can point out the essential issues and made enormous contribution. I would also like to express my gratitude to Mr. Kodai Tejima for designing the pendulum with us.

Also, our experiments are not accomplished without Mr. Shigemi Otsuka, Mr. Yoshikatsu Nanjo, and Mr. Takeshi Abe, the engineers in the Science Faculty. They finely manufactured the parts of our setup in spite of our immature blueprints. Also their warm encouragement cheers me up when I was tired during the experiment.

I also appreciate Prof. Osamu Miyakawa. He told me everything about the digital systems. Whenever we had troubles, he kindly tell me what to do. Our work was not accomplished without Osamu.

Additionally, several companies have been involved in this work. I appreciate Mr. Yoshitaka Takahashi (Cosmotec Corporation) for the construction of the vacuum system. Mr. Yasuhiro Higuchi, Mr. Tsutomu Nakanishi, and Mr. Shuichi Goto (Jecc Torisha Co., Ltd.) also helped us for the cryogenic system.

I would like to express my gratitude to our group members. It was really lucky to me that I started my research career at the same time with Mr. Yuta Michimura who is a current assistant professor in our lab. He is one of the most dependable researcher who can take care of the lab members. I am greatly honor to have him

as a comrade from now on. Dr. Nobuyuki Matsumoto often tells me interesting researches on the optical mechanics. Though I do not know about the opt-mechanics well, I admire his deep understandings and insights into the optical physics. Mr. Takafumi Ushiba is a researcher who can work steadily with objective view. When I worked with him on the experiment for the frequency-stabilized laser source, he helped me a lot of work without getting down even though the process was troublesome. Mr. Kentaro Komori is also a promising student in our group. I am really looking forward to hearing that his enthusiastic work has been accomplished. I also would like to thank my former group mate, Prof. Koji Ishidoshiro, Mr. Kakeru Takahashi, Mr. Kenshi Okada, and Mr. Kazunori Shibata. Especially, Prof. Koji Ishidoshiro and Mr. Kenshi Okada supported me with the inspect of the previous TOBA experiments. Other than the Ando's group member, I would like to express the deepest appreciation to Dr. Noriaki Ohmae, who is a co-researcher of the frequency-stabilized laser source experiment. He always gives me fruitful advices especially on the development of the AVIT. Ms. Miki Ueda, Ms. Michiko Kondo, and Ms. Ami Ito has helped me with the official work.

In addition, I am grateful to Prof. Makoto Sasaki, Prof. Kazuo Makishima, Prof. Hiroshi Fukuyama, Prof. Naoki Yoshida, and Prof. Takeo Moroi, members of a thesis committee. They gave me a lot of useful advices during the defense of my thesis.

Finally, I would like to offer my special thanks to my parents, and my husband. They, especially my husband, never blamed on me even though I neglect the houseworks. He always warmly encouraged and watched over me when I was depressed. I believe that I could overcome anything only if I am with him.

Bibliography

[1] Aasi, J. et al., "Einstein@Home all-sky search for periodic gravitational waves in LIGO S5 data," Phys. Rev. D 87, 042001 (2013).

[2] Aasi, J. et al., "Search for gravitational waves from binary black hole inspiral, merger, and ringdown in LIGO-Virgo data from 20092010," Phys. Rev. D 87, 022002 (2013).

[3] Aasi, J. et al., "Implementation of an F-statistic all-sky search for continuous gravitational waves in Virgo VSR1 data," ArXiv preprint arXiv:1402.4974 (2014).

[4] Aasi, J. et al., "Searches for continuous gravitational waves from nine young supernova remnants," ArXiv preprint arXiv:1412.5942 (2014).

[5] Aasi, J. et al., "Search for Gravitational Waves Associated with gamma-ray Bursts Detected by the Interplanetary Network," Phys. Rev. Lett. 113, 011102 (2014).

[6] Abadie, J. et al., "All-sky search for gravitational-wave bursts in the second joint LIGO-Virgo run," Phys. Rev. D 85, 122007 (2012).

[7] Abadie, J. et al., "Search for gravitational waves from binary black hole inspiral, merger, and ringdown," Phys. Rev. D 83, 122005 (2011).

[8] Abadie, J. et al., "Predictions for the rates of compact binary coalescences observable by ground-based gravitational-wave detectors," Class. Quantum Gravity 27, 173001 (2010).

[9] Abbott, B. P. et al., "An upper limit on the stochastic gravitational-wave background of cosmological origin," Nature 460, 9904 (2009).

[10] Accadia, T. et al., "Status of the Virgo project," Class. Quantum Gravity 28, 114002 (2011).

[11] Akutsu, T. et al., "Search for a Stochastic Background of 100-MHz Gravitational Waves with Laser Interferometers," Phys. Rev. Lett. 101, 101101 (2008).

[12] Ando, M., Ishidoshiro, K., Yamamoto, K., Yagi, K., and Kokuyama, W., “Torsion-Bar Antenna for Low-Frequency Gravitational-Wave Observations,” 161101, 14 (2010).

[13] Aoyama, S., Tazai, R. , and Ichiki, K., “Upper limit on the amplitude of gravitational waves around 0.1 Hz from the Global Positioning System,” Phys. Rev. D 89, 067101 (2014).

[14] Armstrong, J. W., Iess, L., Tortora, P. , and Bertotti, B., “Stochastic Gravitational Wave Background: Upper Limits in the $10-6$ to $10-3$ Hz Band,” Astrophys. J. 599, 806813 (2003).

[15] Astone, P. et al., “Crosscorrelation measurement of stochastic gravitational waves with two resonant gravitational wave detectors,” Astron. Astrophys. (1999).

[16] Babak, S. et al., “Searching for gravitational waves from binary coalescence,” Phys. Rev. D 87, 024033 (2013).

[17] Beker, M. G. et al., “Improving the sensitivity of future GW observatories in the 110 Hz band: Newtonian and seismic noise,” Gen. Relativ. Gravit. 43, 623656 (2010).

[18] Blanchet, L., Iyer, B., and Joguet, B., “Gravitational waves from inspiraling compact binaries: Energy flux to third post-Newtonian order,” Phys. Rev. D 65, 064005 (2002).

[19] Cella, G., Sannibale, V., DeSalvo, R., Mrka, S. , and Takamori, A., “Monolithic geometric anti-spring blades,” Nucl. Instruments Methods Phys. Res. Sect. A Accel. Spectrometers, Detect. Assoc. Equip. 540, 502519 (2005).

[20] Chen, D. et al., “Vibration measurement in the KAGRA cryostat,” Class. Quantum Gravity 31, 224001 (2014).

[21] Coccia, E., Dubath, F. , and Maggiore, M., “Possible sources of gravitational wave bursts detectable today,” Phys. Rev. D 70, 084010 (2004).

[22] Cokelaer, T., “Gravitational waves from inspiralling compact binaries: Hexagonal template placement and its efficiency in detecting physical signals,” Phys. Rev. D 76, 102004 (2007).

[23] LSC Collaboration et al., “Search for Gravitational Waves from Binary Black Hole Inspiral, Merger and Ringdown in LIGO-Virgo Data from 2009-2010,” ArXiv preprint arXiv:1209.6533 (2012).

[24] Coughlin, M., and Harms, J. Constraining, “The gravitational-wave energy density of the Universe in the range 0.1 Hz to 1 Hz using the Apollo Seismic Array,” Phys. Rev. D 90, 102001 (2014).

[25] Coughlin, M., and Harms, J., “Upper Limit on a Stochastic Background of Gravitational Waves from Seismic Measurements in the Range 0.051 Hz,” Phys. Rev. Lett. 112, 101102 (2014).

[26] Coughlin, M., and Harms, J. Constraining, “The gravitational wave energy density of the Universe using Earth ’ s ring,” Phys. Rev. D 90, 042005 (2014).

[27] Cutler, C., and Flanagan, ., “Gravitational waves from merging compact binaries: How accurately can one extract the binary ’ s parameters from the inspiral waveform?,” Phys. Rev. D 49, 26582697 (1994).

[28] Driggers, J. C., Harms, J., and Adhikari, R. X., “Subtraction of Newtonian Noise Using Optimized Sensor Arrays,” Phys. Rev. D 86, 102001, (2012).

[29] Eda, K., Shoda, A., Itoh, Y., and Ando, M., “Improving parameter estimation accuracy with torsion-bar antennas,” Phys. Rev. D 90, 064039 (2014).

[30] Einarsson, I., Hoechner, A., Wang, R., and Kusche, J. Gravity, “Changes due to the Sumatra-Andaman and Nias earthquakes as detected by the GRACE satellites: a reexamination,” Geophys. J. Int. 183, 733747 (2010).

[31] Finn, L., “Detection, measurement, and gravitational radiation,” Phys. Rev. D 46, 52365249 (1992).

[32] Frajuca, C. et al., “Searching for monochromatic signals in the ALLEGRO gravitational wave detector data,” J. Phys. Conf. Ser. 228, 012007 (2010).

[33] Hannam, M., “Status of black-hole-binary simulations for gravitational-wave detection,” Class. Quantum Gravity 26, 114001 (2009).

[34] Harms, J. et al., “Low-frequency terrestrial gravitational-wave detectors,” Phys. Rev. D 88, 122003 (2013).

[35] Hulse, R. A., and Taylor, J. H., "Discovery of a pulsar in a binary system," Astrophys. J. 195, L51 (1975).

[36] Ishidoshiro, K., Ando, M., Takamori, A., Okada, K., and Tsubono, K., "Gravitational-wave detector realized by a superconductor," Phys. C Supercond. its Appl. 470, 18411844 (2010).

[37] Ishidoshiro, K., Ph.D. thesis, "Search for low-frequency gravitational waves using a superconducting magnetically-levitated torsion antenna," University of Tokyo (2010).

[38] Ishidoshiro, K. et al., "Upper Limit on Gravitational Wave Backgrounds at 0.2 Hz with Torsion-bar Antenna," 12, 25 (2011).

[39] Kawamura, S. et al., "The Japanese space gravitational wave antenna: DECIGO," Class. Quantum Gravity 28, 094011 (2011).

[40] Maggiore, M., "Gravitational wave experiments and early universe cosmology," Phys. Rep. 331, 283367 (2000).

[41] Maggiore, M., Gravitational Waves: Volume 1: Theory and Experiments. (Oxford University Press, 2007).

[42] Maggiore, M., "GRAVITATIONAL WAVE EXPERIMENTS AND EARLY UNIVERSE COSMOLOGY Gravitational wave experiments and early universe cosmology," Physics Reports 331, 283 (2000).

[43] Ott, C. D., "The gravitational-wave signature of core-collapse supernovae," Class. Quantum Gravity 26, 063001 (2009).

[44] Pasham, D. R., Strohmayer, T. E., and Mushotzky, R. F., "A 400-solar-mass black hole in the galaxy M82," Nature 513, 746 (2014).

[45] Rosa, R. De, Garufi, F., Milano, L., Mosca, S., and Persichetti, G., "Characterization of electrostatic actuators for suspended mirror control with modulated bias," J. Phys. Conf. Ser. 228, 012018 (2010).

[46] Saulson, P., "Terrestrial gravitational noise on a gravitational wave antenna," Phys. Rev. D 30, 732736 (1984).

[47] Schutz, B. F., "Networks of gravitational wave detectors and three figures of merit," Class. Quantum Grav. 28 125023 (2011).

[48] Shoda, A. et al., “Search for a stochastic gravitational-wave background using a pair of torsion-bar antennas,” Phys. Rev. D 89, 027101 (2014).

[49] Somiya, K., “Detector configuration of KAGRAthe Japanese cryogenic gravitational-wave detector,” Class. Quantum Gravity 29, 124007 (2012).

[50] Takamori, A., Ph.D. thesis, “Low Frequency Seismic Isolation for Gravitational Wave Detectors,” University of Tokyo (2002)

[51] Taylor, J. H., and Weisberg, J. M., “A new test of general relativity - Gravitational radiation and the binary pulsar PSR 1913+16,” Astrophys. J. 253, 908 (1982).

[52] Taylor, S. R., and Gair, J. R., “Cosmology with the lights off: Standard sirens in the Einstein Telescope era,” Phys. Rev. D 86, 023502 (2012).

[53] The LIGO Scientific Collaboration, “Advanced LIGO,” ArXiv preprint arXiv:1411.4547 (2014).

[54] The LIGO Scientific Collaboration et al. “Narrow-band search of continuous gravitational-wave signals from Crab and Vela pulsars in Virgo VSR4 data,” ArXiv preprint arXiv:1410.8310 (2014).

[55] Vitale, S., “Space-borne gravitational wave observatories,” Gen. Relativ. Gravit. 46, 1730 (2014).

[56] Wang, Q.-L., Yeh, H.-C., Zhou, Z.-B., and Luo, J., “Improving the sensitivity of a torsion pendulum by using an optical spring method,” Phys. Rev. A 80, 043811 (2009).

[57] Weber, J., “Anisotropy and Polarization in the Gravitational-Radiation Experiments,” Phys. Rev. Lett. 25, 180184 (1970).

[58] Will, C., and Wiseman, A., “Gravitational radiation from compact binary systems: Gravitational waveforms and energy loss to second post-Newtonian order,” Phys. Rev. D 54, 48134848 (1996).

[59] Yakunin, K. N. et al., “Gravitational waves from core collapse supernovae,” Class. Quantum Gravity 27, 194005 (2010).

[60] Zwart, S. F. P., Baumgardt, H., Hut, P., Makino, J., and McMillan, S. L. W., “Formation of massive black holes through runaway collisions in dense young star clusters,” Nature 428, 7246 (2004).

[61] Bendat, J. S., and Piersol, A. G., Random Data: Analysis and Measurement Procedures, (Wiley, 2010)

[62] Faulkner, Eric A., Introduction to the Theory of Linear Systems., (Chapman and Hall, 1969).

[63] Komori, K., Graduation thesis, University of Tokyo (2013)

[64] Kuwahara, Y., Graduation thesis, University of Tokyo (2013)

[65] Matteo, B., presentation at GWADW conference (2014)

[66] Hirakawa, H., Narihara, K., and Fujimoto, M., “Theory of Antennas for Gravitational Radiation,” J. Phys. Soc. Japan 41, 1093-1101 (1976).

[67] Bork, R., and Heefner, J., “Digital LOS and SOS Control Systems For LIGO,” LIGO document, LIGO-T000073-x0 (2000).